UNIVERSITÄT BREMEN

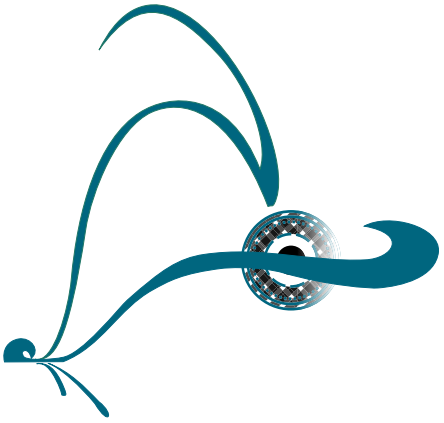

The Role of Electric Charge in Relativistic Accretion onto Compact Objects - An Analytical Approach

von

Kris Inken SCHROVEN

Eingereicht im Fachbereich Physik und Elektrotechnik zur
Erlangung des akademischen Grades eines
Doktor der Naturwissenschaften (Dr. rer. nat.)

Erstgutachter:	Prof. Dr. Claus Lämmerzahl
Zweitgutachterin:	Prof. Dr. Jutta Kunz

Acknowledgement

First of all I would like to thank my supervisor Claus Lämmerzahl for his support and openness towards various propositions.

I am especially grateful to Eva Höne for our insightful discussions and the support, she provided during these recent years.

Working together with Audrey Trova has been very enjoyable, so I need to take this chance and express my gratitude for this nice collaboration.

Needless to say, I am very grateful towards my fellow PhD students Paul Jefremov, Vojtěch Witzany and Efthimia Deligianni. I will remember the nice time we spent together on conferences or in Bremen and our many great discussions, whether they were on our research topics or something else entirely.

My sincere thank you goes to all my colleagues at ZARM, the "Gravi" group, my fellow PhD students from "Models of Gravity" and of course my friends for making the recent years during my PhD so enjoyable.

Last but not least, a big thank you goes to Svea Schroven, for being a great sister and what comes along with it. I would also like to thank my parents Hiltrud Floren and Ludwig Schroven for their support.

This work would not have been possible without financial support from the German Research Foundation within the Research Training Group "Models of Gravity" and within the Collaborative Research Centre "geo-Q".

Abstract

This thesis is dedicated to the discussion of the role of electric charge in relativistic accretion onto compact objects. Many high-luminosity phenomena in the observed universe can be traced back to accretion processes, in which electromagnetic fields play an important role. These fields are either produced within the accreted matter or they enter the stage as external fields like interstellar magnetic fields or fields, produced by the accreting object.

The first part of the thesis examines the accretion process of hydrogen plasma onto a weakly charged black hole. An analytical model describes a stationary accretion process of dilute collisionless plasma from a rotating spherical shell onto a rotating and charged black hole. Within the model the test-particle approach is used in order to describe the plasma particle motion. The model is applied to analyze the influence of a realistic black hole net charge on plasma accretion. It is shown, that even very small black hole charges may have a non-negligible effect on the accretion process, as long as the electromagnetic field, created by the plasma, is still negligible. The inner and outer edge of the forming accretion disc strongly depend on the particle charge in the plasma. Four possible accretion disc configurations are analyzed in detail.

The second part of the thesis concerns charged thick accretion discs around spinning compact objects, which are affected by an external magnetic dipole field. The situation is described in an idealized way by the Kerr metric and a magnetic dipole "test-field" in Kerr spacetime. Pressure equations describe the charged fluid structures. The self-consistency of the model and integrability conditions of the pressure equations lead to restrictions on the fluid conductivity and the charge distribution in the structures. Previous publications discussed the limiting case of a non-rotating central object. Therefore the discussion focuses on the influence of the central object's spin on the existence and locations of the charged structures. Frame dragging effects result in the existence of rigidly rotating polar clouds, which do not exist in the non-rotating case. Counter-rotating equatorial tori are preferred over co-rotating ones in the case of a rapidly spinning central object.

List of Publications

1. K. Schroven, E. Hackmann, and C. Lämmerzahl. Relativistic Dust Accretion of Charged Particles in Kerr-Newman Spacetime. *Phys. Rev. D*, 96:063015, 2017

2. A. Trova, K. Schroven, E. Hackmann, V. Karas, J. Kovář, and P. Slaný. Equilibrium Configurations of a Charged Fluid around a Kerr Black Hole. *Phys. Rev. D*, 97: 104019, 2018

3. K. Schroven, A. Trova, E. Hackmann, and C. Lämmerzahl. Charged Fluid Structures around a Rotating Compact Object with a Magnetic Dipole Field. *Phys. Rev. D*, 98:023017, 2018

Contents

List of Figures

List of Tables

Notation

The metric signature $(-,+,+,+)$ will be used.

,	$A_{,\mu}$ denotes the partial derivative of A by μ
;	$A_{;\mu}$ denotes the covariant derivative of A by μ
$'$	$f'(s)$ denotes the derivative of a function $f(s)$ by s
(..)	$T_{(\mu\nu)}$ denotes the symmetric part of the Tensor $T_{\mu\nu}$
[..]	$T_{[\mu\nu]}$ denotes the anti-symmetric part of the tensor $T_{\mu\nu}$
$*$	${}^*T^{\alpha\beta}$ denotes the dual of the tensor $T^{\mu\nu}$
$\dot{}$	$\dot{x}$ denotes the derivative of x with respect to proper time
$\ddot{}$	$\ddot{x}$ denotes the second derivative of x with respect to proper time

Chapter 1

Introduction

1.1 Astronomy – Observation of the Power Houses

All along humans are fascinated, anytime they take a gander at the star-bright night. The history of astronomy therefore is a long one. In its beginnings observations of the night sky were used for time determination and navigation, next to its great religious importance. While passing major milestones from the invention of the telescope four hundred years ago to the start of applying spectroscopy to the kickoff of gravitational wave astronomy just recently [4], astronomy gained its solely scientific character and developed into what we know it as today.

The observable universe contains processes with conditions that could never be created in any laboratory on earth. Along with it comes the possibility to test theories on a whole different level. The theory of General Relativity, introduced 1915 by Albert Einstein, could finally predict the correct course of Mercury, where the Newtonian theory failed, and was further confirmed by an observation of light bending through the sun, that was consistent with Einstein's theory.

In the 1960s the new field of relativistic astrophysics saw a boost after the new methods of radio and X-ray astronomy opened the full range of the electromagnetic spectrum and lead to the observations of quasi stellar radio sources (quasars) and x-ray sources, such as Cygnus X-1 (Cyg X-1), where relativistic effects had to be taken into account in order to understand the processes behind these emissions. Cause of the new found energy sources were accretion processes. Not nuclear burning – the energy source of a sun – but the extraction of gravitational potential energy from material, which is accreted on a gravitating body, is responsible for many phenomena observed in astronomy today. While this energy source is ineffective for objects such as our sun, where nuclear burning

exceeds accretion by a factor of several thousand, the more compact an object is the more energy can be extracted from infalling material. In the end the accretion onto the most compact objects, speaking neutron stars or black holes, provides a power supply several times larger than what a sun of comparable mass could accomplish.

Initially neutron stars and black holes were seen as purely theoretical objects, which are not actually realized in nature. But with the interpretation of the new observations in the sixties as accretion processes onto (supermassive) black holes or neutron stars, and the discovery of pulsars, the point of view changed. The detection of gravitational waves, which fitted perfectly well the structure predicted for black hole and neutron star mergers, was further strong evidence for their existence [4, 5].

The main criteria of a black hole is the presence of an event horizon, which causally separates a local region of spacetime – the black hole – from the rest. No information can be passed from the spacetime region behind the event horizon to the outer universe. A very compact mass can create such a state, by deforming spacetime so strongly, that even light cannot defy its gravitational effects in a certain local region of spacetime around it. Stellar massive black holes with a mass of $\sim 1 - 100\, M_\odot$ can form through the collapse of massive stars at the end of their life span, when nuclear burning drops and with it the radiation pressure, that is needed to stabilize the star against its own gravitation. Supermassive black holes ($\sim 10^5 - 10^{10}\, M_\odot$) are expected to exist in the center of most galaxies. The process behind their formation could not finally be settled until now. Observations point to their existents already several hundred million years from big bang and it is difficult to explain how they could form that fast. According to the no-hair theorem every black hole is fully characterized by only three properties: mass, spin and charge [6]. While the determination of mass and spin of observed black hole candidates is a major topic in astronomy, the charge is in general expected to be extremely small, due to the enormous strength of electromagnetic effects compared to the gravitational ones [1].

Neutron stars are another possible final state of large stars after their death with initial masses of $\sim 10 - 30\, M_\odot$. Degenerate neutron gas pressure stabilizes the core of the old star and prevents it from a collapse into a black hole. Stars with higher masses will eventually result in the formation of a black hole at the end of their lives. This restricts possible masses for neutron stars to $\sim 3\, M_\odot$. Their exact matter of state is unclear, but the detection of the neutron star merger 2017 puts new light on the subject. Some neutron stars produce strong magnetic fields with up to 10^{11} T, which are then also known as magnetars [7]. Highly magnetized rotating neutron stars are better known as pulsars, if they emit beams of electromagnetic radiation. If the beam is repeatedly

[1] see Sec. 2.2.1.1 for more details

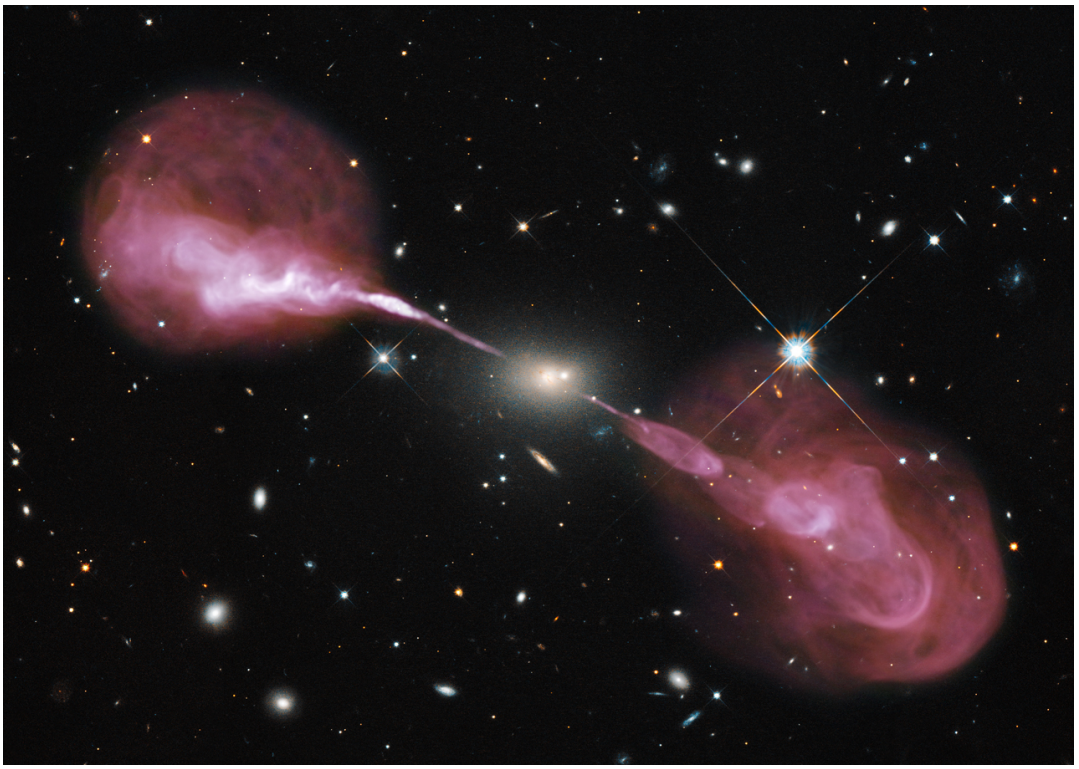

FIGURE 1.1: Multi-wavelength view of radio galaxy Hercules A. Very prominent in the picture are the two radio jets in reddish, which expand deep into space, with their source galaxy Hercules A between them. Credits: NASA, ESA, S. Baum and C. O'Dea (RIT), R. Perley and W. Cotton (NRAO/AUI/NSF), and the Hubble Heritage Team (STScI/AURA)

pointing towards us, due to the rotation of the pulsar, it is detected as a pulsed signal. The high stability of their rotation make pulsars very precise clocks and led to the method of pulsar timing. Pulsar timing was also used to detect the orbital decay in the probably most famous pulsar binary PSR B1913+16 or Hulse–Taylor binary, which could be interpreted as the first indirect evidence for gravitational waves [8].

Many of the high-luminosity phenomena in the universe are traced back to accretion processes, which can take place in several different environments. First of all there are active galactic nucleis (AGNs), which the already mentioned quasars belong to. AGNs are apparently stellar sources with a non-thermal spectrum. They are located at the center of so called active galaxies, and are very compact with a size of around $1-10$ pc [9], while outshining the entire rest of its host galaxy with bolometric luminosities of around $\sim 10^{47}\mathrm{erg\,s^{-1}}$ [10]. As such they are the most powerful steady energy sources in the known universe, deserving the name power houses of the universe. Their emission can range through the whole electromagnetic spectrum from radio (radio-loud AGNs) to UV to X-ray up to gamma ray radiation. The only possible explanation for these observations is an accretion process driven by a supermassive black hole of $10^6 - 10^{10}\,M_\odot$ in its center. Some AGNs emit radio jets in opposite directions, which are oriented perpendicular to

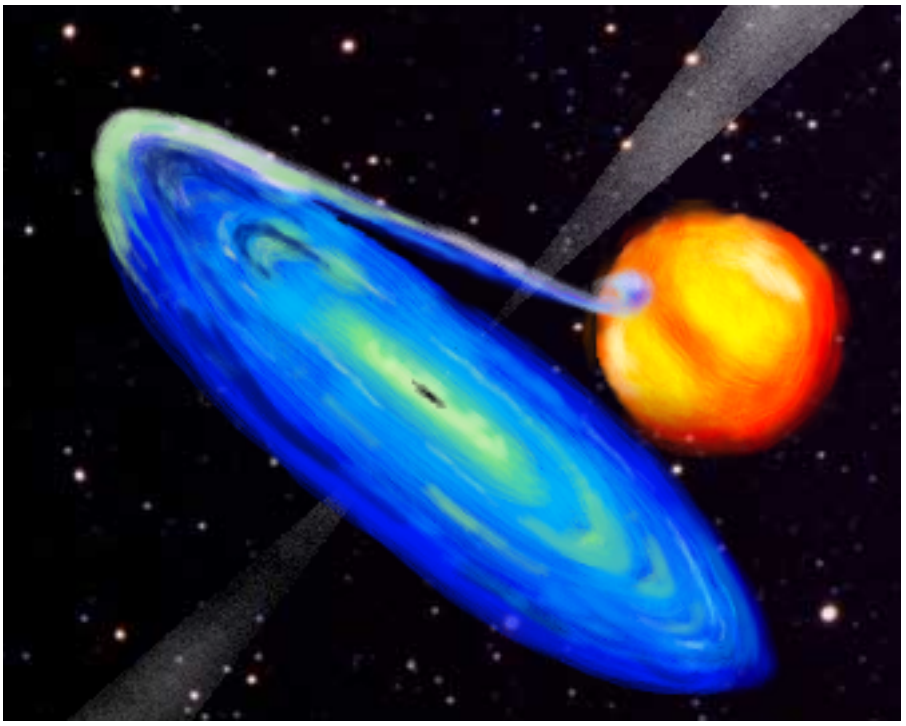

FIGURE 1.2: Schematic picture of an exemplary X-ray binary. In orange the companion star, which loses matter in a Roche lobe overflow. In blue the created accretion disc, with the compact star at its center. Jets are ejected perpendicular to the disc.

the plane of accretion. These jets emit particles at high speeds, close to the speed of light even, and small opening angles of a few degrees, extending up to 300 kpc into space [11]. The process leading to their existence is believed to involve magnetohydrodynamic and electrodynamic effects caused by the presence strong electromagnetic fields in the near-horizon region of the spinning supermassive black hole [12]. A multi-wavelength view of radio galaxy Hercules A, with its big radio jets is shown in Fig. 1.1. Another environment for accretion processes are binary systems. Most stars in binaries will undergo a mass transfer at some point in their evolution. The mass transfer from a "normal" star to its compact companion can be initiated due to various reasons (growth of the "normal" star during its evolution in life, or reduction of the separation between the companions), so that the gravitational pull of the compact star removes outer layers of the companion. This process is known as Roche lobe overflow. An accretion disc is build in the process around the compact star, where the matter heats up and results in a radiation in the X-ray spectrum. These binaries are specified as X-ray binaries, with Cyg X-1 being a prominent member [9, 13]. A schematic picture of the X-ray binary is given in Fig.1.2.

1.2 The Accretion Process

Cosmic matter mainly exists in the form of plasma. It is the main ingredient of suns or interstellar nebulae [14, 15]. So independently of how the accreted matter is supplied, it is expected to be in the plasma state. Different ways to describe the astrophysical plasma are introduced later in Sec. 2.3. Rotating inflows of matter – which would be the general scenario – will eventually flatten out and form an accretion disc [16]. The matter of the disc has to transport angular momentum outwards in order to move closer to the gravitational center, while releasing energy, and be actually accreted. Viscous effects are therefore needed in accretion processes. They extract energy from the system, help to move angular momentum outwards, and are therefore cooling the matter. However, the resulting radiation causes a radiation pressure, which hinders the accretion process by pushing the disc material outwards. From this interplay the Eddington limit is derived, a limit on the maximal luminosity an accretion process can generate. In some accretion systems the maximal luminosity predicted by the Eddington limit is expected to be nearly reached. The knowledge about their luminosity turns these systems into standard candles, which are used in many methods for determining distances to far away objects in space [9].

Phenomena, that are traced back to accretion processes, show a variety of electromagnetic spectra, thermal or non-thermal ones, that sometimes contain X-ray or radio parts. In order to describe the underlying processes of these phenomena, very different accretion models are required. Analytic models and numerical simulations go hand in hand for the task of understanding the accretion processes, that can cause this variety of spectra. While the analytical models provide the basic concept and understanding of the processes, numerical simulations are required, where the analytic models reach their limits due to their simplicity.

The discussion of accretion processes started with the most basic case of spherical accretion of an ideal, polytropic gas. The model was first examined 1952 by Bondi [17] in an Newtonian approach and later generalized to a general relativistic (GR) treatment by Michel in 1972 [18], who further gives first estimates on the realized temperatures and luminosities that could be reached in the process. The importance of rotation of the accreted matter was invoked into accretion theories, after spherical accretion was found to have a very low efficiency in converting potential energy to radiation [19]. This finally led the way to accretion discs.

The first treatment of the formation of accretion discs was studied 1976 by Ulrich [20]. He discussed the infall of rotating dust onto a central object, starting at a rotating spherical shell located infinitely far away. The model depicts a reflection symmetry with

respect to a plane perpendicular to the dust cloud's rotation axis. Matter is treated as dust, if all types of particle interactions are neglected and the particles are considered to be in free fall. According to the model, a disc will form in the symmetry plane, since all dust particles will eventually collide at this plane with a counterpart particle, which has its origin in the opposite hemisphere. The relativistic extension of Ulrich's model was introduced 2001 by Illarionov and Beloborodov [21]. The model was further modified by moving the location of the spherical shell to finite radii by Tejeda et al. (2012) [22], which allows for more general boundary conditions. In this work a black hole charge is added to the model and applied on charged particles, in order to take the effects of realistic electric black hole charges onto plasma accretion into account.

The most prominent disc model surely is the standard thin disc model introduced by Shakura and Sunyaev [23], which was transferred to the relativistic description by Novikov and Thorne [24]. Viscosity is treated in this model by a simple constant parameter (known as the α-prescription of viscosity). Limits to the value of α are estimated using the dimensions of the accretion disc. The thin disc model assumes that all energy extracted by the accretion process is locally completely radiated away. This leads to a rather small accretion rate due to the high radiation pressure. Thin discs have – as the name suggests – a small hight to radius ratio $z/r \ll 1$. They are comparably cold ($T \sim 10^4 - 10^7 K$) and optically thick, leading to a thermal radiation spectrum.

The estimates for the viscosity parameter in the thin disc model cannot be explained by ordinary molecular viscosity, since it is to weak for astrophysical processes. Another source could be turbulence driven by the magneto-rotational instability (MRI). Weak magnetic fields in the disc power turbulent fluctuations in the accreted matter. In numerical shear box simulations estimations for the α-parameter were derived based on the MRI with varying results. Many numerical simulations of accretion discs are based on the thin disc model and take stresses in the fluid matter into account only in terms of the α-parameter (see [25] and references within).

In contrast to the thin disc model, the slim disc model allows cooling in form of advection. Not all extracted energy is directly radiated away, but a part is captured inside the disc, and the disc blows up, leading to hight to radius ratios of $z/r \leq 1$. The necessity for higher luminosities and accretion rates lead to this model [25].

Carried to the extremes is that way of cooling in advection dominated accretion flows (ADAFs). Advection dominates the cooling process in this model. The accretion disc is hot and optically thin. In the result no typical thermal spectrum is radiated, but one that contains the spectra of bremsstrahlung, synchrotron radiation (magnetic fields are present) and their comptonized parts [25].

Some measured spectra from binary systems show thermal and non-thermal parts. In order to explain them sufficiently, an inner hot disc surrounded by a truncated standard thin disc was suggested to model the accretion flow in these systems. This combination was first introduced 1976 by Shapiro et al. [26] and further developed in later years. The accretion flow of binaries with a black hole companion can have different spectral states. Depending on the accretion rate, a quiescent state is present, if the accretion flow can be described solely by a hot accretion flow, for which Sagittarius A* (Sgr A*) in the center of our own galaxy is a good example. In the hard and intermediate state a hot disc is build up in the inner parts, while being surrounded by the standard thin disc. In the thermal state the accretion flow can be described solely in the thin disc model [25].

In order to describe the full picture of an accretion process in the fluid approach GR magnetohydrodynamics (MHD) has to be considered, including turbulences, radiation processes, nuclear burning and more. Its simulation therefore requires a large range of scales. Some important effects, like the mentioned MRI, have to be simulated on very small scales, while the interpretation of observational phenomena demands a discussion of very large scales. The computational expense rises enormously, if the number of considered dimensions is increased. It is absolutely necessary to reduce the computational costs by different methods and assumptions. Various different codes like HARM, ZEUS, ATHENA or COSMOS++ exist, based on hydrodynamics, (ideal) MHD or even (ideal) GRMHD, that approach the simulation of accretion processes with different models or simplifications. Numerical simulations are also a good way to check a given model for instabilities like Rayleigh-Taylor instability, Papaloizou–Pringle instability or thermal and viscous instability [25].

The simplest way to describe geometrically thick accretion discs in a GR setting is in form of toroidal configurations, which are constructed by considering a perfect fluid, effected only by the spacetime geometry of the accreting object. They were introduced by Paczyński and his collaborators in a series of publications [27, 28, 29], which yielded to their name “Polish Donuts”. Their theoretical foundation will be introduced in Sec. 2.5. The distribution of angular momentum inside the thick disc is free to choose and determines the disc structure. For simplicity reasons it is often set to be constant. Other, non-constant angular momentum distributions, however, are highly motivated, since they avoid instabilities, that occur in the constant case, and lead to a large variety of disc structures, from rather flat to very expanded discs [30, 31]. They can be used to describe a broader range of accretion disc scenarios. The simplicity of the model motivates to study the properties of a range of more complex spacetimes with it, that have no direct adaptation in classical astrophysics [32, 33, 34, 35]. Furthermore, the Polish Donut model often finds adaptation as an initial condition for numerical simulations. It is also used to simulate radiation spectra, e.g. for Sgr A* in our galactic center [36].

Magnetic fields are supposed to play major roles in accretion disc processes. They are needed to trace viscosity effects in the discs back to the MRI, or to understand jet formation. The mere fact, that mostly plasma is accreted promotes their presence. This motivates to add magnetic fields to the simple Polish Donut model. The ground was broken by Komissarov [37], who constructed a thick disc with a toroidal magnetic field and by that opened the model to discussions of magnetic effects in thick accretion discs [38, 39]. The model was further extended by external electric and magnetic fields acting on an electrically charged fluid [40, 41, 42]. Within this setting arose the possibility for polar clouds. The combination of electromagnetic and GR effects in thick accretion discs can be discussed in this setting, which is also where a major part of this work focuses on.

1.3 Aim of the Work

Three parameters characterize the exterior of a black hole according to the no-hair theorem: Its mass, spin and charge. The estimates on realistic black hole charges are small on long timescales, but can be big on short ones [43, 44, 45]. Charged black holes are considered very seriously as an important factor in selected astrophysical processes, especially in the recent years [46, 47, 48, 49, 50]. How does the presence of electric charge influence GR accretion processes onto compact objects is the key question this work tackles. To do this the work specializes on two scenarios.

While the black hole mass and spin are commonly taken into account in (relativistic) accretion models and numerical simulations, the black hole charge is in general assumed to be negligible, since realistic estimations point to very small net charges of black holes [2]. The first scenario treated in this work is devoted to discuss, which influence realistically small black hole charges can have on accretion processes. To do that the modified and GR version of Ulrich's model [22] is adapted in Kerr-Newman spacetime.

Electromagnetic fields are likely to be present during accretion processes, either produced in the process of accretion, or by the accreting object, e.g. by a magnetar. The second scenario is devoted to the question, how the structure of an accretion disc is affected, if it has a non-vanishing charge distribution, while being exposed to external electromagnetic fields. This scenario was discussed for non-rotating central objects and different external magnetic fields by Kucáková et al. [40], Kovář et al. [41, 42] in the Polish Donut model in the idealized case of a non-conducting fluid. The second major part of this work focuses on how rotation of the central object and the accompanying relativistic effects changes the picture.

[2] see Sec. 2.2.1.1 for more details

The structure of this thesis is as follows. In Chapter 2 the basic theory of the discussed subjects is introduced. Chapter 3 focuses on the first scenario and the influence of small net charges on the accretion process, while Chapter 4 treats the second scenario about the structure and existence of charged accretion discs in the vicinity of a magnetic dipole field produced by a central, spinning object. A summary is given in Chapter 5, concluding remarks, an outlook and open questions are stated in Chapter 6.

Chapter 2

Theoretical Foundation

2.1 Coming from Einstein's Equations

Every general relativistic treatment of a physical problem begins with the Einstein equations

$$G_{\mu\nu} + \Lambda g_{\mu\nu} = \frac{8\pi G}{c^4} T_{\mu\nu}\,, \tag{2.1}$$

which contain the gravitational constant G and the speed of light c. The first term $G_{\mu\nu}$ is called Einstein tensor. It can be expressed in terms of the spacetime metric $g_{\mu\nu}$, the Ricci-tensor $R_{\mu\nu}$ and the Ricci-scalar R, both contractions of the Riemann curvature tensor:

$$G_{\mu\nu} = R_{\mu\nu} - \frac{1}{2} g_{\mu\nu} R\,. \tag{2.2}$$

Constructed only out of contractions of the Riemann curvature tensor and the metric, the Einstein tensor is a measure of spacetime geometry.

Skipping the second term, the explanation of Eq. (2.1) turns to the stress-energy tensor $T_{\mu\nu}$ on the right-hand side. $T_{\mu\nu}$ acts as the source term of gravity and contains the knowledge of energy density, momentum density and stress at a point in spacetime (called event). It is symmetric in μ, ν. The demand for conservation of energy-momentum results in the conservation law

$$T^{\mu\nu}{}_{;\nu} = 0\,. \tag{2.3}$$

Lastly, the term $\Lambda g_{\mu\nu}$ contains the cosmological constant Λ. The influence of the cosmological constant only plays a role in a cosmological context. Its effects are totally negligible on the scale of galaxies or stars. This term is written down in (2.1) only for completeness and will be set to zero in the following.

The focus of this work lies on the relativistic description of charged accretion processes. The Einstein Eqs. (2.1) have therefore to be solved for a stress-energy tensor containing the electromagnetic fields and matter contribution of both the central object as well as the accreted matter.

The stress-energy tensor of an electromagnetic field $T^{\mu\nu}_{(em)}$ is given by

$$T_{(em)_{\mu\nu}} = -\frac{1}{\mu_0}\left(F_{\mu\alpha}F_{\nu}{}^{\alpha} - \frac{1}{4}g_{\mu\nu}F_{\alpha\beta}F^{\alpha\beta}\right) , \tag{2.4}$$

where μ_0 is the magnetic constant. $F_{\alpha\beta}$ is the electromagnetic field tensor, introduced initially for the formulation of Maxwell's equations in Minkowski spacetime. In the general relativistic case they take the form

$$\begin{aligned} F_{[\alpha\beta;\gamma]} &= 0 \qquad \textit{homogeneous Maxwell equations} , \\ F^{\alpha\beta}{}_{;\beta} &= \mu_0 j^{\alpha} \quad \textit{inhomogeneous Maxwell equations} . \end{aligned} \tag{2.5}$$

j^{α} is called four-current density, the source term of the electromagnetic field. Due to the first relation in (2.5), the electromagnetic field tensor can be expressed in terms of a four-potential A_{α}

$$F_{\alpha,\beta} = A_{\beta,\alpha} - A_{\alpha,\beta} . \tag{2.6}$$

By using the Maxwell equations (2.5) one derives the following expression for the left-hand side of the conservation law (2.3) [6]:

$$T^{\mu\nu}_{(em)_{;\nu}} = -F^{\mu\alpha}j_{\alpha} . \tag{2.7}$$

The right-hand side of the above equation can be seen as electric force ($F^{0\alpha}j_{\alpha}$), and Lorentz force ($F^{b\alpha}j_{\alpha}$, $b = 1, 2, 3$) density. In case of a vacuum this term obviously has to vanish, since j_{α} vanishes, and the conversation law is satisfied.

If matter is involved, it is possible to introduce a further stress-energy tensor $T^{\mu\nu}_{(matter)}$ representing the inner energy and momentum density and stress of the matter. If external forces are present, they will appear as a force density on the right-hand side of

$$T^{\mu\nu}_{(matter)_{;\nu}} = f^{\mu} , \tag{2.8}$$

such that $T^{\mu\nu}_{(matter)}$ is not conserved. In case of charged matter one can now identify the external force density f^{μ} as the electric and Lorentz force density from Eq. (2.7) acting on the matter. This leads to a total stress-energy tensor

$$T^{\mu\nu}_{(tot)} = T^{\mu\nu}_{(em)} + T^{\mu\nu}_{(matter)} , \tag{2.9}$$

which will then satisfy the conservation law (2.3)

$$T^{\mu\nu}_{(tot)_{;\nu}} = 0\,. \tag{2.10}$$

To set up an accretion model, for which the above equations can be solved analytically, making assumptions about the accreted matter, the accreting object, as well as their interactions, is absolutely necessary. For instance, different plasma models can be used to describe the accreted matter and simplify the accretion model's equations with it. Which plasma model to choose depends on the scenario one wants to discuss. The same is valid for the description of the accreting object. The following section is dedicated to hint the different possibilities of describing astrophysical plasma, while going into details, where it is needed, to understand the used accretion models later on in Sec. 3 and 4.
[6, 51]

2.2 Electromagnetic Fields in Curved Spacetime

When discussing plasma or in general charged matter in a GR treatment, electromagnetic fields have to be considered in curved spacetimes. They contribute to the Einstein equations (2.1) through an electromagnetic part $T^{\mu\nu}_{(em)}$ in the source term $T^{\mu\nu}$, while the electromagnetic field tensor occurring in $T^{\mu\nu}_{(em)}$ on the other hand has to satisfy Maxwell's equations. The non-linear set of Einstein and Maxwell equations can be solved analytically in special cases or under certain approximations. Two of them will be introduced here, as they are used later on.

In electrovacuum the stress-energy tensor only contains terms connected to the electromagnetic field, and has no matter related parts. The Einstein field equations with such a stress-energy tensor are known as Einstein-Maxwell equations:

$$G_{\mu\nu} = -\frac{8\pi G}{c^4}\frac{1}{\mu_0}\left(F_{\mu\alpha}F_{\nu}{}^{\alpha} - \frac{1}{4}g_{\mu\nu}F_{\alpha\beta}F^{\alpha\beta}\right) \qquad \textit{Einstein-Maxwell equations}\,. \tag{2.11}$$

The stress-energy tensor has to satisfy the conservation law (2.3), in a way that the four-current density j^{α} in the inhomogeneous Maxwell Eqs. (2.7) vanishes and an electrovacuum is described. The corresponding Maxwell equations, that have to be satisfied as well, are then given by Eq. (2.5) for $j^{\alpha} = 0$.

2.2.1 The Kerr-Newman Solution

By assuming spherical symmetry, one expects the line element ds^2 to take the following form in spherical coordinates $(\bar{t}, \bar{r}, \bar{\theta}, \bar{\phi})$,

$$ds^2 = e^{\lambda(\bar{r},\bar{t})} d\bar{t}^2 - e^{2\nu(\bar{r},\bar{t})} d\bar{r}^2 - \bar{r}^2 \left(d\bar{\theta}^2 + \sin\left(\bar{\theta}\right)^2 d\bar{\phi}^2 \right) . \tag{2.12}$$

When the two functions $\lambda(\bar{r}, \bar{t})$ and $\nu(\bar{r}, \bar{t})$ are determined by satisfying the Einstein-Maxwell equations (2.11), one derives the Reissner-Nordström solution for an electromagnetic field that is static and spherically symmetric. It was found by Hans Reissner and Gunnar Nordström already in 1916 and 1918 [52, 53]. The solution can be expanded from a static, spherical metric to the stationary, axially symmetric Kerr-Newman metric, by a complex coordinate transformation [54]. The metric of a stationary and axially symmetric spacetime can be written in the following form by using a spherical polar coordinate system:

$$ds^2 = g_{tt}\, dt^2 + 2g_{t\phi}\, dt\, d\phi + g_{rr}\, dr^2 + g_{\theta\theta}\, d\theta^2 + g_{\phi\phi}\, d\phi^2 . \tag{2.13}$$

Specifying to Boyer-Lindquist coordinates, the Kerr-Newman metric takes the form

$$ds^2 = \frac{\rho^2}{\Delta} dr^2 + \rho^2 d\theta^2 + \frac{\sin^2(\theta)}{\rho^2} \left[\left(r^2 + a^2 \right) d\phi - a\, c\, dt \right]^2 - \frac{\Delta}{\rho^2} \left[a \sin^2(\theta)\, d\phi - c\, dt \right]^2 , \tag{2.14}$$

where

$$\rho^2(r, \theta) = r^2 + a^2 \cos^2(\theta) , \tag{2.15}$$

$$\Delta(r) = r^2 - 2Mr + a^2 + Q^2 + P^2. \tag{2.16}$$

This metric describes a black hole if $M^2 > a^2 + Q^2 + P^2$ and otherwise a naked singularity with a ring singularity at $\rho^2(0, \pi/2) = 0$ and a coordinate singularity at $\Delta(r) = 0$, which is satisfied for

$$r_\pm = M \pm \sqrt{M^2 - Q^2 - P^2 - a^2} . \tag{2.17}$$

r_+ and r_- are called inner and outer horizon, respectively. The black hole is stationary and axially symmetric, since the metric coefficients do neither depend on t nor ϕ. Furthermore the black hole possesses a reflection symmetry with respect to $\theta = \pi/2$.

The associated electromagnetic field tensor is expressed by the following electromagnetic potential:

$$\begin{aligned} A = A_\nu dx^\nu =& \frac{c^2}{\sqrt{4\pi\varepsilon_0 G}} \left\{ \frac{Qr}{\rho^2} \left(dt - a\sin^2(\theta)\, d\phi \right) + \frac{1}{\rho^2} P\cos(\theta) \left(a dt - (r^2 + a^2) d\phi \right) \right\} \\ =:& \frac{c^2}{\sqrt{4\pi\varepsilon_0 G}} \tilde{A}_\nu dx^\nu \,. \end{aligned} \tag{2.18}$$

Like the metric the electromagnetic potential is stationary and axially symmetric. Its components A_ν therefore neither depend on t or ϕ. However, in case of $P \neq 0$ the reflection symmetry at $\theta = \frac{\pi}{2}$, that is present for the metric, does not show up in the electromagnetic potential.

By the Gaussian flux integrals one can identify Q, M and a as related to the total electric charge q, the total mass m and the angular momentum J of a black hole by

$$a = \frac{J}{mc} \,, \tag{2.19}$$

$$M = \frac{Gm}{c^2} \,, \tag{2.20}$$

$$Q^2 = \frac{q^2 G}{4\pi\varepsilon_0 c^4} \,, \tag{2.21}$$

with ε_0 referring to the electric constant [6]. The assumption of magnetic monopoles allows to write the Maxwell equations in a particularly symmetric form. The homogeneous Maxwell equations then turn into inhomogeneous ones of the form ${}^*F^{\alpha\beta}{}_{;\beta} = \mu_0 j^\alpha_{(m)}$, where $j^\alpha_{(m)}$ is the magnetic four-current density produced by magnetic monopoles, and ${}^*F_{\alpha\beta} = \frac{1}{2} F^{\mu\nu} \varepsilon_{\mu\nu\alpha\beta}$ is the dual of the electromagnetic field tensor F. Parameter P, which appears in the Kerr-Newman metric and the associated electromagnetic potential, can be identified to be related to the magnetic monopole of the black hole, by calculating the Gaussian flux integral as for Q, but for the dual ${}^*F$ of the electromagnetic field tensor [55, 6].

The ergoregion is defined as the area in which local observers cannot be at rest, but must move in line with the rotation of the black hole. The ergoregion coincides with $g_{tt} \leq 0$, which is satisfied for

$$r \leq M \pm \sqrt{M^2 - Q^2 - P^2 - a^2 \cos(\theta)^2} \,. \tag{2.22}$$

The Kerr-Newman metric is the most general solution of the Einstein-Maxwell equations for a stationary, axially symmetric black hole [56]. This is also expressed in the no-hair theorem, which states, that the exterior of a black hole is described by three parameters

only: charge, mass and angular momentum. The Kerr-Newman spacetime includes three limiting cases: Reisner Nordström spacetime, for which the angular momentum of the black hole vanishes ($a = 0$), Kerr spacetime, for which the charges of the black hole vanish ($Q = P = 0$), and Schwarzschild spacetime, for which both, charges and angular momentum are zero ($a = Q = P = 0$). Together they form the Kerr-Newman family of solutions.

2.2.1.1 Astrophysical Restrictions on the Black Hole Charge

In the first instance the electric net charge of a black hole receives an upper limit by demanding the existence of an event horizon (see Sec. 2.2.1). This restriction allows electric net charges up to $Q = M$. For these net charges the electromagnetic force acting on a charged particle is excessively stronger than the gravitational effects. A non-relativistic treatment leads to an electric-gravitational force ratio of

$$\frac{f_{(em)}}{f_{(grav)}} = \frac{\epsilon}{\sqrt{4\pi\varepsilon_0}\mu_p} \sim 10^{18}$$

for a proton with a mass μ_p [57]. Therefore black holes with non-vanishing net charges are commonly dismissed with the argumentation, that these black holes would be immediately discharged by a selective accretion of opposite charged particles. Errant charges in the vicinity of the black hole are absorbed by the interstellar medium. Following this argumentation only electric net charges are expected whose resulting force is compensable by gravitational effects, leading to

$$\mu M \gtrsim \frac{\epsilon Q}{\sqrt{4\pi\varepsilon_0}} \qquad \Rightarrow \qquad Q \lesssim 10^{-18} - 10^{-21} M\,, \tag{2.23}$$

for the accretion of protons and electrons respectively [57, 48]. Still, black holes might tend to display very small positive net charges below the given restriction (2.23), since protons are slightly preferred during plasma accretion due to their bigger masses [48].

The picture changes considerably, however, when introducing magnetic fields. Rotating black holes can be charged, if located in an external magnetic field, as shown by Wald [45]. The electric net charge favored by the black hole depends on the strength of the magnetic field, and is not limited by the restriction (2.23) given above. A trapping of charged particles in the magnetosphere of a black hole could also stop the selected accretion of opposite charged particles and lead to net charges bigger than the restriction (2.23) [58]. Furthermore, magnetized or charged stars will also collapse into an electrically charged black hole [59, 60].

Still, in all these cases the electric net charge of the black hole could be limited due to the spontaneous charge loss of charged black holes because of pair production close to the black hole horizon [61]. It can be derived, that it leads to a restriction of the net charge to [62]

$$Q < 10^{-5} \frac{M^2}{M_\odot},$$

where $M_\odot$ is the value of M (see Eq. (2.20)) for the solar mass.

Nevertheless even very small net charges, that fulfill the restriction (2.23), have a noticeable effect on the accretion process, as will be discussed in Sec. 3. Its noticeable influence on the bremsstrahlung profile of SgrA* is used by Zajaček et al. [48] to derive an upper limit for the net charge of SgrA*.

2.2.2 Electromagnetic Test-fields

When one wants to describe electromagnetic fields in the vicinity of a compact object the Einstein equations (2.1) have to be solved, with the stress-energy tensor containing an electromagnetic part (2.4). In the electrovacuum case – e.g. for a black hole as the compact object– the Einstein-Maxwell equations (2.11) have to be solved, as it was done to derive the Kerr-Newman solution previously. In general, however, it is not possible to solve the Einstein-Maxwell equations analytically. Electromagnetic fields strong enough to significantly influence the spacetime curvature are rare to build up in realistic scenarios (see the previous discussion in Sec. 2.2.1.1). Hence, in most cases it is a good approach to assume, that the electromagnetic field is weak enough, so that it can be treated as a test-field, meaning its influence on the spacetime can be neglected. The Einstein equations can then be solved without the electromagnetic contribution to the stress-energy tensor, and the Maxwell equations (2.5) are solved afterwards in the found background spacetime.

The outer Schwarzschild and Kerr metric are solutions to the vacuum field equations ($T^{\mu\nu}_{(matter)} = T^{\mu\nu}_{(em)} = 0$). Both metrics can be obtained from the Kerr-Newman metric (2.14) by setting both charges, P and Q, to zero, as well as, in case of Schwarzschild, angular momentum a.

In the test-field approximation, an electromagnetic field in the vicinity of a rotating black hole can be described by the Kerr metric and an electromagnetic potential A^μ derived from the Maxwell equations (2.5) on the Kerr background.

By using the Newman-Penrose approach Teukolsky [63] was able to show, that the source-free Maxwell equations are separable in r and θ on a Kerr background if stationarity and axial symmetry is assumed [1]. They can then be solved in terms of Legendre functions $P_l(u), Q_l(u)$ and their associated Legendre polynomials $P_l^m(u), Q_l^m(u)$, where u is either a function of r or $\cos(\theta)$ [65, 66].

A transformation back into Boyer-Lindquist coordinates results in the general outer solution $A_\alpha = \frac{c^2}{\sqrt{4\pi\varepsilon_0 G}}\tilde{A}_\alpha$ of a
stationary and axially symmetric electromagnetic potential on Kerr background[66]:

$$\begin{aligned}\tilde{A}_t =& -\frac{r(Q+\zeta)}{\rho^2} - \sum_{l=1}^{\infty}\left\{\frac{\Delta(r)}{\rho^2}Q_{l,r}\left(\frac{r-1}{\xi}\right)P_l\left(\cos(\theta)\right)\left(r\beta_l^r - a\cos(\theta)\beta_l^i\right)\right.\\ &\left.+\frac{a}{\rho^2}Q_l\left(\frac{r-1}{\xi}\right)\sin(\theta)P_l^1\left(\cos(\theta)\right)\left(a\cos(\theta)\beta_l^r + r\beta_l^i\right)\right\}, \qquad (2.24)\\ \tilde{A}_\phi =& \frac{ar(Q+\zeta)}{\rho^2}\sin^2(\theta) + \sum_{l=1}^{\infty}\left\{\frac{a\Delta(r)}{\rho^2}Q_{l,r}\left(\frac{r-1}{\xi}\right)P_l\left(\cos(\theta)\right)\sin^2(\theta)\left(r\beta_l^r - a\cos(\theta)\beta_l^i\right)\right.\\ &+\frac{r^2+a^2}{\rho^2}Q_l\left(\frac{r-1}{\xi}\right)\sin(\theta)P_l^1\left(\cos(\theta)\right)\left(a\cos(\theta)\beta_l^r + r\beta_l^i\right)\\ &\left.-\frac{\Delta(r)}{l(l+1)}Q_l\left(\frac{r-1}{\xi}\right)P_l^1\left(\cos(\theta)\right)\sin(\theta)\beta_l^i\right\}, \qquad (2.25)\end{aligned}$$

where $\xi = r_+ - 1 = \sqrt{1-a^2}$. The inner solution can be derived from the outer one (2.24),(2.25) by replacing $Q_l(u)$ with $P_l(u)$, $\beta_l^{r,i}$ with $\alpha_l^{r,i}$, and adding a further constant α_t to the expression (2.24) of A_t [65, 66]. Furthermore $\zeta = \hat{\zeta}\sqrt{G}/(\sqrt{4\pi\varepsilon_0}c^2)$ corresponds to the total charge $\hat{\zeta}$ of a charge distribution lying between the inner and outer source-free solution. It has therefore be set to zero in the expression of the inner solution. The coefficients $\alpha_l = \alpha_l^r + i\alpha_l^i$ and $\beta_l = \beta_l^r + i\beta_l^i$ are complex constants. They can be derived from matching the inner and outer solution at the position of the source charge (e.g. a current loop) [66].

The electromagnetic potential of a Kerr-Newman black hole is reproduced from expression (2.24) and (2.25) by keeping only the monopole ($l = 0$) term and expecting no charge distribution between the inner and outer solution ($\zeta = 0$).

2.2.2.1 The Dipole Magnetic Test-field in Kerr Spacetime

Bičák and Dvořák [67] showed, that the electromagnetic test-field of an elementary magnetic dipole oriented along the rotation axis is equivalent to that of a small current loop with a vanishing net charge ($Q + \zeta = 0$) in the equatorial plane. The coefficients

[1] For an introduction into the Newman-Pensrose approach, as well as for the derivation of the separation of Maxwell's equations in Newman-Penrose coordinates see [64].

β_l and α_l can be calculated for such a charge distribution. The dipole-component of the electromagnetic field is given by the $l = 1$-term in Eqs. (2.24) and (2.24). The corresponding coefficients β_1^r and β_1^i are given by [68, 66]

$$\beta_1^r = 0, \qquad \beta_1^i = -\frac{3}{2}\frac{B}{\xi^2}\,. \tag{2.26}$$

Looking at the behavior of A_t, A_ϕ at large radii, one can identify B as the magnetic dipole moment.

With this considerations one derives $A_\alpha^{(dipole)}$, the
electromagnetic potential of a dipole magnetic test-field in Kerr spacetime:

$$\tilde{A}_t^{(dipole)} = -\frac{3}{2}\frac{aB}{\xi^2\rho^2}\left[-r + \cos^2(\theta) + \frac{1}{2\xi}\ln\frac{r-1+\xi}{r-1-\xi}\Big(r(r-1) + (a^2-r)\cos^2(\theta)\Big)\right], \tag{2.27}$$

$$\tilde{A}_\phi^{(dipole)} = -\frac{3}{4}\frac{B\sin^2(\theta)}{\xi^2\rho^2}\left[(r-1)\rho^2 + 2\,r\,(r+a^2) - \frac{1}{2\xi}\ln\frac{r-1+\xi}{r-1-\xi}\,\Big(\Sigma - 4\,r\,a^2\Big)\right], \tag{2.28}$$

where $\Sigma = (r^2+a^2)^2 - \Delta(r)a^2\sin^2(\theta)$ [68].

The frame dragging effect in Kerr spacetime connects the ϕ- and t- component in the metric's description (Eq. (2.14), $Q = P = 0$). This leads to the A_t-component in the description of a magnetic dipole field, which will cause, according to (2.37), an electric part in the dipole field for an observer at rest.

With an expansion of the logarithmic term in $A_\phi^{(dipole)}$ in $\frac{1}{r}$ (see Appendix B), it can be shown, that for $B > 0$, $0 \le a < 1$ and for all θ

$$A_\phi^{(dipole)} > 0, \text{for all } r > r_+\,, \tag{2.29}$$

while $A_t^{(dipole)}$ changes sign, depending on θ:

$$A_t^{(dipole)} \le 0 \qquad \text{for } r > r_+, \theta = \pi/2\,, \tag{2.30}$$

$$A_t^{(dipole)} \ge 0 \qquad \text{for } r > r_+, \theta = 0\,. \tag{2.31}$$

In case of $a = 0$, the electromagnetic potential is reduced to a magnetic dipole test-field in Schwarzschild spacetime [69]

$$\tilde{A}_t^{(dipole)} = 0\,, \tag{2.32}$$

$$\tilde{A}_\phi^{(dipole)} = -\frac{3}{4}B\sin^2(\theta)\left(r + 1 - \frac{r^2}{2}\ln\frac{r}{r-2}\right). \tag{2.33}$$

Here the potential only contains a ϕ-component and the electric component of the field vanishes.

In the extremal Kerr case ($a = 1$), the electromagnetic potential simplifies greatly to [70]

$$\tilde{A}_t^{(dipole)} = -\frac{B}{2(r-1)^2\rho^2}\left(r\sin^2(\theta) - 2\,(r-1)\cos^2(\theta)\right)\,, \tag{2.34}$$

$$\tilde{A}_\phi^{(dipole)} = -\frac{B\sin^2(\theta)}{2(r-1)^2\rho^2}\left((r-1)\left(r+\cos^2(\theta)\right) - 2\,r^3\right)\,. \tag{2.35}$$

The magnetic and electric field of the electromagnetic potential should behave as dipole and quadrupole fields in flat spacetime, respectively. This leads to A_t falling off faster than A_ϕ for an increasing radial component r.

2.3 Description of Plasma

Plasma is composed of partly or fully ionized gas, and builds the fourth fundamental state of matter. It is in general treated as quasi-neutral, showing no total charge. To differentiate plasma from the classical gaseous state, where also a minor fraction of gas particles are always ionized, plasma is defined as a state, where the long range Coulomb interaction between the charged particles leads to a collective behavior of the ionized gas. This adds to the individual interactions of particles, such as collisions [71, 15].

Depending on the condition a plasma occurs in (expressed among others by its diluteness and particle velocities), a certain plasma type can be assigned to it. Some prominent types are mentioned here:

- In hot or thermal plasma collisions dominate the particle interaction so that the plasma is locally in thermodynamic equilibrium. The fluid description can be used for this plasma type, and properties like pressure and temperature can be declared.
- In a two-temperature plasma the electron and ion distributions have reached a thermodynamic equilibrium due to ion-ion and electron-electron collisions separately, but the plasma is not in an overall thermodynamical equilibrium, which would be reached by a sufficiently high electron-ion collision rate. The two-fluid approach considers this by treating electron and ion distributions as separate fluids, which can then have different temperatures and pressures. The evolution of the two fluids is coupled by long range electromagnetic interactions.
- In case of a cold or non-thermal plasma thermodynamic equilibrium is not reached either by the ions or by all particle types. The collision rate between ions or

all plasma particle types is not frequent enough, and the long range Coulomb interaction dominates the plasma behavior. A fluid description is not possible, but a kinetic description might be used.

- In collisionless plasmas collisions between the plasma particles are so rare, that they can be neglected compared to the long range Coulomb interaction. A kinetic or a test-particle description could be adaptable.
- A non-neutral plasma has, as the name suggests, a non-vanishing total charge. The arising electromagnetic field will strongly affect the plasma behavior.
- A dusty plasma does not depict electrons and ions, but charged dust.

Obviously, different mathematical approaches are required for the different plasma types ranging from a fluid description over a kinetic description to a test-particle description of the plasma. In the following the relativistic versions of this descriptions are shortly introduced, after stating some notations on particle motion and electromagnetic fields in four dimensional spacetime.

The motion of a particle is described by a curve $x^\alpha(s)$ in spacetime in the coordinate system x^α, $\alpha = 0..3$. The curve is parametrized by an affine parameter s. The proper time τ in the particles rest frame is often used to parametrize its curve. The four-velocity $\dot{x}^\alpha$ and four-acceleration $\ddot{x}^\alpha$ of the particle are then defined by

$$\dot{x}^\alpha = u^\alpha = \frac{d}{d\tau}x^\alpha \qquad\qquad \ddot{x}^\alpha = \frac{d^2}{d\tau^2}x^\alpha \,. \tag{2.36}$$

In the GR treatment electric (E_α) and magnetic (B_α) fields seen by an observer with a four-velocity $u^\mu_{(obs)}$ can be specified by

$$E_\alpha = F_{\alpha\beta}u^\beta_{(obs)} \,, \qquad\qquad B_\alpha = -\frac{1}{2}\varepsilon_{\alpha\beta}{}^{\delta\gamma}F_{\delta\gamma}u^\beta_{(obs)} \,, \tag{2.37}$$

where $\varepsilon_{\alpha\beta}{}^{\delta\gamma}$ is the Levi-Civita tensor.

Test-particle approach The term test-particles refers to particles, that do not effect the spacetime in which they are located, and just react to it. They are therefore in a way "testing" the spacetime by moving in it. For very diluted plasmas it might be reasonable to describe each plasma particle separately as a test-particle with a charge ϵ, moving within an electromagnetic field described by $F^{\mu\alpha}$. Collisions between plasma particles are completely neglected, but electric and Lorentz-forces

$$-F^{\mu\alpha}J_\alpha \tag{2.38}$$

act on the test-particle, where

$$J^\alpha = \epsilon\, \dot{x}^\alpha \tag{2.39}$$

is the four-current assigned to the charged test-particle with the four-velocity $\dot{x}^\alpha$.

Kinetic Approach Within a kinetic or a fluid approach one treats the plasma particle movement statistically. For that (covariant) distribution functions $\mathcal{F}(x^\mu, p^\mu)$ are introduced, that describe the plasma's electron and ion motion. A combination of the Boltzmann and Maxwell equations (where the Maxwell equations enter the collisionless Boltzmann equation as external forces) determines the evolution of the distribution function. Introduced in the classical limit by A. A. Vlasov in 1938, the self-consistent set of differential equations has various different names [72] but will here be called Vlasov-Maxwell equations:

$$\begin{aligned} \frac{\partial \mathcal{F}}{\partial s} = \dot{x}^\mu \frac{\partial \mathcal{F}}{\partial x^\mu} + \epsilon \frac{\partial \mathcal{F}}{\partial p^\mu} F^{\mu\nu} \dot{x}_\nu = 0\,, \\ F^{\alpha\beta}{}_{;\beta} = f^\alpha_{(source)}\,, \end{aligned} \qquad \textit{relativistic Vlasov-Maxwell equations.} \tag{2.40}$$

where $f^\alpha_{(source)}$ is the source term of the electromagnetic field created by the plasma particles. The collision term of the Boltzmann equation is neglected in Eq. (2.40). [73].

A kinetic approach is reasonable, if the plasma is not in thermal equilibrium, and a fluid approach is not adaptable. It is used for diluted plasmas containing particles with high velocities such as cold or collisionless plasmas.

Fluid Approach In this approach plasma is viewed as an electromagnetic fluid, and can therefore be described in the theory of MHD, or its GR generalization GRMHD. The interaction between the fluid and its electromagnetic field is expressed in the total stress-energy tensor (2.9), composed of a fluid and an electromagnetic term. The stress-energy tensor for a perfect fluid [74]

$$T^{\mu\nu}_{(ifluid)} = \frac{1}{c^2}\left(p g^{\mu\nu} + (\varepsilon + p) U^\mu U^\nu\right) \tag{2.41}$$

is often used as the matter term $T^{\mu\nu}_{(matter)}$ in $T^{\mu\nu}_{(tot)}$. It neglects shear and bulk viscosities of the fluid as well as energy fluxes. p and ε are the pressure and energy density of the fluid, respectively. U^α is the four-velocity of the fluid [2].

Central equations of GRMHD are the conservation of rest-mass

$$(\rho_m U^\mu)_{;\mu} = 0\,, \tag{2.42}$$

[2] A lower case u denotes the four-velocity of a single particle, while a capital letter U denotes the statistical quantity of a fluid four-velocity

where ρ_m is the rest-mass density, and energy-momentum (2.10). The second leads to

$$(\varepsilon + p)\,\dot{U}_\nu + h^\mu_\nu \partial_\mu p = h^\mu_\nu F_{\mu\alpha} j^\alpha \,, \tag{2.43}$$

after a projection of Eq. (2.10)

$$T^{\mu\nu}_{(tot)_{;\nu}} = 0 \rightarrow T^{\mu\nu}_{(ifluid)_{;\nu}} = -T^{\mu\nu}_{(em)_{;\nu}} \tag{2.44}$$

orthogonal to the fluid four-velocity by using the projection tensor

$$h_{\mu\nu} = c^2\, g_{\mu\nu} + U_\mu U_\nu \,, \qquad\qquad h_{\mu\alpha} U^\alpha = 0 \,. \tag{2.45}$$

Equations (2.42) and (2.43) have to be solved together with Maxwell's equations (2.5). The four-current density j^α is decomposed into a term parallel and orthogonal to U^α

$$j^\alpha = \rho_q U^\alpha + \sigma F^{\alpha\beta} U_\beta \,. \tag{2.46}$$

The first term describes the part of j^α, which arises from the motion of the fluid with charge density ρ_q. The second term is the conduction current $j^\alpha_{(c)}$. Its strength is determined by the conductivity σ of the fluid.

In the approach of ideal MHD the set of differential equations (2.42), (2.43), (2.5) are simplified by the assumption of an infinite conductivity of the fluid or rather plasma. An infinite conductivity leads to the demand

$$F^{\alpha\beta} U_\beta = 0 \,, \tag{2.47}$$

to keep the conduction current (second term in Eq. (2.46)) finite. This leads to a vanishing Lorentz-force $F^{\mu\alpha} j_\alpha = \rho_q F^{\mu\alpha} U_\alpha = 0$ acting on a fluid, which is analogous to a vanishing electric field in the rest-frame of the fluid. While the inhomogeneous Maxwell equation (2.5) is used to determine j_α, the homogeneous Maxwell equation describes the evolution of the electromagnetic field.

More detailed information on the theory of GRMHD can be found in [75, 76, 77], where the focus lies especially on the numerical approach of solving the introduced set of differential equations.

The test-particle and fluid approach are adapted for two different accretion scenarios in the later sections 2 and 3.

2.4 Charged Particles in the Vicinity of a Charged, Rotating Black Hole

A charged particle moving in the vicinity of a charged, rotating black hole is described by a charged test-particle moving in Kerr-Newman spacetime. To derive the particle motion the equations of motion have to be set up first, then separated, and in the end solved by elliptic functions.

2.4.1 Equations of Motion in Kerr-Newman Spacetime

In contrast to uncharged particles, that follow geodesic motion, the Lorentz force acts on charged particles, causing them to be accelerated. For a particle with an electric charge ϵ, mass μ and a four-velocity $\dot{x}^\alpha$ the equations of motion in Kerr-Newman spacetime are (see Eqs. (2.39),(2.38))

$$\mu\, \ddot{x}_\nu = F_{\nu\alpha} J^\alpha = \epsilon\, F_{\nu\alpha} \dot{x}^\alpha \,. \tag{2.48}$$

$F_{\nu\alpha}$ can be derived from the electromagnetic potential (2.18) by using Eq. (2.6).

A first step to solve the given equations of motion analytically is to decouple the equations. One way to accomplish that is to express equation (2.48) in terms of a Hamiltonian H and the Hamilton equations of motion

$$\dot{q}^\sigma = \frac{\partial H}{\partial \pi_\sigma} \,, \qquad\qquad \dot{\pi}_\sigma = -\frac{\partial H}{\partial q^\sigma} \,, \tag{2.49}$$

which further induces the Hamiltonian property

$$\frac{d}{d\tau} H = \frac{\partial}{\partial \tau} H \,. \tag{2.50}$$

q^σ and π_σ are the generalized coordinates and momenta respectively.

The Hamiltonian can be derived from the Lagrange function $\mathcal{L}$. The Lagrange function on the other hand has to be chosen such that the Euler-Lagrange equations reproduce the equations of motion (2.48). In this case it takes the form

$$\mathcal{L} = \frac{1}{2} g_{\mu\nu} \dot{x}^\mu \dot{x}^\nu - \hat{\epsilon}\, A_\mu \dot{x}^\mu \,, \tag{2.51}$$

where $\hat{\epsilon} = \epsilon/\mu$ is the specific charge. Here the Boyer-Lindquist coordinates x^α are used as the generalized coordinates $\dot{q}^\alpha$. The Hamiltonian is connected to the Lagrange function

as follows:

$$H = \pi_\sigma \dot{q}^\sigma - \mathcal{L}\,, \qquad \pi_\sigma = \frac{\partial \mathcal{L}}{\partial \dot{q}^\sigma}\,. \tag{2.52}$$

The Hamiltonian for the given dynamical system now reads

$$H = \frac{1}{2} g^{\mu\nu} \left(\pi_\mu + \hat{\epsilon}\, A_\mu\right) \left(\pi_\nu + \hat{\epsilon}\, A_\nu\right)\,, \qquad \pi_\sigma = \dot{x}_\sigma - \hat{\epsilon} A_\sigma\,. \tag{2.53}$$

Stationarity and axial symmetry of both the Kerr-Newman metric (2.14) as well as the electromagnetic potential (2.18) causes the metric and potential components to neither depend on t and ϕ. The second Hamilton equation in (2.49) therefore yields to two constants of motion:

$$\begin{aligned} c^2 E = \frac{\mathbf{E}}{\mu} &= -\pi_t = -g_{tt}\dot{t} - g_{t\phi}\dot{\phi} + e\,\tilde{A}_t\,, \\ c\,l = \frac{L}{\mu} &= \pi_\phi = +g_{t\phi}\dot{t} + g_{\phi\phi}\dot{\phi} - e\,\tilde{A}_\phi\,. \end{aligned} \tag{2.54}$$

E and l are the specific energy and the angular momentum in direction of the rotation axis, connected, as given, to the energy $\mathbf{E}$ and angular momentum L in direction of the rotation axis of a particle with a mass μ. The specific charge parameter e is related to the particle charge by $e = \frac{\epsilon}{\mu\sqrt{4\pi\varepsilon_0 G}}$. Since H does not explicitly depend on τ, the Hamiltonian itself is a further constant of motion (see (2.50)). It can be identified as the normalization condition for the four-velocity, and is therefore set to $H = -c^2$:

$$-c^2 = g_{\mu\nu}\dot{x}^\mu \dot{x}^\nu\,. \tag{2.55}$$

The given equation represents the Hamilton-Jacobi equation. Plugging in the found constants of motion (2.54) for the generalized momenta reduces the unknown dynamical variables in the equation to r and θ, and their first derivatives, which have to be separated to solve the equations of motion. To achieve this the Mino time

$$d\lambda = c\rho^{-2} d\tau \tag{2.56}$$

is introduced to equation (2.55) [78]. The central mass M can be eliminated from the equations by the transformation $x = M\bar{x}$, for $x = r, t, a, l, Q, P, d/d\lambda$. The separated

equation now results in:

$$\left(\frac{d\theta}{d\bar{\lambda}}\right)^2 + \bar{a}^2\cos^2(\theta) + \frac{\mathcal{T}^2(\theta)}{\sin^2(\theta)} = \frac{1}{\bar{\Delta}(\bar{r})}\left(\mathcal{R}^2(\bar{r}) - \left(\frac{d\bar{r}}{d\bar{\lambda}}\right)^2\right) - \bar{r}^2 = \bar{K}\,, \tag{2.57}$$

$$\mathcal{T}(\theta) = \bar{a}E\sin^2(\theta) - \bar{l} + \hat{e}\bar{P}\cos(\theta)\,, \tag{2.58}$$

$$\mathcal{R}(\bar{r}) = (\bar{r}^2 + \bar{a}^2)E - \bar{a}\bar{l} - \hat{e}\bar{Q}\bar{r}\,. \tag{2.59}$$

The separation constant $\bar{K}$, known as the Carter constant, is the fourth constant of motion. With as many constants of motion as degrees of freedom the system is integrable, and will not show chaotic motion. [79]

Together with Eqs. (2.54) or the first equation in (2.49), the separated equations of motion (2.57) build the four differential equations for an electrically charged test-particle in a Kerr-Newman spacetime:

$$\left(\frac{d\theta}{d\bar{\lambda}}\right)^2 = \bar{K} - \bar{a}^2\cos^2(\theta) - \frac{\mathcal{T}^2(\theta)}{\sin^2(\theta)} = \Theta(\theta)\,, \tag{2.60}$$

$$\left(\frac{d\bar{r}}{d\bar{\lambda}}\right)^2 = \mathcal{R}^2(\bar{r}) - (\bar{r}^2 + \bar{K})\bar{\Delta}(\bar{r}) = \mathbf{R}(\bar{r})\,, \tag{2.61}$$

$$\frac{d\phi}{d\bar{\lambda}} = \frac{\bar{a}\mathcal{R}(\bar{r})}{\bar{\Delta}(\bar{r})} - \frac{\mathcal{T}(\theta)}{\sin^2(\theta)}\,, \tag{2.62}$$

$$\frac{c\,d\bar{t}}{d\bar{\lambda}} = \frac{(\bar{r}^2 + \bar{a}^2)\mathcal{R}(\bar{r})}{\bar{\Delta}(\bar{r})} - \bar{a}\mathcal{T}(\theta)\,. \tag{2.63}$$

Up until now the parameters c, G, ε_0 and M were explicitly written out in all equations to show how they enter and scale them. From this point on I will follow the common procedure by setting $c = M = G = 4\pi\varepsilon_0 = 1$ in all equations[3]. This will mainly be expressed by skipping the bar, indicating the normalization by M, for all parameters as well as the tilde introduced for the electromagnetic potential.

With the decoupled equations of motion at hand, some statements about the particle motion are already possible. Particle motion is restricted to values of (r, θ), for which $\Theta(\theta), \mathbf{R}(r) \geq 0$. Furthermore, the nodes of $\Theta(\theta)$ and $\mathbf{R}(r)$ describe the location of turning points in the θ and r direction respectively.

The values of the constants of motion (E, l, K) restrict the area in which the particle motion might take place:

- To find any solution for the θ-motion, $K \geq 0$ has to be satisfied.

[3]This corresponds to a description in geometrized units divided by M

- The equatorial plane at $(\theta = \pi/2)$ can only be reached if $C = K - (aE - l)^2 \geq 0$. Otherwise the particle motion will only take place in the northern or southern hemisphere.
- For a motion in the equatorial plane only, $C = 0$ is necessary.
- In case $E^2 > 1$ the polynomial $\mathbf{R}(r) \to \infty$ for $r \to \pm\infty$. This allows a particle motion starting or ending at infinity. For $E^2 < 1$, where $\mathbf{R}(r) \to -\infty$ for $r \to \pm\infty$, the particle motion will always show an upper and lower bound in r.
- In the special case $E^2 = 1$ $\Theta(\theta)$ reduces to a polynomial of degree two so that the θ-motion is solvable by elementary functions. $\mathbf{R}(r)$ reduces to a polynomial of degree three, creating an upper or lower bound of the r-motion for $eQ > 1$ and $eQ < 0$ respectively.
- Because the equations of motion do not change for

$$(l, a, P\cos(\theta)) \to (-l, -a, -P\cos(\theta)),$$

  a discussion of the equations can be restricted to $a > 0$.

An extensive discussion on the properties of the Kerr-Newman equations of motion can be found in Hackmann and Xu [80]. The listing here only includes properties, that are needed later in chapter 3.

For $P \neq 0$ the reflection-symmetry with respect to $\theta = \pi/2$ is broken in the equation of motion for θ (2.60). In the later adaption of the charged test-particle motion in Kerr-Newman spacetime a reflection-symmetry regarding $\theta = \pi/2$ is demanded. This motivates the restriction to $P = 0$ in the following discussions.

2.4.2 The Limit of Big Charges

In the special case, that the product eQ takes extremely big values for a particle motion[4], all terms in the equations of motion (2.60)-(2.63) that do not contain eQ are negligible. In case of initial four-velocities u^α, which are considered small compared to eQ, the

[4]This is e.g. the case for protons or electrons in the vicinity of a black hole with an electric net charge $Q \sim 1$, see Eq. (3.28)

constants of motion reduce in the limit to

$$\mathcal{E} = \frac{E}{e} \approx A_t = \frac{Qr_0}{\rho_0^2}\,, \tag{2.64}$$

$$\mathscr{L} = \frac{l}{e} \approx -A_\phi \approx a\mathcal{E}\sin^2(\theta_0)\,, \tag{2.65}$$

$$\mathscr{K} = \frac{K}{e^2} \overset{\text{Eq.(2.57)}}{\approx} 0\,, \tag{2.66}$$

which leads to the following expression for the equations of motion:

$$\left(\frac{1}{e}\right)^2\left(\frac{d\theta}{d\lambda}\right)^2 \approx -\frac{T^2(\theta)}{\sin^2(\theta)}\,, \tag{2.67}$$

$$\left(\frac{1}{e}\right)^2\left(\frac{dr}{d\lambda}\right)^2 \approx R^2(r)\,, \tag{2.68}$$

$$\left(\frac{1}{e}\right)\frac{d\phi}{d\lambda} \approx \frac{aR(r)}{\Delta(r)} - \frac{T(\theta)}{\sin^2(\theta)}\,, \tag{2.69}$$

where

$$R(r) = \frac{\mathcal{R}(r)}{e} \approx (r^2+a^2)\mathcal{E} - a\mathcal{L} - Qr\,, \tag{2.70}$$

$$T(\theta) = \frac{\mathcal{T}}{e} \approx a\mathcal{E}\left(\sin^2(\theta) - \sin^2(\theta_0)\right)\,. \tag{2.71}$$

Eq. (2.67) can only be satisfied for $T(\theta) = 0$, which corresponds to a particle motion with constant θ, and thus the particle motions stay on a plane. It further simplifies the equation of the ϕ-motion in terms of r to

$$\frac{d\phi}{dr} = \frac{d\phi}{d\lambda}\Big/\frac{dr}{d\lambda} \approx \frac{a}{\Delta(r)}\,. \tag{2.72}$$

From Eq. (2.72) it can immediately be seen, that ϕ is constant for $a = 0$, which corresponds to a radial infall of the test-particle. For $a \neq 0$ the frame dragging acts on the particle motion, which in result deviates from a radial infall. In the extremal case $a = 1$ Eq. (2.72) is solved by

$$\phi - \phi_0\Big|_{a=1} \approx -\frac{1}{r-a} + -\frac{1}{r_0-a}\,. \tag{2.73}$$

In case of $0 < a < 1$ the ϕ-motion is given by

$$\phi - \phi_0 \approx -\frac{a}{\sqrt{1-a^2}}\mathrm{arcoth}\left(\frac{\mathrm{r}-1}{\sqrt{1-\mathrm{a}^2}}\right) + \mathrm{D}\,, \tag{2.74}$$

where D is an integration constant.

2.4.3 Solutions to the Equations of Motion

Differential equations of the form

$$\left(\frac{d\phi}{du}\right)^2 = P(\phi)\,, \tag{2.75}$$

where $P(\phi)$ is a polynomial of order three or four with no multiple roots, can be solved by means of elliptic functions. Elliptic functions have the following characteristic properties:

- Elliptic functions are meromorphic.
- They are defined as the inverse functions of elliptic integrals. The most general form of an elliptic integral is

  $$I = \int_{\phi_0}^{\phi} f\left(z, \sqrt{P(z)}\right) dz = u(\phi)\,,$$

  where $f\left(z, \sqrt{P(z)}\right)$ is a rational function of z and $\sqrt{P(z)}$.
- They are doubly periodic, with the complex periods ω_1 and ω_2. In the real vector space of the complex plane $\mathbb{C}$, ω_1 and ω_2 correspond to two linearly independent periods.

The elliptic integral, whose inverse function solves differential equation (2.75), takes the simple form

$$\int_{\phi_0}^{\phi} \frac{dz}{\sqrt{P(z)}} = u(\phi)\,. \tag{2.76}$$

[81]

Elliptic functions can be expressed in certain basic elliptic functions. The Weierstrass function $\wp(z-c_1)$ is the one that plays the biggest role in the theory of elliptic functions. It satisfies a differential equation of the form

$$\left(\frac{dy}{du}\right)^2 = 4y^3 - g_2 y - g_3\,, \qquad\qquad y(u_0) = y_0\,. \tag{2.77}$$

The Weierstrass invariants g_2, g_3 are determined by the two periods ω_1, ω_2 of the elliptic function $\wp$, while constant $c_1(u_0, x_0) = u_0 + \int_{y_0}^{\infty} \frac{dz}{\sqrt{4z^3 - g_2 z - g_3}}$ is chosen such that the initial conditions are satisfied. To describe the solution of any differential equation of the form in (2.75) in terms of Weierstrass elliptic functions, $P(\phi)$ has to be turned into Weierstrass form $4y^3 - g_2 y - g_3$. If $P(\phi)$ is of order four, the knowledge of one of its roots ϕ_p is necessary to make a substitution of the form $\phi = \xi^{-1} + \phi_p$, and turn $P(\phi)$ into a polynomial of order three $P(\xi) = \sum_{i=0}^{3} b_i \xi$. This can then easily be transformed into

Weierstrass-form, by substituting $\xi = \frac{1}{b_3}\left(4y - \frac{b_2}{3}\right)$. If g_2, g_3 are both real, then $\wp(z)$ will always take real values for real or imaginary z. Weierstrass elliptic functions have been used to solve the equations of motion in Kerr-Newman spacetime (2.60)-(2.63) in [80]. Due to the purpose of use in this work, however, a set of other basic elliptic functions is used to express the solutions to the Kerr-Newman equations of motion, the Jacobi elliptic functions. They are for example used by Tejeda et al. [82] and Fujita and Hikida [83] to describe the motion of a test-particle in Kerr spacetime. [84]

Jacobi elliptic functions are characterized by their special property to show correspondence to the trigonometric functions, and reduce to them in a limiting case. There are three basic Jacobi elliptic functions $\mathrm{sn}(F,k)$, $\mathrm{cn}(F,k)$ and $\mathrm{dn}(F,k)$, that correspond to the height y, the length x and the varying radius of an ellipse. The normal elliptic integral of first kind

$$F(\varphi,k) = \int_0^{\varphi} \frac{d\vartheta}{\sqrt{1-k^2\sin^2(\vartheta)}} \tag{2.78}$$

$$= \int_0^{y=\sin(\varphi)} \frac{dt}{\sqrt{(1-t^2)(1-k^2t^2)}}\,, \tag{2.79}$$

$$= \int_1^{x=\cos(\varphi)} \frac{dt}{\sqrt{(1-t^2)(k'^2+k^2t^2)}}\,, \tag{2.80}$$

$$\vdots$$

can take different forms, depending on the substitution for φ. Its inverse functions are the basic Jacobi elliptic functions

$$\mathrm{sn}(F,k) = \sin(\varphi) = y, \quad \mathrm{cn}(F,k) = \cos(\varphi) = x \quad \text{and} \quad \mathrm{dn}(F,k) = \sqrt{1-k^2\sin(\varphi)^2}\,. \tag{2.81}$$

Numbers k, $k' \in \mathbb{C}$ are referred to as modulus and complementary modulus of the elliptic integral. k' is related to k by $k' = \sqrt{1-k^2}$. All Jacobi elliptic functions show two periods

$$\omega_1 = 2K(k)\,w_1\,, \qquad K(k) = \int_0^{\pi/2} \frac{d\vartheta}{\sqrt{1-k^2\sin^2(\vartheta)}} \tag{2.82}$$

$$\text{and } \omega_2 = 2iK'(k)\,w_2\,, \qquad K'(k) = K(k')\,, \tag{2.83}$$

where the value of $w_{1,2} \in \{1,2\}$ depends on the Jacobi elliptic function. If k^2 is a real number, then one can suppose without loss of generality, that

$$k, k' \in [0,1]\,, \tag{2.84}$$

due to the following transformation rules:

$$\begin{aligned}
\mathrm{sn}(F, ik) &= \sqrt{\frac{1}{1+k^2}}\frac{\mathrm{sn}\left(\sqrt{1+k^2}F, \sqrt{\frac{k^2}{1+k^2}}\right)}{\mathrm{dn}\left(\sqrt{1+k^2}F, \sqrt{\frac{k^2}{1+k^2}}\right)}\,, \\
\mathrm{cn}(F, ik) &= \frac{\mathrm{cn}\left(\sqrt{1+k^2}F, \sqrt{\frac{k^2}{1+k^2}}\right)}{\mathrm{dn}\left(\sqrt{1+k^2}F, \sqrt{\frac{k^2}{1+k^2}}\right)}\,, \\
\mathrm{dn}(F, ik) &= \frac{1}{\mathrm{dn}\left(\sqrt{1+k^2}F, \sqrt{\frac{k^2}{1+k^2}}\right)}\,,
\end{aligned} \tag{2.85}$$

and

$$\begin{aligned}
\mathrm{sn}(F, k) &= \frac{1}{\sqrt{k^2}}\mathrm{sn}\left(k\,F, \frac{1}{\sqrt{k^2}}\right)\,, \\
\mathrm{cn}(F, k) &= \mathrm{dn}\left(k\,F, \frac{1}{\sqrt{k^2}}\right)\,, \\
\mathrm{dn}(F, k) &= \mathrm{cn}\left(k\,F, \frac{1}{\sqrt{k^2}}\right)\,.
\end{aligned} \tag{2.86}$$

In this case the integrals $K(k)$ and $K'(k)$ are both real numbers as well. Furthermore, all three basis Jacobi functions stay in the real domain for a real argument, and $\mathrm{sn}(F, k)$ and $\mathrm{cn}(F, k)$ take values in the range $[-1, 1]$.

Similar to the Weierstrass case, the differential equation (2.75) has to be converted into a certain form to solve it with the Jacobi elliptic function $\mathrm{pq}(u - c_{pq}, k)$ of one's choice. According to the substitution made in (2.78)

$$\left(\frac{dt}{du}\right)^2 = (1-t^2)(1-k^2t^2) \qquad \text{or} \qquad \left(\frac{dt}{du}\right)^2 = (1-t^2)(k'^2+k^2t^2) \tag{2.87}$$

are for example solved by $\mathrm{sn}(u - c_{sn}, k)$ or $\mathrm{cn}(u - c_{cn}, k)$ respectively. The polynomial of the second equation in (2.87) can actually be converted into the polynomial in the first equation by a redefining the modulus $\tilde{k}^2 = -k^2/k'^2$, and scaling it with k'^2. From this one can deduce the transformation rule (by keeping in mind the integration limits for the definition of cn and sn in (2.79),(2.81))

$$\mathrm{sn}(x, k) = \mathrm{cn}\left(k'\,(x - K(k))\,, \sqrt{-\frac{k^2}{k'^2}}\right)\,. \tag{2.88}$$

Again, the constant $c_{pq}(u_0, t_0)$ is used to satisfy the initial conditions $t(u_0) = t_0$. It has to satisfy:

$$c_{pq} = u_0 - pq^{-1}(t_0, k)\,, \tag{2.89}$$

expressing itself as follows for the given examples:

$$c_{sn} = u_0 - \int_0^{t_0} \frac{dz}{\sqrt{(1-z^2)(1-k^2z^2)}}, \quad c_{cn} = u_0 - \int_1^{t_0} \frac{dz}{\sqrt{(1-z^2)(k^2+k'^2z^2)}}. \tag{2.90}$$

The conversion into one of the forms in (2.87) can be accomplished with substitutions of the form

$$\phi = \frac{A_1 + A_2 t^2}{A_3 + A_4 t^2} \text{ or} \tag{2.91}$$

$$\phi = \frac{B_1 + B_2 t}{B_3 + B_4 t}. \tag{2.92}$$

The constants $A_{1..4}$, and $B_{1..4}$ have to be chosen in a way that terms with odd exponents vanish. The knowledge of two roots of the polynomial $P(\phi)$ is necessary to do that. The choice of the constants can be further used to restrict t to the range $t \in [-1, 1]$, and sort the roots of $P(\phi)$. By doing so, differential equation (2.75) can be solved by Jacobi elliptic functions, while working in the real domain $\mathbb{R}$ only. However, $A_{1..4}$, and $B_{1..4}$ depend in this case on all three or four roots of $P(\phi)$.

This was a very brief introduction into the topic of elliptic functions. I recommend the following literature for a deeper view into the subject to the interested reader: Köcher and Krieg [84], Milne-Thomson [85], Byrd and Friedman [81], Bobek [86].

Now the foundation is laid to solve the equations of motion for an electrically charged test-particle in Kerr-Newman spacetime. In the following the equations of motion for r and θ in (2.60)-(2.63) will be solved in terms of Jacobi elliptic functions. The solution for the t- and ϕ-motion will not be needed in the discussions later in Sec. 3 and will therefore not be presented here. The solutions for $t(\lambda)$ and $\phi(\lambda)$ in terms of Weierstrass' $\wp$-, σ- and ζ- function can be found in Hackmann and Xu [80].

2.4.3.1 Solution of the Equation of Motion for r in Terms of Jacobi Elliptic Functions

To reduce the polynomial $\mathbf{R}(r)$, with its four roots $r_{1..4}$, to the first form given in (2.87), a substitution of the form (2.91) is used:

$$r = \frac{r_4 x^2 - n r_1}{x^2 - n} \qquad\qquad n = \frac{r_4 - r_2}{r_1 - r_2}. \tag{2.93}$$

The differential equation then takes the form:

$$\frac{4\left(\frac{dx}{d\lambda}\right)^2}{(1-E^2)(r_1-r_3)(r_2-r_4)} = (1-x^2)(1-k_r^2x^2)\,, \quad k_r^2 = \frac{(r_3-r_4)(r_1-r_2)}{(r_1-r_3)(r_2-r_4)}\,, \tag{2.94}$$

which results in

$$\begin{aligned} r(\lambda) &= \frac{r_1(r_4-r_2)+r_4(r_2-r_1)\,\mathrm{sn}\,(\xi,k_r)^2}{r_4-r_2+(r_2-r_1)\,\mathrm{sn}\,(\xi,k_r)^2}\,, \\ \xi &= -\frac{1}{2}\sqrt{(1-E^2)(r_1-r_3)(r_2-r_4)}\,\lambda - c_{sn}\,. \end{aligned} \tag{2.95}$$

as solution to the differential equation of the r-motion. While the complete expression (2.95) lies always in the real domain for real values of λ, the expression might contain complex quantities, such as complex roots $r_1,..,r_4$ and complex values for $\mathrm{sn}(\xi,\mathrm{k_r})$ or the modulus k_r. Complex quantities in the calculation can be avoided by expressing the found solution with other Jacobi elliptic functions. The big advantage of Jacobi elliptic function is their correspondence to the trigonometric functions. An expression in Jacobi elliptic function with only real quantities can also help to better capture the structure of the found solution, which would not be as obvious if complex quantities are involved.

Four real roots In the case, that $\mathbf{R}(r)$ shows only real roots $r_a > r_b > r_c > r_d$, the roots can always be assigned to $r_1 - r_4$, such that the solution of the r-motion $r(\lambda)$, given in Eq. (2.95), involves only real quantities, which is the case for $x \in [-1,1]$, $k_r < 1$, and $(1-E^2)(r_1-r_3)(r_2-r_4) > 0$. These conditions can be satisfied by the assignment $r_i = \hat{r}_{[(j+v)\mathrm{mod}4]+1}$, $i,j \in [1,4]$, with $\hat{r}_{1..4} = r_{a..d}$, where r_1 and r_2 have to coincide with the roots bordering the range of particle motion. For an unbound orbit in the range $r \in [r_{a,d}, \pm\infty]$, r_1, r_2 correspond to r_d, r_a [5].

In case that two or four roots of $\mathbf{R}(r)$ are complex, substitutions of the form (2.92) can be made so that only real quantities show up in the expression for the solution of the r-motion.

Two real roots In the case of two real $r_a > r_b$ and two complex $r_c, \bar{r_c}$ roots the particle motion is bound and located in between the two real roots for $E^2 < 1$, or unbound and located in the range $r \in [r_{a,b}, \pm\infty]$ for $E^2 > 1$. With the substitution

$$r = \frac{(r_bA - r_aB)x + r_aB + r_bA}{(A-B)x + A + B} \qquad A = \mathrm{Sign}(1-E^2)\sqrt{(r_a-r_c)(r_a-\overline{r_c})}\,, \tag{2.96}$$

$$B = \sqrt{(r_b-r_c)(r_b-\overline{r_c})}\,, \tag{2.97}$$

[5] For the unbound orbit the assignment $r_d = \hat{r}_4 = r_1$ and $r_a = \hat{r}_1 = r_2$ sets v to $v = 0$. Now the other assignments are given by $r_b = \hat{r}_2 = r_3$ and $r_c = \hat{r}_c = r_4$.

one receives the following result for the r-motion, containing only real quantities

$$r(\lambda) = \frac{r_a B + r_b A + (r_b A - r_a B)\,\mathrm{cn}\left(\tilde{\xi}, \tilde{k}_r\right)}{A + B + (A - B)\,\mathrm{cn}\left(\tilde{\xi}, \tilde{k}_r\right)}\,, \quad \tilde{k}_r^2 = \frac{(r_a - r_b)^2 - (A - B)^2}{4AB} \tag{2.98}$$

$$\tilde{\xi} = \sqrt{(E^2 - 1)\,AB}\,\lambda - c_{cn}\,. \tag{2.99}$$

No real roots In the case of four complex roots $r_q = r_{q_1} + i r_{q_2}, r_c = r_{c_1} + i r_{c_2}, \overline{r_q}, \overline{r_c}$, $E > 1$ has to hold in order to find solutions for the r-motion. With the substitution

$$r = r_{q_2}\frac{x - g_1}{g_1 x + 1} + r_{q_2}\,, \tag{2.100}$$

$$g_1 = \sqrt{\frac{4r_{q_2}^2 - (A' - B')^2}{(A' + B')^2 - 4r_{q_2}^2}}\,, \quad A' = \sqrt{(\overline{r_q} - r_c)(r_q - \overline{r_c})}\,, \quad B' = \sqrt{(r_q - r_c)(\overline{r_q} - \overline{r_c})}\,, \tag{2.101}$$

one receives the following result for the r-motion, containing only real quantities

$$r(\lambda) = r_{q_2}\frac{\mathrm{sc}\left(\xi', \hat{k}_r\right) - g_1}{g_1 \mathrm{sc}\left(\xi', \hat{k}_r\right) + 1} + r_{q_2}\,, \quad \hat{k}_r^2 = \frac{4\,AB}{(A + B)^2} \tag{2.102}$$

$$\xi' = \frac{1}{2}\sqrt{(E^2 - 1)}(A + B)\,\lambda - c_{sc}\,. \tag{2.103}$$

Special case $E = 1$ In this case $\mathbf{R}(r)$ reduces to a polynomial of degree three. The solution for this special case can be realized by calculating the limit

$$\lim_{E \to 1, r_0 \to \infty} r(\lambda)\,, \tag{2.104}$$

where r_0 is the fourth root of $\mathbf{R}(r)$ that moves to infinity as the pre-factor $E^2 - 1$ of the r^4-term approaches zero. By choosing $r_b = r_0$, and using

$$\lim_{E \to 1}(E^2 - 1) r_0 = -2(1 - eQ)$$

equation (2.95) reduces to

$$r(\lambda) = \frac{r_1 - r_4 \mathrm{sn}^2\left(\xi_l, k_{rl}\right)}{\mathrm{cn}^2\left(\xi_l, k_{rl}\right)}\,, \qquad k_{rl}^{\,2} = \frac{r_4 - r_3}{r_1 - r_3}\lambda - c_{sn}\,, \tag{2.105}$$

$$\xi_l = \frac{1}{2}\sqrt{2(1 - eQ)(r_1 - r_3)}\,. \tag{2.106}$$

Again this solution can in general contain complex quantities. This is avoided by taking the $(E \to 1)$-limit of an expression for $r(\lambda)$ without any complex quantities. The given function stays in the real domain for a particle motion between r_1 and infinity [22, 81].

2.4.3.2 Solution of the Equation of Motion of θ in Terms of Jacobi Elliptic Functions

In order to express $\Theta(\theta)$ as a polynomial of order four, the substitution $y = \cos(\theta)$ is used first. One receives:

$$\left(\frac{dy}{d\lambda}\right)^2 = \Theta_y(y) = (1-y^2)(K-ay^2) - \left(aE(1-y^2) - l + ePyx\right)^2 . \tag{2.107}$$

This polynomial can be solved by the exact same procedure introduced to receive the solution $r(\lambda)$ in the section before. However, if the magnetic monopole is set to zero, $\Theta_y(y)$ reduces to a polynomial that only consists of terms with even exponents:

$$\left(\frac{dy}{d\lambda}\right)^2 = \Theta_y(y) = a^2(1-E^2)y^4 - \left(C + a^2(1-E^2) + l^2\right)y^2 + C . \tag{2.108}$$

A further substitution of the form (2.91) or (2.92) is not necessary in this case. It is more straight forward to use a substitution of the form

$$x = \frac{y}{y_a} , \qquad \text{with} \qquad y_a = \cos(\theta_a) \in \mathbb{R}, \Theta_y(y_a) = 0 , \tag{2.109}$$

that shifts the roots of $\Theta_y(y)$ to 1 and $-k_\theta^{-2}$, and converts $\Theta_y(y)$ into the form (2.87):

$$\frac{\cos(\theta_a)^2}{C}\left(\frac{dx}{d\lambda}\right)^2 = (1-x^2)(1-k_\theta^2 x^2), \qquad k_\theta^2 = -\frac{a^2(E^2-1)}{C}y_a^4 , \tag{2.110}$$

which can be solved by

$$\cos(\theta)\cos(\theta_a)\,\mathrm{sn}\left(\frac{\sqrt{C}}{\cos(\theta_a)}\lambda - c_{sn}, k_\theta\right) . \tag{2.111}$$

Like in the last discussion of the r-motion, one might want to express the solution $\theta(\lambda)$ of the θ-motion by functions, that only contain real quantities. With the specific substitution used here, this is only possible if $\theta_a \in \mathcal{R}$, and if the motion is located in the area $[\theta_a, \pi - \theta_a]$, for which $x \in [-1, 1]$ is always satisfied. Because of its symmetry in y, $\Theta_y(y)$ will show four real roots in this case. Furthermore, $k \in [0, 1]$ needs to be satisfied, and the first argument of the elliptic function has to be a real number. Depending on the value of the constants of motion this is fulfilled for different Jacobi elliptic functions, presented in the following.

Case 1: $E < 1$**,** $C > 0$**:** The solution given in (2.111) has only real arguments, if one picks the root of $\Theta_y(y)$, that borders the θ-motion as value for θ_a.

Case 2: $E > 1$**,** $C > 0$**:** In this case, k_θ, defined in (2.111), is imaginary. By using the transformation given in Eq. (2.88), one gets

$$\cos(\theta) = \cos(\theta_a)\mathrm{cn}\left(\frac{\sqrt{C + a^2(E^2-1)\cos^4(\theta_a)}}{\cos(\theta_a)}\lambda - c_{cn}, \tilde{k}_\theta\right), \tag{2.112}$$

with a $\tilde{k}_\theta^2 = -\frac{k_\theta^2}{1-k_\theta^2}$, that obviously stays in the range $0 < \tilde{k}_\theta^2 < 1$.

Case 3: $E > 1$**,** $C < 0$**:** Expression

$$\cos(\theta) = \cos(\theta_a)\mathrm{dn}\left(a\sqrt{E^2-1}\cos(\theta_a), \frac{1}{\tilde{k}_\theta}\right), \tag{2.113}$$

will act in the real domain only in this case. It can be derived from Eq. (2.112) by using the second transformation rule in (2.86).

Case 4: $C = 0$**:** Solutions can only be found for $E > 1$ and $l^2 < a^2(E^2-1)$. Eq. (2.108) reduces to

$$\left(\frac{dy}{d\lambda}\right)^2 = \left(a^2(1-E^2)y^2 - \left(a^2(1-E^2) + l^2\right)\right)y^2, \tag{2.114}$$

which can be solved with

$$\cos(\theta) = \frac{4\left(a^2(E^2-1) - l^2\right)e^{-(\lambda-\lambda_0+\lambda(\theta_0))\sqrt{a^2(E^2-1)-l^2}}}{4\left(a^2(E^2-1) - l^2\right) + e^{-2(\lambda-\lambda_0+\lambda(\theta_0))\sqrt{a^2(E^2-1)-l^2}}}. \tag{2.115}$$

The case $E < 1, C < 0$ can only occur for complex roots of $\Theta_y(y)$ and is therefore not discussed here.

For $E = 1$ k_θ and $\tilde{k}_\theta$ are zero, and the solution for the θ-motion reduces to

$$\frac{\cos(\theta)}{\cos(\theta_a)} = \sin\left(\frac{\sqrt{C}}{\cos(\theta_a)}\left[\lambda - \lambda_0\right] + \arcsin\left(\frac{\cos(\theta_0)}{\cos(\theta_a)}\right)\right) \tag{2.116}$$

for the initial conditions (λ_0, θ_0).

2.4.4 Innermost Stable Circular Orbit in Kerr-Newman Spacetime

Circular orbits are characterized by a vanishing of the first and second derivative of the radial component:

$$\dot{r}(\lambda) = \ddot{r}(\lambda) = 0.$$

The differential equation of r (2.61) can be divided into a kinetic term and an effective potential $V_{eff}(r) = \mathbf{R}(r)$. The conditions for a circular orbit can also be expressed as the conditions $V_{eff}(r) = \frac{d}{dr}V_{eff}(r) = 0$ for an extremum in the radial effective potential. The last stable circular orbit is reached, when the extrema in $V_{eff}(r)$ merge to a saddle

point. This leads to the third condition for innermost stable circular orbits (ISCOs): $\frac{d^2}{dr^2}V_{eff}(r) = 0$.

Thus an expression for the ISCO is received by solving the following set of equations for r and two of the three constants of motion K, E, l (the prime denotes a derivation by the given variable):

$$\begin{aligned} \mathbf{R}(r) &= 0\,, \\ \mathbf{R}'(r) &= 0\,, \\ \mathbf{R}''(r) &= 0\,. \end{aligned} \tag{2.117}$$

A particle motion with a constant angle θ has – analogous to the argumentation above – to fulfill the conditions

$$\Theta(\theta) = 0 \qquad \text{and} \qquad \Theta'(\theta) = 0\,. \tag{2.118}$$

In the special case of a vanishing magnetic monopole ($P = 0$), the second equation in Eq. (2.118) is automatically fulfilled for $\theta = \pi/2$ due to the reflection symmetry along the equatorial plane, and the fist equation can be satisfied for

$$K = (aE - l)^2\,, \tag{2.119}$$

fixing the last constant of motion.

Four different ISCO solutions r_{ISCO} are expected for every set of spacetime parameters $(a, |eQ|, Q)$, corresponding to the direct and retrograde orbit of a charged test-particle with the same $eQ > 0$ and a charged particle with opposite charge $eQ < 0$ of the central black hole.

The three conditions in Eq. (2.117) can be solved analytically is case of a Schwarzschild or Kerr black hole (see e.g. [6] and [87]), having one solution

$$r_{\mathrm{ISCO,SS}} = 6$$

in Schwarzschild and two solutions in Kerr, one for the direct and another for the retrograde orbiting particle, both depending on a. The three conditions cannot be solved analytically for a charged test-particles in Kerr-Newman. In appendix A Eqs. (2.117) are reduced to a complicated expression for $\sqrt{K}$, which is then solved numerically.

For very small values of the black hole net charge Q the influence on the spacetime curvature is vanishingly small ($Q \to 0$) so that it can be neglected in the metric coefficients

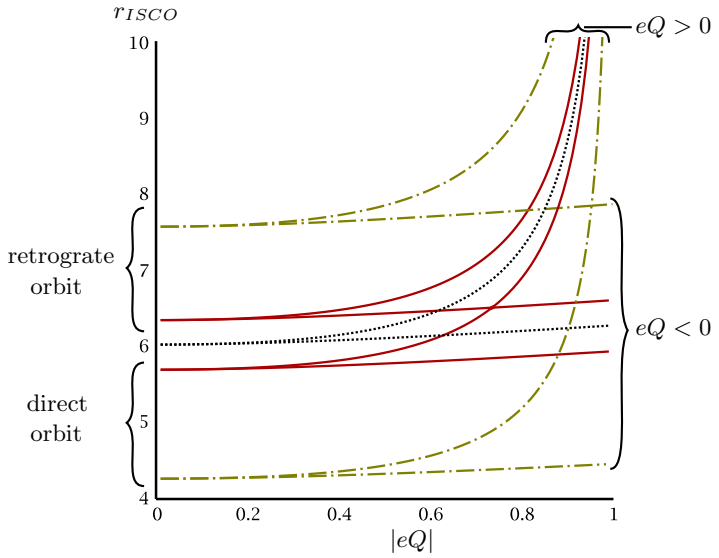

FIGURE 2.1: ISCO radii in the equatorial plane for particles with charge e in Kerr-Newman spacetime with a very small net charge $Q \approx 0$. Depicted are the Reissner-Nordström ($a = 0$) limit (black dotted lines), as well as $a = 0.1$ (red solid lines) and $a = 0.5$ (blue dash-dotted line). Four different solutions arise for a spinning black hole, traced back to the four combinations of direct and retrograde particle motion and $eQ < 0$ or $eQ > 0$. For all cases the ISCO grows for bigger $|eQ|$-values, but significantly faster in the case that black hole and test-particle have the same charge ($eQ > 0$).

($\Delta(r) \to r^2 - 2r + a^2$). However, the test-particles still interact with the electromagnetic field of the black hole, which means that the product eQ is not negligible ($eQ \neq 0$ for $Q \to 0$). In this case the electromagnetic field is treated as a test-field (see Sec. 2.2.2).

The four ISCO solutions presented in Fig. 2.1 as a function of $|eQ|$ and different values of spin a are calculated in the test-field approach ($eQ \neq 0$, $Q \to 0$). In the Reissner-Nordström limit two ISCO solution are found. Starting at the Schwarzschild limit ($|eQ| = 0$) at $r_{\mathrm{ISCO}} = 6$, both solutions $eQ > 0$ and $eQ < 0$ move to bigger radii for bigger values of $|eQ|$, causing r_{ISCO} to be minimal for uncharged particles. The same behavior can be seen for the four ISCO solutions for $a \neq 0$, two starting at $|eQ| = 0$ at each Kerr-ISCO. For $eQ > 0$ the ISCO diverges at $eQ \to 1$, and no ISCO can be found for $eQ > 1$, whereas for $eQ < 0$ the ISCO grows slowly for bigger values of $|eQ|$.

2.5 Polish Donuts

Instead of treating the accreted matter in the vicinity of a compact object as single test-particles, a fluid description might be more appropriate, depending on the situation one wants to investigate. Pressure forces occur, and the accreted matter will deviate from geodesic motion. The stationary and axially symmetric case of a perfect fluid

orbiting some compact object in circular motion can be solved analytically on a general relativistic basis.

This theory was introduced in the 1970s by Fishbone and Moncrief [27], Abramowicz et al. [28], Kozłowski et al. [29] and further developed in the following decades. Komissarov [37] introduced a toroidal magnetic field to the theory, that appears as an additional pressure term in the equations. External magnetic or electric fields entered the theory by Kovář et al. [88, 41, 42].

This very simplified model of an accretion disc is nowhere close to an actual accretion process. It neglects many important effects that occur in accretion processes, with the negligence of dissipative effects such as radiation, and the correlated lack of actual matter accretion (no radial motion of the fluid) leading the way. Nevertheless, the simplicity of the Polish Donut model helps to generate an understanding of thick accretion discs. It is also widely used as an initial condition for simulations of accretion processes.

2.5.1 The Pressure Equations

The following basic assumptions are at the basis of the accretion disc description in the Polish Donut model.

1. The matter which builds the accretion disc is described by a perfect fluid with a polytroic equation of state.
2. The whole system is stationary and axially symmetric. This accounts to the spacetime metric created by the central object, as well as to the fluid motion or an internal or external electromagnetic field, if present.
3. The fluid motion is even further restricted to a purely circular motion around the compact object. The lack of motion towards the central object actually means, that this model does not describe an actual accretion process.
4. The influence of the accretion disc on the spacetime metric is considered negligible. The fluid building the disk therefore serves as a ”test-fluid”, positioned in a given background spacetime.

The metric of a stationary and axially symmetric spacetime takes the form (2.13) in a spherical polar coordinate system, where all metric coefficients depend of r and θ only: $g_{\mu\nu}{=}g_{\mu\nu}(r,\theta)$. Two commuting Killing vectors $\eta^\mu = \delta^\mu_t$ and $\xi = \delta^\mu_\phi$ can be associated with the named symmetries.

The four-velocity U^μ of a fluid in circular motion can be written in terms of the two Killing vectors

$$U^\mu = U^t \left(\eta^\mu + \omega \xi^\mu\right) . \tag{2.120}$$

The specific angular momentum ℓ and angular velocity ω connect by definition the t- and ϕ- component of the fluid's four-velocity. They are given by

$$\ell \coloneqq -\frac{U_\phi}{U_t}, \qquad\qquad \omega \coloneqq \frac{U^\phi}{U^t} , \tag{2.121}$$

and can be expressed in terms of each other by

$$\ell = -\frac{\omega\, g_{\phi\phi} + g_{t\phi}}{\omega\, g_{t\phi} + g_{tt}} \qquad \text{or} \qquad \omega = \frac{\ell\, g_{tt} + g_{t\phi}}{\ell\, g_{t\phi} + g_{\phi\phi}} . \tag{2.122}$$

The normalization condition for the four-velocity reduces in case of circular motion to

$$\alpha = \left(U^t\right)^2 \left(g_{tt} + 2\omega g_{t\phi} + \omega^2 g_{\phi\phi}\right) =: -\left(U^t\right)^2 \mathcal{P}, \qquad \alpha = -1, 0, 1 , \tag{2.123}$$

where $\alpha = -1, 0, 1$ describes subluminal, luminal and superluminal motion respectively. By choosing the affine parameter s of the fluid motion such that $U^t \in \mathbb{R}$, $\mathcal{P} > 0$ indicates subluminal, $\mathcal{P} = 0$ luminal, and $\mathcal{P} < 0$ superluminal circular motion of the fluid. Equation (2.123) leads to an expression for U^t in terms of ω, which reads for subluminal motion:

$$\left(U^t\right)^2 = \frac{1}{\mathcal{P}} = -\frac{1}{g_{tt} + 2\omega g_{t\phi} + \omega^2 g_{\phi\phi}} . \tag{2.124}$$

The acceleration $\dot{U}_\alpha = U^\beta U_{\alpha;\beta}$ is required to keep the fluid on its circular orbit given by Eqs. (2.120) and (2.124). It results in

$$\dot{U}_\alpha = -\partial_\alpha \ln\left(U^t\right) + \frac{\ell \partial_\alpha \omega}{1 - \omega\ell} . \tag{2.125}$$

[89, 74]

Now that the four-velocity of a fluid in circular motion is derived – leaving solely the distribution of $\omega(r, \theta)$ or $\ell(r, \theta)$ free to choose – the equation for an ideal charged fluid introduced in chapter 2.3 (see Eq. (2.43)) is left to be solved. The equation simplifies due to the assumed circular motion, and now reads:

$$\frac{\partial_\mu p}{p + \varepsilon} = \partial_\mu \ln\left(U^t\right) - \frac{\ell \partial_\mu \omega}{1 - \omega\ell} + \frac{\rho_q}{p + \varepsilon} F_{\mu\alpha} U^\alpha + \frac{1}{p + \varepsilon} \sigma h^\nu_\mu F_{\nu\alpha} F^{\alpha\beta} U_\beta . \tag{2.126}$$

To obtain the equation (2.126) above, $\dot{U}_\alpha$ from Eq. (2.125) was plugged into Eq. (2.43), and

$$\begin{aligned} h^\nu_\mu F_{\nu\alpha} j^\alpha &= h^\nu_\mu F_{\nu\alpha} \left(\rho_q U^\alpha + \sigma F^{\alpha\beta} U_\beta \right) \\ &= \rho_q F_{\nu\alpha} U^\alpha + \sigma h^\nu_\mu F_{\nu\alpha} F^{\alpha\beta} U_\beta \end{aligned}$$

was used.

To preserve the self-consistency of the system, Eq. (2.126) should be stationary, axially symmetric, and not violate the assumption of circular motion, meaning the partial derivatives for $\mu = t, \phi$ have to vanish. This is not automatically fulfilled, since the last term in Eq. (2.126) does not automatically vanish for $\mu = t, \phi$. The requirement to set the last term to zero can be turned into a restriction on the conductivity σ:

$$\sigma h^\nu_\mu F_{\nu\alpha} F^{\alpha\beta} U_\beta = 0 \,. \tag{2.127}$$

This can be satisfied by either assuming an overall vanishing conductivity $\sigma = 0$, or by assuming a direction-dependent conductivity $\sigma = \sigma^\mu_\gamma$ (as done in [90]), leading to a conduction current $j^\alpha_{(c)} = F^{\alpha\beta} U_\beta$, which flows such, that the projection of $F_{\mu\alpha} j^\alpha_{(c)}$ orthogonal to U_μ vanishes :

$$h^\nu_\mu F_{\nu\alpha} j^\alpha_{(c)} = 0 \qquad \Rightarrow \qquad F_{\nu\alpha} j^\alpha_{(c)} || U_\mu \,. \tag{2.128}$$

This can be achieved by a conduction current of the form

$$j^\theta_{(c)} = \beta \left(\partial_r A_\phi + \ell \partial_r A_t \right) , \qquad j^r_{(c)} = -\beta \left(\partial_\theta A_\phi + \ell \partial_\theta A_t \right) , \tag{2.129}$$

where $\beta \in \mathcal{R}$ is a scaling factor. The special case of a vanishing A_t or A_ϕ deserves a little more attention. The electromagnetic field described by A^μ is then purely magnetic or purely electric, and the condition (2.129) for $j^\alpha_{(c)}$ simplifies to

$$\begin{aligned} j^\alpha_{(c)} &\parallel B^\alpha \,, && \text{for } A_t = 0 \,, \\ j^\alpha_{(c)} &\perp E^\alpha \,, && \text{for } A_\phi = 0 \,. \end{aligned}$$

Hence, in the special case of a purely magnetic or purely electric field the self-consistency of Eq. (2.126) is reached, if the conduction current follows the course of the magnetic field lines or the direction orthogonal to the electric field respectively. A projection of the pressure equation along the magnetic field lines does not differ from the uncharged case, since all the terms containing $F_{\alpha\beta}$ vanish in Eq. (2.126) [42, 90].

In contrast to this special case, the general solution requires an a priori assumption on

a conduction current depending not only on the electromagnetic potential, but also on the fluid's angular momentum. In this general case it is therefore reasonable to assume an overall vanishing conductivity instead.

To sum it up, the self-consistent pressure equations for a charged fluid in circular motion in the vicinity of a stationary and axially symmetric spacetime and electromagnetic field reads [88]

$$\frac{\partial_\mu p}{p+\varepsilon} = \partial_\mu \ln\left(U^t\right) - \frac{\ell \partial_\mu \omega}{1-\omega\ell} + \frac{\rho_q}{p+\varepsilon} F_{\mu\alpha} U^\alpha \,. \tag{2.130}$$

With the last term in Eq. (2.130) the electromagnetic forces enter the charged fluid description. According to the origin of the last term from Eq. (2.43), the electromagnetic force on the charged fluid in μ-direction is

$$\left.\begin{array}{r}\text{repulsive for } 0 < \\ \text{attractive for } 0 > \end{array}\right\} \frac{\rho_q}{p+\varepsilon} F_{\mu\alpha} U^\alpha \,. \tag{2.131}$$

2.5.2 Integrability Conditions

In order to solve the pressure equations (2.130) by a scalar function h (in which pressure and energy density can then be expressed), it is a necessary condition that h fulfills the integrability condition (e.g. [91])

$$\partial_\mu \partial_\nu h - \partial_\nu \partial_\mu h = 0 \,. \tag{2.132}$$

The demand to satisfy the integrability condition necessarily leads to further conditions to the involved quantities. These further conditions will be discussed in the following, under the assumption of a barotropic fluid, for which the pressure can be expressed as a function of the energy density only

$$p = p(\varepsilon) \,. \tag{2.133}$$

This assumption reduces the left-hand side of the pressure equations (2.130) to a partial derivative of a scalar function, $\frac{\partial_\mu p}{p+\varepsilon} = \partial_\mu F\left(p, \varepsilon(p)\right) = \partial_\mu h$, so that the integrability condition is fulfilled, if the right-hand side of the pressure equations can be reduced to a partial derivative of a scalar function as well.

Relativistic von Zeipel's Theorem

Having a look on the uncharged case, in which the third term in Eq. (2.130) vanishes, the integrability condition is fulfilled, if $\frac{\ell \partial_\mu \omega}{1-\omega\ell}$ can be expressed as a partial derivative of a

scalar function. This is the case for either a constant angular momentum or velocity ($\ell = const. \vee \omega = const.$), or if the angular velocity is a function of the angular momentum only:

$$\omega = \omega(\ell)\,. \tag{2.134}$$

This connection is called the *relativistic von Zeipel's theorem*, and it was formulated among others by Abramowicz [92].

Restrictions to the Charge Distribution

In case of a charged fluid, the third term in Eq. (2.130) does not vanish, and $\frac{\rho_q}{p+\varepsilon}F_{\mu\alpha}U^\alpha$ has to fulfill the condition of being the partial derivative of a scalar function as well. This can be transformed into a condition on the angular velocity and the charge distribution ρ_q, which is – up until now – not restricted by the Polish Donut model.

Written out explicitly, the third term of Eq. (2.130) reads:

$$\frac{\rho_q}{p+\varepsilon}F_{\mu\alpha}U^\alpha = \mathcal{K}\left(U^t\partial_\mu A_t + U^\phi\partial_\mu A_\phi\right) \tag{2.135}$$

$$= \mathcal{K}U^t\left(\partial_\mu A_t + \omega\partial_\mu A_\phi\right)\,, \tag{2.136}$$

where $\mathcal{K} = \frac{\rho_q}{p+\varepsilon}$. By setting a first condition of rigid rotation

$$\omega = const. \tag{2.137}$$

the partial derivative can be taken out of the bracket. In a second condition the charge distribution ρ_q is restricted to

$$\frac{\rho_q}{p+\varepsilon}U^t = \mathcal{K}U^t = f_\mathcal{K}(S)\,, \qquad S = A_t + \omega A_\phi \tag{2.138}$$

so that the third term can be written as

$$\frac{\rho_q}{p+\varepsilon}F_{\mu\alpha}U^\alpha = f_\mathcal{K}(S)\partial_\mu S\,, \tag{2.139}$$

which is obviously the partial derivative of a scalar function. $f_\mathcal{K}(S)$ is an arbitrary real function of S.

The value of S corresponds to the electromagnetic potential that affects a charged particle on a circular orbit with an angular velocity ω. Curves of constant $\frac{\rho_q}{p+\varepsilon}U^t$ will coincide with curves of constant S.

In the special case that either A_t or A_ϕ vanishes, the first condition for rigid rotation is not necessary for the pressure equations to satisfy the integrability condition, and the second condition reduces to $\mathcal{K}U^\alpha = f_\mathcal{K}(A_\alpha)$.

2.5.3 Solution to the Pressure Equations

Under the conditions given in section 2.5.2 above, the integration of the pressure equations (2.130) is path independent. It can be given in terms of an effective potential $h(r,\theta)$

$$h(r,\theta) = A\left(\int_0^p \frac{dp}{p+\varepsilon}\right), \tag{2.140}$$

where A is just a scaling factor. Depending on the choice of $p(\varepsilon)$, the integral in Eq. (2.140) can be solved, and pressure p, energy density ε and charge distribution ρ_q are expressed in terms of h. Equipotential surfaces of h coincide with surfaces of constant pressure and constant energy density.

With the definition of $\mathcal{P}$ in Eq. (2.123), the pressure equations (2.130) are written in terms of h as

$$\partial_\mu h = A\left(-\frac{\partial_\mu \mathcal{P}}{2\mathcal{P}} + f_\mathcal{K}(S)\partial_\mu S\right). \tag{2.141}$$

The integration of Eq. (2.141) is straight forward. One receives the following expression for the effective potential h. Finally, the pressure equations of a charged perfect fluid in circular, rigid rotation are solved:

$$h = A\left(-\frac{1}{2}\ln\mathcal{P} + \int f_\mathcal{K}(S)\,dS\right) + h_0\,. \tag{2.142}$$

h_0 is an integration constant. It can be used to set the effective potential to a certain value (eg. zero) at a certain point (r,θ).

2.5.4 Existence of Bound Solutions

According to Eq. (2.140) the pressure of a perfect fluid structure described by the Polish Donut model vanishes at $h = 0$ and marks the end of the fluid structure. As already mentioned, the integration constant h_0 can be used to shift the location of $h = 0$, and therefore the border of the fluid structure to a certain position. A bound fluid structure can then only be found, if the effective potential $h(r,\theta)$ has a local maximum, so that $h(r,\theta) = 0$ describes a closed curve in the $[r,\theta]$-area, bordering the fluid structure. The

maximum then acts as the torus center. By introducing the Hessian matrix for h

$$\mathcal{H} = \begin{pmatrix} \partial^2_{rr} h & \partial^2_{r\theta} h \\ \partial^2_{\theta r} h & \partial^2_{\theta\theta} h \end{pmatrix} , \tag{2.143}$$

the conditions for a maximum of $h(r, \theta)$ at (r_c, θ_c) can be formulated as

1. necessary conditions (extrema) $\partial_\theta h(r_c, \theta_c) = 0 \quad \text{and} \quad \partial_r h(r_c, \theta_c) = 0\,,$ (2.144)

and

2. sufficient conditions $\partial^2_{rr} h(r_c, \theta_c) < 0 \quad \text{and} \quad \det(\mathcal{H})(r_c, \theta_c) > 0\,.$ (2.145)

At extremal points (r_c, θ_c), where the first condition holds, the gradient of the pressure vanishes, and the pressure equations (2.43) reduce to the equations of geodesic motion in the uncharged case, or to the equations of motion for charged particles in an electromagnetic field.

Let us take a look at the simplest case of a Polish Donut: An uncharged perfect fluid in circular rotation in Schwarzschild spacetime with a constant angular momentum distribution (see eg. [89, 74]). The equation of the effective potential simplifies significantly to $h = -\ln|U_t|$. Closed equipotential surfaces are found for $h > 0$, indicating a local maximum in h – the center of the fluid torus. The geodesic equation for circular motion in Schwarzschild spacetime is given by

$$r_c^2 - \ell^2(r_c - 3) = 0\,, \qquad \theta_c = \pi/2 \tag{2.146}$$

[64]. Its solutions (r_c, θ_c) mark the position of the effective potential's up to two extrema. Depending on the value of ℓ, the roots might be real or complex.

A plot of the negative effective potential at the equatorial plane $-h(r, \frac{\pi}{2})$ is shown in Fig. 2.2 (a) for different values of the angular momentum ℓ. Bound solutions for a fluid torus can be found, if the course of $-h(r, \pi/2)$ contains a local minimum (corresponding to a local maximum in $h(r, \theta)$). In this case all roots of $P_{circular}(r)$ are real, and the third real root corresponds to a local maximum in $-h(r, \frac{\pi}{2})$. For the angular momentum $\ell_{(ms)}$ of the ISCO, the two outer roots of $P_{circular}(r)$ merge. $\ell_{(ms)}$ therefore builds the lower limit for ℓ, below which no bound structures for the fluid torus can be found.

The choice of h_0 determines up to which point the fluid structure reaches in the potential, or you might say, how much the potential is "filled" with fluid.

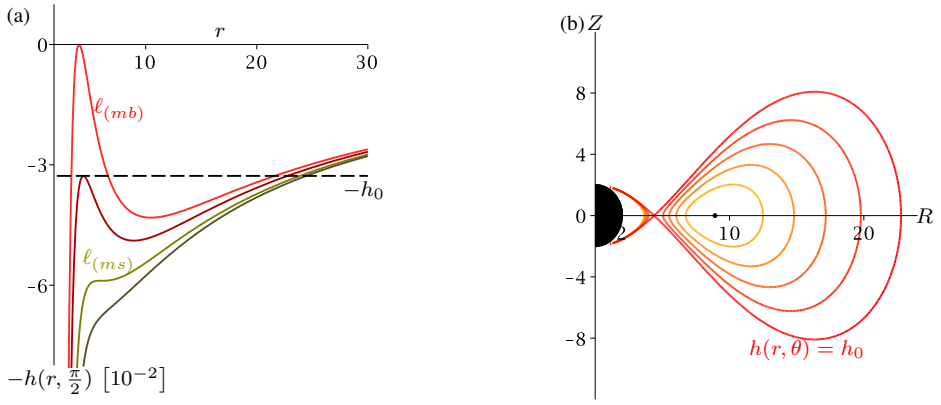

FIGURE 2.2: Effective potential $-h(r,\theta)$ for an uncharged perfect fluid in circular rotation around a Schwarzschild black hole. First (a) plotted on the equatorial plane ($\theta = \pi/2$) for different values of the angular momentum ($\ell = 4$ (bright red), $\ell = 3.85$ (dark red), $\ell = \frac{3}{2}\sqrt{6}$ (bright olive), $\ell = \frac{3}{2}\sqrt{6} - 0.1$ (dark olive)), and secondly (b) as equipotential curves in the $[R = r, Z = r\cos(\theta)]$-plane for $\ell = 3.85$. The choice of h_0 determines up to which point the fluid structure reaches in the potential. No extrema can be found for $-h(r,\theta)$ outside the horizon for $\ell < \ell_{(ms)}$, the angular momentum of the ISCO. $\ell_{(mb)}$ is the value of the angular momentum of the marginally bound circular orbit. The given choice of h_0 in (a) has the same value as the maximum of $-h(r,\pi/2)$ for $\ell = 3.85$. It creates a cusp point at the location of the maximum in the equipotential curve $h = h_0$ in (b). Closed equipotential curves with a cusp can be found for angular momenta $\ell_{(ms)} < \ell < \ell_{(mb)}$.

Existence of a Cusp Point

Next to local maxima of the effective potential, which build the center of fluid structures, its saddle points – or cusp points – are also of great interest. Saddle points are extremal points, and therefore fulfilling the conditions (2.144), its Hessian matrix however is indefinite, resulting in

$$\det(\mathcal{H})(r_c,\theta_c) < 0\,. \tag{2.147}$$

An equipotential curve of the effective potential $h(r,\theta)$, that runs through a saddle point, will show a cusp at the same location.

In the example of an uncharged perfect fluid encircling a Schwarzschild black hole, a solution with a local maximum in $h(r,\theta)$, which implies that $P_{circular}$ has two real roots, always comes along with a saddle point at the other extremum $(r_{\text{cusp}}, \frac{\pi}{2})$. In Fig. 2.2 (a) the maximum in the negative effective potential $-h\left(r, \frac{\pi}{2}\right)$ on the equatorial plane marks the saddle or cusp point. The corresponding equipotential curve $h(r,\theta) = h\left(r_{\text{cusp}}, \frac{\pi}{2}\right)$ in Fig. 2.2 (b) shows a cusp at $(r_{\text{cusp}}, \frac{\pi}{2})$. Even though the Polish Donut model itself does not allow for any radial motion, matter accretion from the thick disc onto the central object is expected to occur through the cusp point, as long as the fluid structure ends right at this point, meaning $h\left(r_{\text{cusp}}, \frac{\pi}{2}\right) = 0$. Bound fluid structures with a cusp cannot be found for all angular momenta $\ell > \ell_{ms}$ of the fluid. If ℓ is bigger than the angular

momentum of the marginally bound circular orbit ℓ_{mb}, the equipotential curve belonging to the cusp point is not closed, and the fluid structure ending at the cusp reaches infinity.

Cusp points therefore determine points through which matter accretion might take place. It is an important criterium of a cusp point if its equipotential curve is closed. To speak of a bound fluid structure as an actual accretion disc, from which matter can be accreted, the fluid structure should contain a cusp point, through which the matter is channeled before falling onto the central object. For a more detailed description of the uncharged fluid torus in Schwarzschild spacetime see eg. [74, 89].

Chapter 3

Plasma Accretion by a Charged, Rotating Black Hole

The goal of this chapter is to investigate how and to which extent an electric net charge of a spinning black hole influences the relativistic accretion process – especially with respect to plasma accretion.

Considered are black hole charges, which can be called realistic according to the discussion in Sec. 2.2.1.1. The accreted plasmas are supposed to be very dilute with densities that typically occur in interstellar or interplanetary plasmas.

A good way to gain a basic understanding of a physical process is to approach the questioning by using an analytical model. The heavy simplification of a complex physical process, necessary to receive an analytical description, allows to focus on the pure effects of the aspect of interest. Furthermore the analytical model might serve as a test-bed for numerical simulations of the problem.

The problem will be tackled by using a generalization of the model introduced by Mendoza, Tejeda, and Nagel [93], Tejeda, Mendoza, and Miller [22] and Tejeda, Taylor, and Miller [82]. In these publications it was used for a Newtonian approach, and for Schwarzschild and Kerr spacetime, respectively. It was shown that the used model is well suited to explore relativistic effects, such as frame dragging, on the accretion process, and may further be used in numerical simulations for collapsar-like setups to reduce computational costs.

As a general relativistic description of the charged, spinning black hole, Kerr-Newman spacetime (Sec. 2.2.1) is employed. Analogous to the description of the accreted matter as dust in [93, 22, 82], the accreted plasma is described in the test-particle approach, introduced in Sec. 2.3. This description of plasma is justified for sufficiently dilute

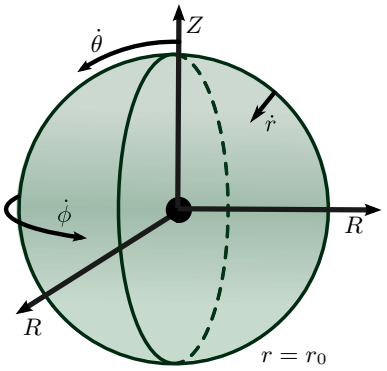

FIGURE 3.1: Sketch of the dust accretion model. In Boyer-Lindquist coordinates: $R = \sqrt{r^2 + a^2}\sin(\theta)$, $Z = r\cos(\theta)$.

plasmas, for which any type of particle interactions – let it be collisions of electromagnetic effects – may be neglected.

3.1 The Accretion Model

Next to the assumption of sufficient diluteness, further simplifying assumptions are needed to allow for a description of the accretion process in terms of an analytical model. The model is a generalization of the model used in [22, 82] to a charged spinning black hole and charged matter. The resulting model and the included simplifying assumptions are introduced in the following.

The model can basically be divided into three parts: (i) an electrically charged and rotating black hole, solely determining the gravitational and electromagnetic field, (ii) a featureless accretion disc, that lies in the equatorial plane of the black hole, and (iii) a rotating shell of charged particles surrounding the black hole at a certain radius r_0, and the continuous source of the accreted matter. A sketch of the model is depicted in Fig. 3.1. The following provides a detailed descriptions of the three model parts.

The charged, rotating black hole The electrically and rotating central black hole is described by the Kerr-Newman spacetime with the magnetic monopole set to zero ($P = 0$). According to the discussion in Sec. 2.2.1 the spacetime possesses an axial symmetry along the rotation axis ($\theta = 0$), and a reflection symmetry with respect to equatorial ($\theta = \pi/2$) plane. In case of no magnetic monopole, the corresponding equations of motion (2.60) -(2.63) for a charged test-particle reproduce both symmetries. Both net charge and mass of the central black hole are considered constant. The accretion rate therefore has to be appropriately small.

As discussed in the previous section 2.2.1.1, realistic estimations point to small, but not vanishing black hole net charges. This is also in general the assumption in this model. For a certain order of magnitude ($eQ \sim 1$) both electromagnetic and gravitational interactions play a noticeable role in the motion of a charged particle. For much smaller net charges, the electromagnetic influence on the accretion process is negligible, and the Kerr-limit is reached, which was already discussed by Tejeda et al. [82]. For much bigger net charges electromagnetic effects dominate the particle motion and it does not deviate much from a radial infall (see Sec. 2.4.2).

The featureless accretion disc A featureless accretion disc is assumed to be located in the equatorial plane, which is motivated by the reflection symmetry of spacetime and equations of motion. If the symmetry is broken, either by the equations of motion or the mean initial conditions of the accreted matter building the disc, the location of the disc deviates from the equatorial plane. This is the case e.g for warped and twisted accretion discs [94, 95, 96], where the mean angular momentum of the accreted matter is not oriented along the rotation of the black hole, or for accretion discs in NUT spacetime [35], which exhibits no reflection symmetry with respect to $\theta = \pi/2$. The consideration of a magnetic monopole would break the mirror symmetry of the equations of motion for electrically charged particles, making the accretion disc position unclear. The accretion disc is assumed to have no influence on the spacetime or on the overall electromagnetic field, which will be solely created by the central black hole. The disc therefore is, like the black hole, treated as a passive sink for accreted matter and energy.

The built model can deduce features of the initially featureless accretion disc.

The charged particle cloud A charged particle cloud takes the role of plasma in this model. The charged particles of the cloud are continuously injected at r_0 with initial velocities $(\dot{r}_0, \dot{\theta}_0, \dot{\phi}_0)$, which do not vary on the r_0-shell. From every point of the r_0-shell a collection of ions and electrons is injected, which has an overall vanishing charge, so that a quasi-neutral plasma is ensured on the shell. The particles start falling onto the black hole, until they either hit the accretion disc at the equatorial plane, or reach the event horizon. The formed plasma is assumed to be sufficiently dilute, so that any particle collisions are negligible. Furthermore electromagnetic fields or gravitational effects created by the plasma have to be small enough to be negligible compared to the electromagnetic field and gravitational influence of the central black hole. This assumptions support the concept of the central black hole and accretion disc as passives sinks for particles and energy. The charged particles, that build the collisionless, cold plasma, can then be described in the test-particle approach, in which the trajectory of each

individual particle in the cloud is given by the equations of motions (2.60) -(2.63) in Kerr-Newman spacetime. These trajectories build streamlines for the particles, starting at different angles on the shell and reaching either the equatorial plane or the event horizon of the black hole.

The initial conditions $(\dot{r}_0, \dot{\theta}_0, \dot{\phi}_0)$ are chosen such that the spacetime symmetry is reproduced. A jump of the initial value of the four-velocity in θ-direction at the equatorial plane can be avoided by setting $\dot{\theta}_0$ to zero, since a reproduction of the mirror symmetry at the equatorial plane demands $\dot{\theta}_0 = -\dot{\theta}\big|_{\pi-\theta_0}$. Particles from the upper hemisphere will collide with their counterpart particle from the lower hemisphere precisely at the equatorial plane due to the mirror symmetry. Setting the three initial conditions $(\dot{r}_0, \dot{\theta}_0, \dot{\phi}_0)$ for every plasma particle in the dust cloud is equivalent to completely determine the three constants of motion E, l and C for the course of every particle. They are determined by Eqs. (2.54) and (2.60).

Streamline intersections of the same particle type result in a divergence of the particle density at the point of intersection. This becomes vivid by inspecting Eq. (3.20), which will be discussed in more detail in Sec. 3.4. At the intersection points a sufficient diluteness of the plasma does not hold anymore. It is therefore necessary to demand, that streamline intersections do not occur, which leads to the restriction

$$\left(\frac{\partial\theta}{\partial\theta_0}\right) \geq 0\,, \tag{3.1}$$

and in the end restricts the range of initial conditions $(\dot{r}_0, \dot{\theta}_0, \dot{\phi}_0)$ that are consistent with the model.

The constant initial conditions of the plasma particles at r_0 result in a constant accretion rate

$$\dot{M} = -\int\int n_0 \rho^2(r_0)\dot{r}_0 \sin(\theta_0) d\theta_0 d\phi_0 \tag{3.2}$$

for a particles density n_0 at r_0. Together with the treatment of the central black hole and accretion disc as passive sinks for particles and energy a stationary accretion model is built.

Four aspects of the accretion process in the described model are examined in regards to their dependence on spacetime parameters (eQ, a) and initial conditions $(\dot{r}_0, \dot{\theta}_0, \dot{\phi}_0, r_0)$: a) The velocity field of the plasma, b) the shape of the streamlines, c) the resulting density field and d) the location of the inner and outer edge of the initially featureless assumed accretion disc. The axial symmetry of the introduced accretion model makes it sufficient to discuss all aspects projected onto the (r, θ) plane. Due to the additional reflection symmetry to the equatorial plane, and the accretion disc hindering all particles

from passing it, the discussion can be further restricted to $\theta < \frac{\pi}{2}$. All aspects will be treated separately for the different particle types of the plasma cloud.

3.2 The Velocity Field

The velocity field is calculated in a set of reference frames, which describe Kerr-Newman spacetime locally as Minkowskian. The Kerr-Newman metric of the form (2.13), is then locally expressed in a set of Minkowskian coordinates $x^{\hat{\alpha}}$:

$$\begin{aligned} ds^2 &= \left(g_{tt} - \omega_Z^2 g_{\phi\phi}\right) dt^2 + g_{rr}\, dr^2 + g_{\theta\theta}\, d\theta^2 + g_{\phi\phi}\left(d\phi - \omega_Z\, dt\right)^2 , \\ &= -d\hat{t}^2 + d\hat{r}^2 + d\hat{\theta}^2 + d\hat{\phi}^2 . \end{aligned}$$

An expression of the plasma cloud's velocity field in $x^{\hat{\alpha}}$ corresponds to measurements by locally non-rotating observers, better known as zero angular momentum observers (ZAMOs). The worldlines of these observers are constant in the radial and θ-component, but they have a changing ϕ-component:

$$\phi = const. + \omega_Z t\,, \qquad \text{with} \qquad \omega_Z = -\frac{g_{\phi t}}{g_{\phi\phi}}\,,$$

which is why they encircle the black hole from a resting observer at infinity's point of view. ZAMOs are so to say "frame-dragged". The reference frames were introduced by Bardeen et al. [87] as locally nonrotating reference frames (LNRFs)[1].

The four-velocity components $u^{\hat{\alpha}}$ in LNRFs of the plasma particle cloud at point (r, θ) can be calculated from the four-velocity components $(u^t, u^r, u^\theta, u^\phi)$ in Boyer-Lindquist coordinates by

$$\begin{aligned} u^{\hat{r}} &= \sqrt{\frac{\rho^2}{\Delta}}u^r\,, \qquad & u^{\hat{\phi}} &= \sqrt{\frac{\Sigma}{\rho^2}}\sin(\theta)\left(u^\phi + \frac{(r^2-a^2)-\Delta}{\Sigma}u^t\right), \\ u^{\hat{\theta}} &= \sqrt{\rho^2}u^\theta\,, & u^{\hat{t}} &= \sqrt{\frac{\rho^2\Delta}{\Sigma}}u^t\,, \end{aligned} \tag{3.3}$$

where u^t, u^r, u^θ and u^ϕ are known from the four equations of motion (2.60) -(2.63) in Kerr-Newman spacetime:

$$\begin{aligned} u^r &= \frac{\sqrt{\mathbf{R}}}{\rho^2}\,, & u^\phi &= \frac{a\mathcal{R}(r)}{\rho^2\Delta} - \frac{\mathcal{T}(\theta)}{\rho^2\sin^2(\theta)}\,, \\ u^\theta &= \frac{\sqrt{\Theta}(\theta)}{\rho^2}\,, & u^t &= \frac{(r^2+a^2)\,\mathcal{R}(r)}{\rho^2\Delta} - \frac{a\mathcal{T}(\theta)}{\rho^2}\,. \end{aligned} \tag{3.4}$$

[1] Detailed information on LNRFs can be found in the very same article or otherwise in [6].

In flat spacetime, the three-velocity v^a, $a = 1..3$ of a particle measured by an observer at rest can by calculated by

$$v^a = \frac{dx^a}{dx^0} = \frac{u^a}{u^0}\,. \tag{3.5}$$

According to Eq. (3.5) the plasma cloud's velocity field measured at (r, θ) by the corresponding ZAMO is

$$v^{\hat{r}} = \frac{d\hat{r}}{d\hat{t}} = \frac{\sqrt{\mathbf{R}/\Delta}}{\rho\gamma}\,, \tag{3.6}$$

$$v^{\hat{\theta}} = \frac{d\hat{\theta}}{d\hat{t}} = \frac{\sqrt{\Theta}}{\rho\gamma}\,, \tag{3.7}$$

$$v^{\hat{\phi}} = \frac{d\hat{\phi}}{d\hat{t}} = \frac{\rho(l - eQra/\rho^2\,\sin^2(\theta))}{\gamma\Sigma}\,, \tag{3.8}$$

where the magnetic monopole is set to zero ($P = 0$). In the given equations above γ is the Lorentz factor between the LNRF and the passing plasma particles. It is given by

$$\gamma = u^{\hat{t}} = \sqrt{1 + v^{\hat{r}2}\gamma^2 + v^{\hat{\theta}2}\gamma^2 + v^{\hat{\phi}2}\gamma^2}\,. \tag{3.9}$$

The absolute value $|\boldsymbol{v}|$ of the three-velocity in a LNRF cannot exceed the speed of light (in dimensionless units 1) for a timelike motion:

$$|\boldsymbol{v}| = \sqrt{v^{\hat{r}2} + v^{\hat{\theta}2} + v^{\hat{\phi}2}} < 1\,, \tag{3.10}$$

which can be derived from the normalization condition (2.55).

Velocity components (3.6)-(3.8) depend on coordinates (r, θ) and on the initial conditions $\dot{r}_0, \dot{\theta}_0, \dot{\phi}_0, \theta_0$ and r_0, which determine the values of the constants of motion E, l and C. As a consequence the streamlines of the plasma cloud have to be calculated first, to gain an expression for (r, θ) in terms of the initial conditions.

3.3 Streamlines

Streamlines describe the course of one plasma particle type from its starting point (r_0, θ_0) on the rotating shell to the equatorial plane or event horizon. They are expressed by a function $r(\theta)$. The streamline function $r(\theta)$ can be derived from the solutions of the equations of motion (2.60) -(2.63), which were derived in Sec. 2.4.3.

The solution for the r-motion $r(\lambda)$ was derived in (2.95). The integration constant c_{sn} fixes the initial condition $r(\lambda_0) = r_0$. According to Eq. (2.90) and substitution (2.93) it

is given for $\lambda_0 = 0$ by

$$c_{sn} = -\int_0^{y_0} \frac{dz}{(1-z^2)(1-k_r^2 z^2)} = -F\left(y_0 = \sqrt{\frac{(r_4-r_2)(r_0-r_1)}{(r_1-r_2)(r_0-r_4)}}, k_r\right) , \tag{3.11}$$

$$=: -\frac{1}{2}\sqrt{(1-E^2)(r_1-r_3)(r_2-r_4)}\Phi(r_0) . \tag{3.12}$$

To receive an expression $r(\theta)$, Mino time λ in $r(\lambda)$ needs to be expressed in terms of angle θ. The solution for the θ-motion $\theta(\lambda)$ is given in (2.112), where c_{cn} fixes initial condition $\theta(\lambda_0) = \theta_0$:

$$c_{cn} = -F\left(x_0 = \frac{\cos(\theta_0)}{\cos(\theta_a)}, \tilde{k}_\theta\right) . \tag{3.13}$$

Solving $\theta(\lambda)$ for λ leads to

$$\lambda = \Psi(\theta) - \Psi(\theta_0) , \qquad \text{with} \qquad \Psi(\theta) = \frac{\cos(\theta_a)\,\mathrm{cn}^{-1}\left(\frac{\cos(\theta)}{\cos(\theta_a)}, \tilde{k}_\theta\right)}{\sqrt{C + a^2(E^2-1)\cos^4(\theta_a)}} . \tag{3.14}$$

Putting everything together, the streamlines are given in terms of $r(\theta)$ by (2.95), with

$$\xi = \frac{1}{2}\sqrt{(1-E^2)(r_1-r_3)(r_2-r_4)}\,(\Phi(r_0) + \Psi(\theta_0) - \Psi(\theta)) . \tag{3.15}$$

Constants of motions C, E and l appear in the streamline description $r(\theta)$ and in Eqs. (2.60) and (2.61). They determine the roots $r_{1..4}$ and θ_a, and are calculated using Eqs. (2.54) and (2.57) for the initial conditions r_0, θ_0 and $(\dot{r}_0, \dot{\theta}_0, \dot{\phi}_0)$. The equations in (2.54) contain $\dot{t}$, which is derived from the normalization condition (2.55). As a consequence, the constants of motion are different for every streamline, since the streamlines start at different angles θ_0 on the rotating shell at r_0.

During calculation of streamlines for various different initial conditions, it turns out that turning points in either $r(\lambda)$ or $\theta(\lambda)$ for $\theta \in [\theta_0, \pi/2]$ are mainly causing the intersection of streamlines. Streamline intersections, as mentioned before have to be avoided, since they give rise to a divergence of the plasma particle density at that point. A set of initial conditions can be checked rather easily if it results in turning points for the r- or θ-motion in the named range, by checking if $\tau(\theta) > \tau(r)$ for $\theta_0 = \pi/2 - \delta\theta_0$ close to the equatorial plane. The set of initial conditions is discarded in case the occasion arises. Small values for the specific angular momentum l and charge product eQ seem preferable to avoid turning points.

The position and number of real roots of $\mathbf{R}(r)$ and $\Theta(\theta)$ changes for different streamlines and initial conditions. If all roots of $\mathbf{R}(r)$ are real, they are assigned to $r_{1..4}$ as described in Sec. 2.4.3.1, so that the calculation of $r(\lambda)$ stays in the real domain. In case that two complex roots of $\mathbf{R}(r)$ occur, the real roots are assigned to r_1, r_4, with $|r_1| < |r_4|$,

and the complex pair to r_2, r_3. In case of four complex roots one complex conjugate pair is assigned to r_1, r_4 and the other one to r_2, r_3. This approach does not avoid a calculation in the complex domain for $r(\lambda)$. To keep the calculation in the real domain, when complex roots of $\mathbf{R}(r)$ occur, one has to use the respective expression (2.98) or (2.98) for $r(\lambda)$.

If $\Theta(\theta)$ has real roots, $\theta_a \in [0, \pi/2]$ is chosen to be the root closest to the equatorial plane. The streamline will then lie in the range $\theta \in [\theta_a, \pi/2]$, since turning points in $\theta(\lambda)$ are not permitted in the streamline description. According to the discussion in Sec. 2.4.3.2 $\lambda(\theta)$ can be expressed solely in real quantities for all three cases. It is worth mentioning here, that case 3 will not occur in the streamline description, as $C < 0$ describes a particle motion which cannot reach the equatorial plane (see discussion in Sec. 2.4.1). By setting the initial condition $\dot{\theta}_0 = 0$, θ_0 and θ_a coincide.

The streamline description could be expressed in the same equations which were introduced by Tejeda et al. [82] for uncharged dust accreted by a Kerr black hole. Only the position of the roots $r_{1..4}$, θ_0 and the values of E, C and l is influenced by the black hole net charge acting on the plasma.

3.4 The Density Field

The density field is determined by satisfying the continuity equation

$$(nu^\mu)_{;\mu} = 0\,, \tag{3.16}$$

introduced before in Eq. (2.42) in Sec. 2.3 for the fluid approach of plasma. Equation (2.42) can be turned into Eq. (3.16) by expressing the rest-mass density ρ_m as $\rho_m(r,\theta) = \mu_x n(r,\theta)$, where $n(r,\theta)$ denotes the particle density of particles with mass μ_x.

With the help of Gauss' theorem

$$\int_{\mathcal{V}} V^\mu{}_{;\mu}\sqrt{g}\, d^4x = \int_{\partial\mathcal{V}} V^\mu N_\mu \sqrt{|h|}\, d^3x\,, \qquad g = \det(g_{\mu\nu})\,, \tag{3.17}$$

the continuity equation can be written as an integration over the particle flux through a three dimensional hypersurface $\partial\mathcal{V}$ delimiting the integration volume $\mathcal{V}$:

$$\int_{\partial\mathcal{V}} nu^\mu N_\mu \sqrt{|h|} d^3x = 0\,. \tag{3.18}$$

N_μ is a unit vector normal to $\partial\mathcal{V}$, and h is the determinant of the induced metric on the hypersurface. To solve Eq. (3.18) for n, a wise choice for integration volume $\mathcal{V}$ is helpful.

It is chosen such that the spatial protection of $\partial\mathcal{V}$ is described by neighboring streamlines reaching from r_0 to r. The particle flux will only be non-zero through the two segments of $\partial\mathcal{V}$ at r and r_0, that are oriented perpendicular to the radial direction and connected by the neighboring streamlines. With $N_\mu = \pm\delta^r_\mu/\sqrt{g^{rr}}$ and $|h|/g^{rr} = \rho^4\sin^2(\theta)$ at the two hypersurface segments, Eq. (3.18) reduces to

$$nu^r\rho^2\sin(\theta)\,d\theta\,d\phi\,dt - n_0u^r_0\rho^2_0\sin(\theta_0)\,d\theta_0\,d\phi_0\,dt_0 = 0\,, \tag{3.19}$$

where the zero indicates an evaluation of the quantity at $r = r_0$ and $\theta = \theta_0$. Stationarity and axial symmetry of the described accretion process demands that $d\phi_0 dt_0 = d\phi dt$ for the chosen hypersurface. One can now derive the final equation for the particle density field [82]:

$$n = \frac{n_0u^r_0\rho^2_0\sin(\theta_0)}{u^r\rho^2\sin(\theta)}\left(\frac{\partial\theta}{\partial\theta_0}\right)^{-1}\,. \tag{3.20}$$

An intersection of streamlines leads to $\left(\frac{\partial\theta}{\partial\theta_0}\right) = 0$ at the point of intersection, resulting in a diverging particle density n at that point (see Eq. (3.20)). The negligence of particle interactions is not a good approximation in this case. Streamline intersections have to be avoided for this reason, which results in the initial condition given in Eq. (3.1).

The whole plasma density field is simply derived, by deriving the density field n_i of each plasma particle type separately using Eq. (3.20) and calculate their sum

$$n_{(plasma)} = \sum_i n_i\,(r,\theta)\,. \tag{3.21}$$

3.5 Features of the Accretion Disc

Plasma particles from the spherical shell which do not fall directly onto the event horizon feed an initially featureless accretion disc, located at the equatorial plane. Particle interactions, resulting for example in pressure and viscosity, are not negligible in the disc, so that plasma particles will be trapped in the accretion disc once they reach the equatorial plane. Due to this process, the accretion disc builds up until a stationary situation is reached.

The following definitions for the inner and outer edge however are derived from the used collisionless accretion model. Even though a rough approximation, due to its negligence of the influence of any kind of particle interaction on the edge's position, it can still give a hint on where to expect the inner and outer edge of the accretion disc.

The Outer Edge Bearing in mind that streamlines do not intersect, the furthest away from the central black hole a streamline can reach the equatorial plane is given by

$$r_{\mathrm{D}} := \lim_{\theta_0 \to \frac{\pi}{2}} r\left(\theta = \pi/2\right) . \tag{3.22}$$

The outer edge of the final accretion disc is determined by r_{D}. The expression for r_{D} is given by (2.95), with E, C, l and the roots of $\mathbf{R}(r)$ calculated in the limit $\theta_0 \to \pi/2$. Variable ξ, which was specified in Eq. (3.15) simplifies to [82]

$$\xi_{\mathrm{D}} = \frac{1}{2}\sqrt{\left(1-E^2\right)\left(r_1 - r_3\right)\left(r_2 - r_4\right)}\left(\Phi\left(r_0\right) - \frac{\pi}{2\sqrt{l^2 - \left(E^2-1\right)a^2}}\right) . \tag{3.23}$$

It is derived by first calculating term $\Psi(\theta)$ in Eq. (3.15) for $\theta = \pi/2$

$$\Psi(\pi/2) = \frac{\cos(\theta_a)\, K(\tilde{k}_\theta)}{\sqrt{C + (E^2-1)a^2\cos^4(\theta_a)}} \tag{3.24}$$

and then taking the limit $\lim_{\theta_0 \to \frac{\pi}{2}} \Psi(\pi/2)$. Since $\lim_{\theta_0 \to \frac{\pi}{2}} \theta_a = \pi/2 = \theta_0$, term $\Psi(\theta_0)$ becomes $\Psi(\theta_a) = 0$.

The Inner Edge The inner edge will be defined by the ISCO for charged particles in Kerr-Newman spacetime. Without further forces acting on the plasma particles besides the one arising from the interaction with the black hole's electromagnetic field, the plasma particles cannot stay on circular orbits around the central black hole for radii smaller than their corresponding ISCO. Particles, that reach the equatorial plane at radii smaller then their ISCO are bound to fall into the black hole and do not contribute to the main accretion disc. However, these plasma particles could form a so-called minidisc [97, 98], while spiraling into the black hole.

The ISCO for charged particles in Kerr-Newman spacetime is discussed in Sec. 2.4.4. For each particle type in the plasma cloud the corresponding ISCO will be located at a different radius, depending on the value for eQ (see Fig. 2.1). The ISCO of plasma particles with $eQ > 0$, deviate much more from the corresponding ISCO of uncharged particles, than the ISCO of plasma particles with the same $|eQ|$, but $eQ < 0$.

3.6 Hydrogen Plasma and Uncharged Dust Accretion

The discussion of the accretion process of hydrogen plasma and uncharged dust accretion within the introduced model helps to gain a basic understanding of how an electric net charge of a spinning black hole might effect accretion processes. Available tools are

the discussion of streamlines, the velocity field in LNRFs, the density field built by the accreted matter as well as the position of the inner and outer edge of the fed accretion disc.

The discussions are undertaken by an evaluation for different initial conditions $(\dot{r}_0, \dot{\phi}_0)$ at r_0 and the spacetime parameters (a, Q) (for uncharged dust) or (a, eQ) (for hydrogen plasma). For a better comparison with the results in Tejeda et al. [82], the initial conditions are given in terms of the radial and angular velocities in LNRFs $\left(v_e^{\hat{r}_0}, v_e^{\hat{\phi}_0}\right)$ measured at $(r_0, \theta = \pi/2)$. They can be calculated from $(\dot{r}_0, \dot{\phi}_0)$ using Eqs. (3.6) and (3.8). The choice of $v_e^{\hat{r}_0}$, $v_e^{\hat{\phi}_0}$ and spacetime parameters a and Q is restricted to

$$\left(-v_e^{\hat{r}_0}, v_e^{\hat{\phi}_0}\right) \in [0, 1) \qquad \text{and} \qquad (a^2 + Q^2) \in [0, 1] \,. \tag{3.25}$$

The restrictions on $v_e^{\hat{r}_0}$ and $v_e^{\hat{\phi}_0}$ are necessary to assure a time-like motion of the accreted matter, the restrictions on a and Q prohibit naked singularities. By restricting $v_e^{\hat{\phi}_0}$ to positive values, a counter-rotating dust or plasma cloud corresponds to a negative spin parameter a.

The initial angular motion in θ is set to zero for all discussed scenarios:

$$\dot{\theta}_0 = 0 \,. \tag{3.26}$$

As a consequence starting point θ_0 coincides with root θ_a of $\Theta(\theta)$, which occurs in Eq. (3.14) of the streamline description.

The density field is derived by numerically calculating differential $\left(\frac{\partial\theta}{\partial\theta_0}\right)$ from Eq. (3.20). It is possible to find an analytical expression for the differential. However, θ_0 enters the inverse function of the streamline description $\theta(r)$ among others through the roots $r_{1..4}$ of $\mathbf{R}(r)$. This complicates a possible analytic expression of $\left(\frac{\partial\theta}{\partial\theta_0}\right)$ enormously, so that a numerical approach is preferred here.

3.6.1 Accretion of Uncharged Dust

The special case of the accretion of uncharged dust by a strongly charged central black hole is presented in terms of streamlines, local velocity field and density field in Fig. 3.2 (b).

As discussed in Sec. 2.2.1.1 strongly charged black holes with $Q \sim 1$ are rather unlikely to exist. Furthermore it is unlikely, that initially neutral accreted matter remains neutral in the vicinity of such an extremely strong electromagnetic field. Nevertheless this case

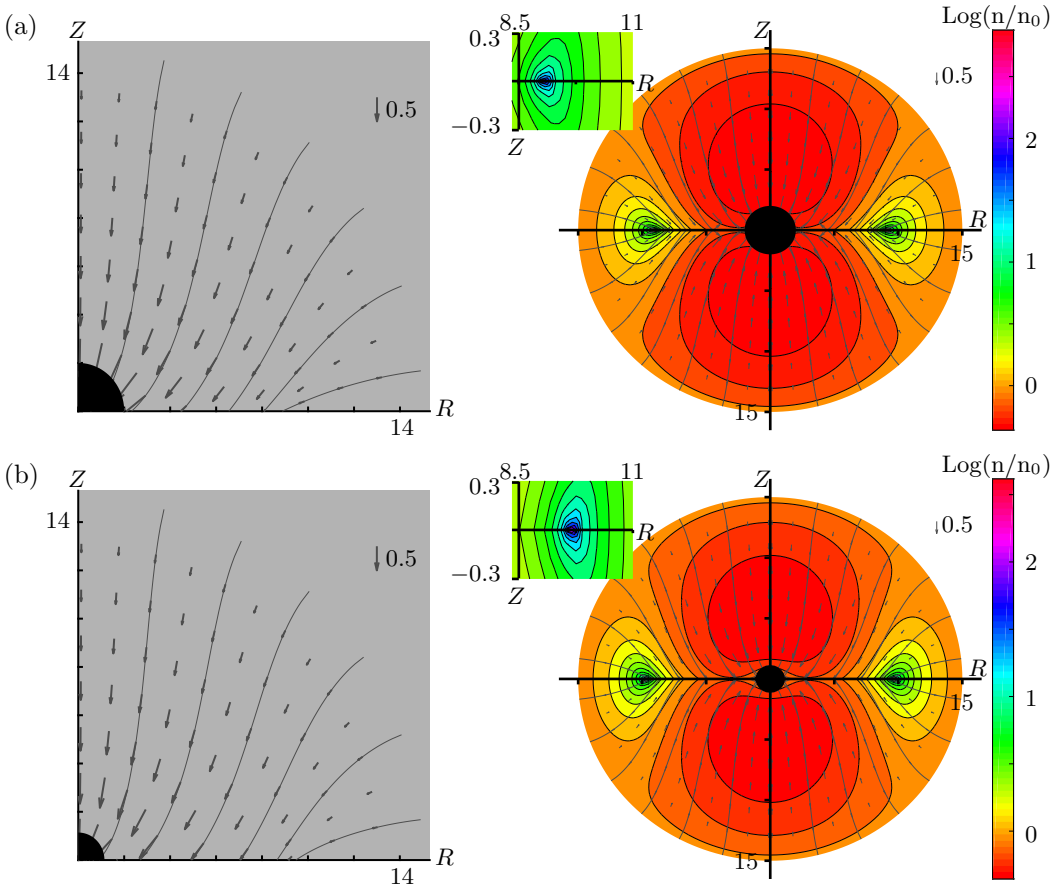

FIGURE 3.2: Streamlines, local velocity field (left and right) and density field (right) presented for uncharged dust (a) in the Schwarzschild limit ($a = Q = 0$) and (b) for a negatively charged black hole with $a = 0, Q = 0.99$. The initial conditions are in both examples set to $r_0 = 15$, $v_e^{\hat{\phi}_0} = 0.25$ and $v_e^{\hat{r}_0} = -0.1$. Particle density normalized to the initial particle density n/n_0 is depicted in a logarithmic scale as a color plot. The black hole net charge has only a small influence on the accretion flow. The density peak occurring in both examples moved to a bigger radius for the charged black hole.

will be shortly discussed here. It focuses on the pure effect of the additional spacetime curvature caused by the electrical net charge on the accretion process.

In case of uncharged dust ($e = 0$), the net charge Q only contributes to the equations of motion by its appearance in the metric coefficients trough $\Delta(r)$ (see Eqs. (2.14), (2.54)). Its effect on the accretion flow will therefore be relevant only for small values of r, where the value of $\Delta(r)$ significantly deviates from the one for $Q = 0$.

To support this statement, the accretion of uncharged dust by a strongly charged black hole ($Q = 0.99$) is compared to the accretion by an uncharged black hole with otherwise same initial conditions and spin parameter (see Fig. 3.2). Only slight differences can be recognized between the accretion pictures of the uncharged and the charged black hole case. Density peaks occur at the location of the outer edge of the fed accretion disc. The peaks position moves to a slightly bigger radius for the charged black hole.

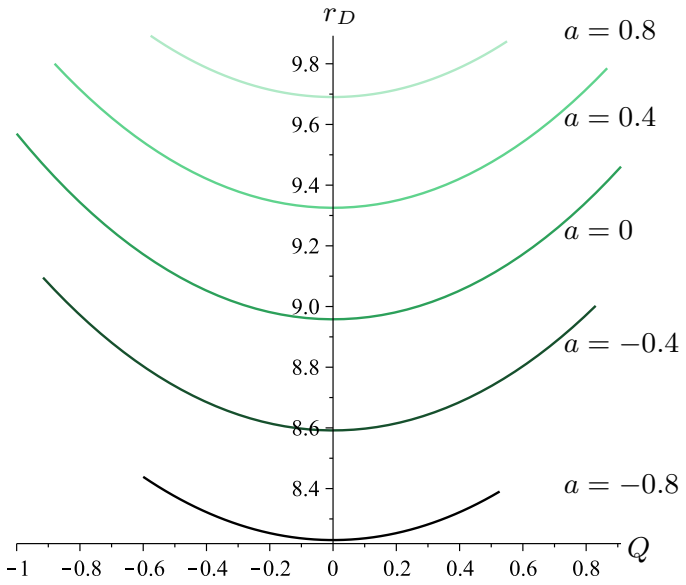

FIGURE 3.3: Outer edge r_{D} of the forming accretion disc for uncharged dust ($e = 0$) as a function of net charge Q for $r_0 = 15$, $v_e^{\hat{\phi}_0} = 0.25$, $v_e^{\hat{r}_0} = -0.1$ and different values of a. The dust flow is counter-rotating for $a < 0$ and co-rotating for $a > 0$. r_{D} changes only slightly for a variation of a and even less for a variation of Q compared to the changes induced by a variation of the initial velocities $v_e^{\hat{\phi}_0}$ and $v_e^{\hat{r}_0}$, plotted in Fig. 3.9. The shift of r_{D} to bigger values for higher spins a depicts the frame-dragging effect, which was discussed in Tejeda et al. [82].

The rather small influence of a black hole net charge on the accretion of uncharged dust is also seen in its small effect on the location of the outer edge, which is depicted in Fig. 3.3. The position of r_{D} changes only slightly with a variation of net charge Q in the order of a few percent. The changes in r_{D} are even less then the changes caused by a variation of spin parameter a, which is also presented in Fig. 3.3. A variation of the initial conditions causes notably bigger changes in the location of the outer edge. This becomes apparent in Fig. 3.8 (a) and (b) at $eQ = 0$.

All in all, the effect of an additional spacetime curvature due to the black hole net charge is not relevant for accretion processes even in case of extremal net charges $Q = 1$.

3.6.2 Accretion of Hydrogen Plasma

The hydrogen plasma is assumed to be composed of protons and electrons. Unionized hydrogen is neglected in this description. Electrons and protons are ejected from the rotating shell at r_0 with a constant particle density $n_{0,\mathrm{e}} = n_{0,\mathrm{p}} = n_0$ [2], so that a quasi-neutral plasma exists on the shell.

[2]The particle mass, specific charge and particle density field of electrons and protons is referred to by index e or p, respectively.

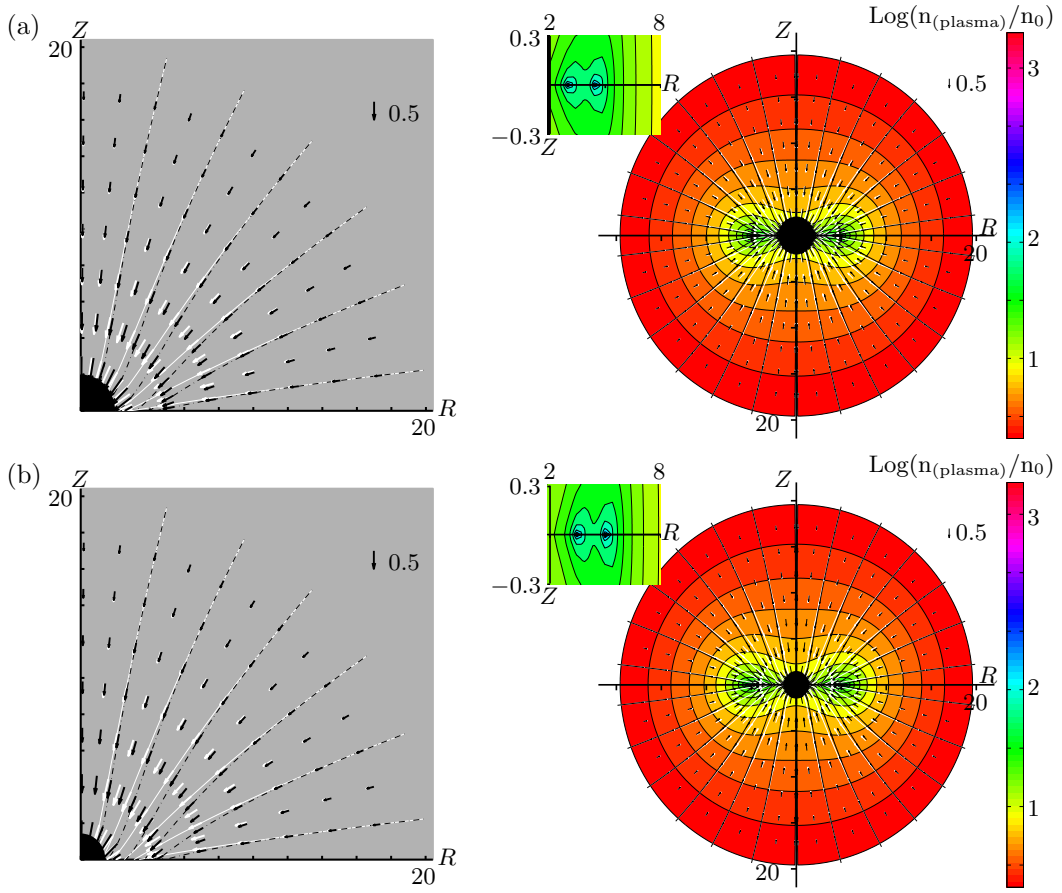

FIGURE 3.4: Streamlines, local velocity field (left and right) and density field (right) presented for the accretion of hydrogen plasma by a negatively charged black hole with $e_{\mathrm{e}}Q = 0.5$ and two different spin parameters $a = 0.1$ (a) and $a = 0.9$ (b). The initial conditions in both examples are set to $r_0 = 20$, $v_e^{\hat{\phi}_0} = 0.11$ and $v_e^{\hat{r}_0} = -0.2$. The plasma density, normalized to the initial particle density of electrons and protons $n_{(plasma)}/n_0$, is depicted in a logarithmic scale. The black hole spin has only a small influence on the accretion flow. The density peaks move to bigger radii for faster spinning black holes.

As mentioned in the introduction of the used accretion model (Sec. 3.1) the considered black hole net charge Q has to result in $eQ \sim 1$. Only then electromagnetic and gravitational effects play a role in the described accretion process. The specific charge e of an electron or proton is given in geometrized units by

$$e_{\mathrm{e,p}} = \frac{1}{\sqrt{4\pi\varepsilon_0 G}} \left(\frac{\epsilon}{\mu}\right)_{\mathrm{e,p}} , \tag{3.27}$$

which results in

$$e_{\mathrm{e}} \approx -2.042 \cdot 10^{21} \qquad \text{and} \qquad e_{\mathrm{p}} \approx 1.112 \cdot 10^{18} . \tag{3.28}$$

The restriction to $eQ \sim 1$ leads to considered net charges of the order

$$Q \sim 10^{-18} - 10^{-21} . \tag{3.29}$$

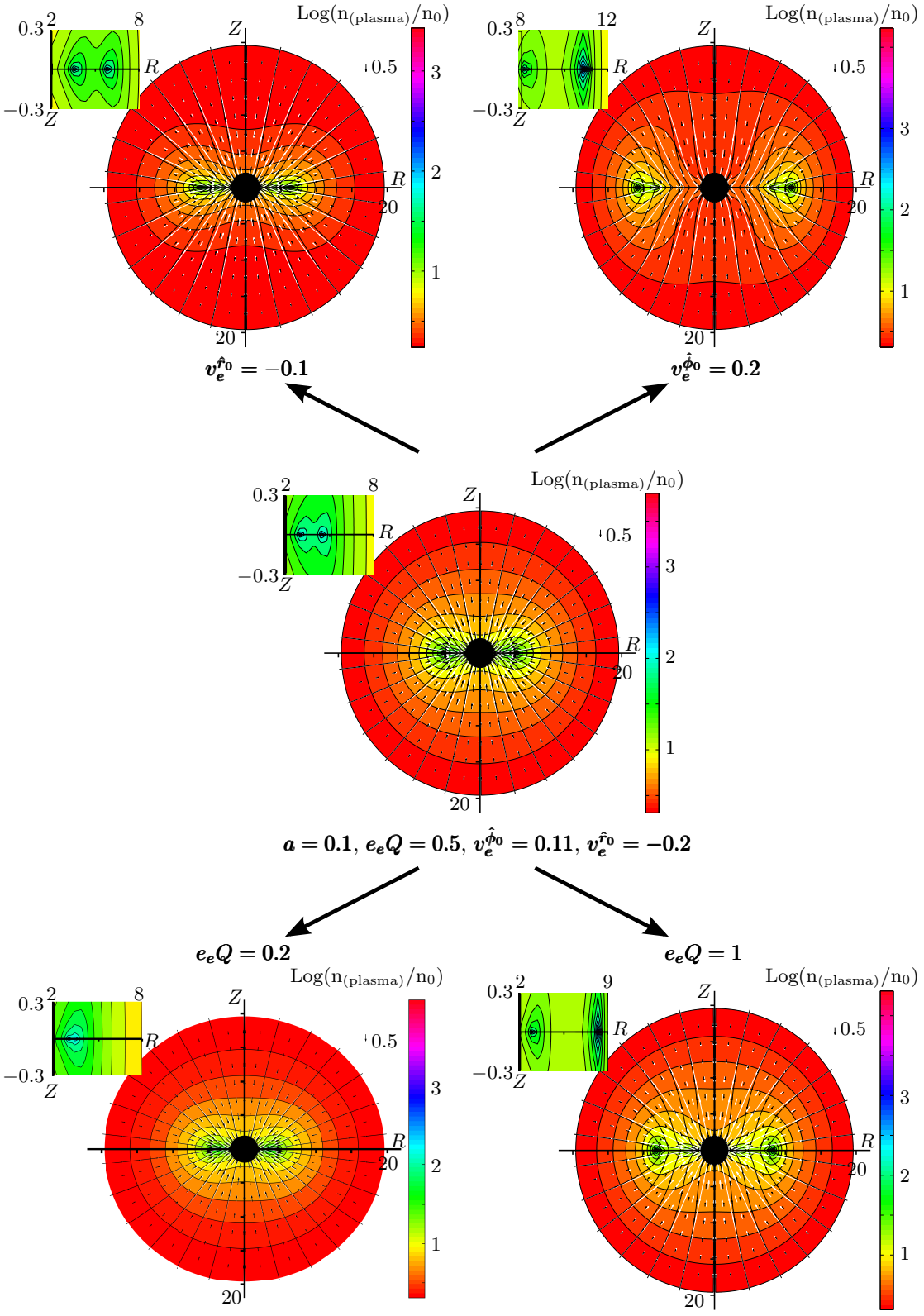

FIGURE 3.5: Streamlines, local velocity field and density field are presented for hydrogen plasma accretion by a negatively charged black hole. Parameter e_pQ, used to calculate the accretion features for protons, is given by $e_pQ = \frac{\mu_e}{\mu_p} e_eQ$. Black and white streamlines and velocity fields describe the electron and proton motion respectively. The two top and two bottom examples deviate each in only one choice for $v_e^{\hat{r}_0}$,$v_e^{\hat{\phi}_0}$ or e_eQ from the example depicted in the center. Hence, the effect of changing $v_e^{\hat{r}_0}$,$v_e^{\hat{\phi}_0}$ or e_eQ on the accretion process becomes apparent by comparing the respective example with the central one. Two density peaks arise for a plasma, which can be traced back to the differently charged particle types of the plasma. Changes in the initial conditions and black hole charge have a strong effect on all features of the accretion flow.

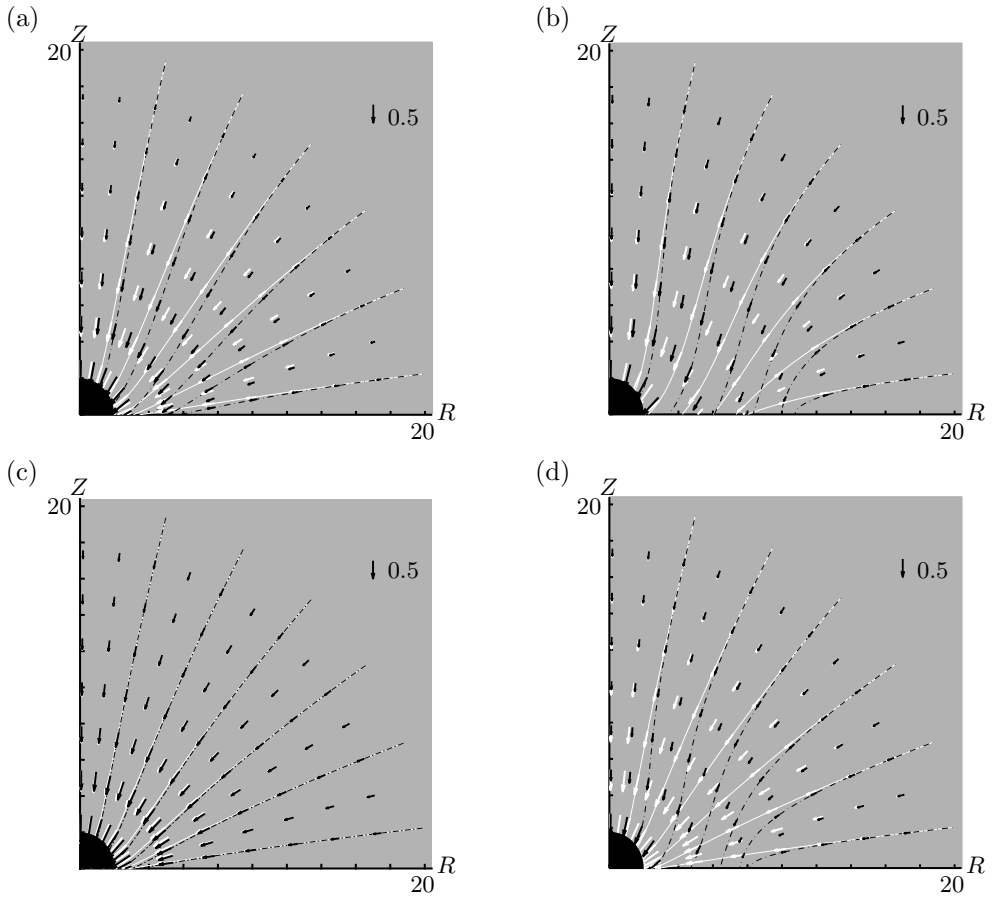

FIGURE 3.6: Streamlines and local velocity field presented separately for the examples given in Fig. 3.5. (a) Top left example in Fig. 3.5. ($v_e^{\hat{r}_0} = -0.1$, $v_e^{\hat{\phi}_0} = 0.11$, $e_\mathrm{e}Q = 0.5$); (b) Top right example ($v_e^{\hat{r}_0} = -0.2$, $v_e^{\hat{\phi}_0} = 0.2$, $e_\mathrm{e}Q = 0.5$) ; (c) Bottom left example ($v_e^{\hat{r}_0} = -0.2$, $v_e^{\hat{\phi}_0} = 0.11$, $e_\mathrm{e}Q = 0.2$); (d) Bottom right example ($v_e^{\hat{r}_0} = -0.2$, $v_e^{\hat{\phi}_0} = 0.11$, $e_\mathrm{e}Q = 1$); The spin parameter is set to $a = 0.1$ for all plots. The plot for the central example is already presented in Fig. 3.4 (a) (left).

Hence, all terms in the various equations for the accretion features under discussion can be neglected, that contain Q, but not e.

Two density peaks will arise at the equatorial plane for plasma accretion (see Figs. 3.4, 3.5 and 3.7). They are each caused by one of the two plasma particle types, distinguished by their different specific charges – here e_e and e_p. From Figs. 3.4, 3.5 and 3.7 it can also be concluded, that the positions of the density peaks coincide with the outer edge locations of the respective particle type.

Figure 3.4 pictures two examples for plasma accretion with the same initial conditions and back hole charge, but different spin parameters. A variation of a affects the accretion flow only slightly. A small shift in the position of the density peaks towards bigger radii is detected for bigger values of a, while the distance between the peaks does not seem to be effected. The overall structure of the accretion flow stays the same. The influence

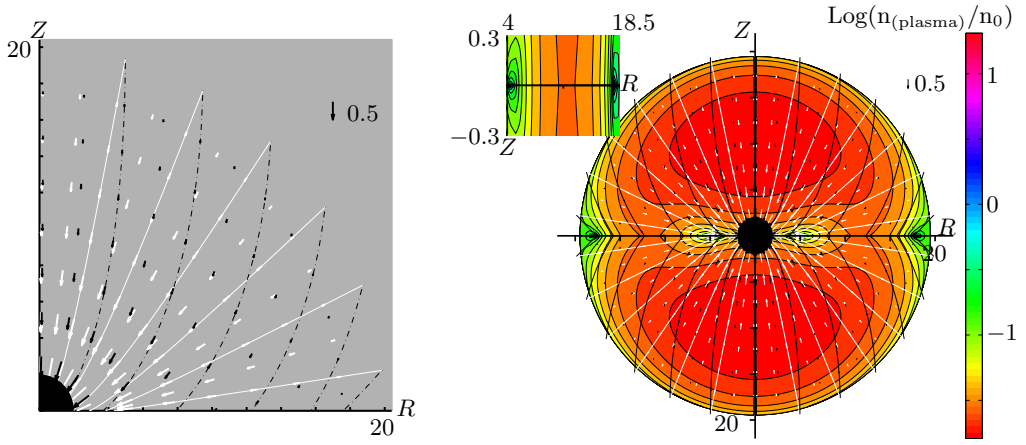

FIGURE 3.7: Streamlines, local velocity field (left and right) and density field (right) presented for the accretion of hydrogen plasma by a negatively charged black hole with $a = 0.1$, $e_{\mathrm{e}}Q = 0.5$, $v_e^{\hat{\phi}0} = 0.11$ and a very small value for the initial local velocity in radial direction $v_e^{\hat{r}0} = -0.001$. The result is a weak particle infall, which leads to very small density values, and a big effect of the attractive or repulsive electromagnetic forces on protons or electrons respectively in the accretion flow.

of the black hole spin a on the structure of the accretion flow and on the position of the density peaks was discussed in detail by Tejeda et al. [82] for the uncharged case, focusing on the effects of frame-dragging. One of which is the shift of the outer edge of the accretion disc towards bigger radii, for otherwise same initial conditions. The effect is reproduced here in the case of plasma accretion. For more details of the influence of the spin parameter see Tejeda et al. [82].

The influence of the initial conditions $v_e^{\hat{r}0}$, $v_e^{\hat{\phi}0}$ and the black hole charge $e_{\mathrm{e}}Q$ on the accretion flow and on the location of the density peaks is analyzed by comparing example plots, which differ from each other only in one choice for $v_e^{\hat{r}0}$, $v_e^{\hat{\phi}0}$ or $e_{\mathrm{e}}Q$. The streamlines and local velocity field are presented in Fig. 3.6 and furthermore in Fig. 3.5 in combination with the density field.

As one can see in the direct comparison in Figs. 3.5 and 3.6, the initial conditions $v_e^{\hat{r}0}$, $v_e^{\hat{\phi}0}$ and black hole charge $e_{\mathrm{e}}Q$ effect the accretion flow structure and peak location considerably. Larger values for $v_e^{\hat{r}0}$ and $v_e^{\hat{\phi}0}$ result in more strongly curved streamlines and density peaks located at bigger radii. This effect is reproduced in Figs. 3.8 and 3.9 due to the equivalence of the position of the outer edge r_{D} and the density peak. Figures 3.8 and 3.9 plot the location of the outer edge of the accretion disc depending on $v_e^{\hat{r}0}$, $v_e^{\hat{\phi}0}$ and $e_{\mathrm{e}}Q$.

An increasing value of the black hole net charge in $e_{\mathrm{e}}Q$ has a reverse effect on the two particle types of the plasma. While big values of $e_{\mathrm{e}}Q$ support a radial infall for protons, the streamlines of electrons on the other hand are more strongly curved, which leads to bigger values of the accretion disc's outer edge created by the electrons. The effect of

	Example 1	Example 2
$v_e^{\hat{\phi}_0}$	0.11	0.11
$v_e^{\hat{r}_0}$	-0.27	-0.001
eQ_1	-0.5	0.5
eQ_2	0	0.7
$\Delta r_{\mathrm{D}}(eQ_1 \to eQ_2)$	≈ 0.5	≈ 6

TABLE 3.1: Change of the the outer edge position Δr_{D} for a variation of eQ from eQ_1 to eQ_2 for two sets of initial local velocities and eQ: Example 1 and example 2. A variation of eQ results in a significant bigger change of r_{D} in example 2, where bigger values for $v_e^{\hat{r}_0}, v_e^{\hat{\phi}_0}$ and eQ are chosen.

eQ on the position of the outer edge is depicted in Fig. 3.8. As a result, the distance between the density peaks increases for increasing values of the black hole net charge, as one can see when comparing the bottom two example plots with the central plot in Fig. 3.5. Due to the equivalence of density peak and outer edge location of the respective plasma particle type, the effect is reproduced in Fig. 3.8, where one needs to compare the difference between the value of r_{D} for electrons ($eQ = e_{\mathrm{e}}Q$) and protons ($eQ = e_{\mathrm{p}}Q = \frac{\mu_{\mathrm{e}}}{\mu_{\mathrm{p}}} e_{\mathrm{p}}Q$) for the same initial conditions.

An example for an extreme case is pictured in Fig. 3.7. Here the absolute value of the initial local velocity in radial direction $\left|v_e^{\hat{r}}\right|$ is chosen very small, which describes a very slow particle infall. This leads on the one hand to very small density values (see Eq. (3.20)), on the other hand the attractive and repulsive electromagnetic forces on the plasma particles effect their course more strongly, leading to huge deviations in their courses. The strong deviations of the streamlines are seen in Fig. 3.7. While protons show a rather radial infall, the streamlines of the repulsed electrons have the typical course of a small value for

$$dr/d\theta = \sqrt{\mathbf{R}(r)/\Theta(\theta)}\,.$$

The radial velocity $\dot{r} = \mathbf{R}(r)$ stays small in the case of a repulsive electromagnetic force. The strong effect of a change in eQ on the accretion flow for a slow radial infall can also be seen in the behavior of r_{D} in Fig. 3.8, where r_{D} grows faster for bigger eQ the smaller the initial absolute value $|v_e^{\hat{r}}|$.

3.6.2.1 The Accretion Disc

The extent of the developed accretion disc is – according to the used model – bordered by the its inner and outer edge. The inner and outer edge are defined as discussed in Sec. 3.5, and are different for each particle type.

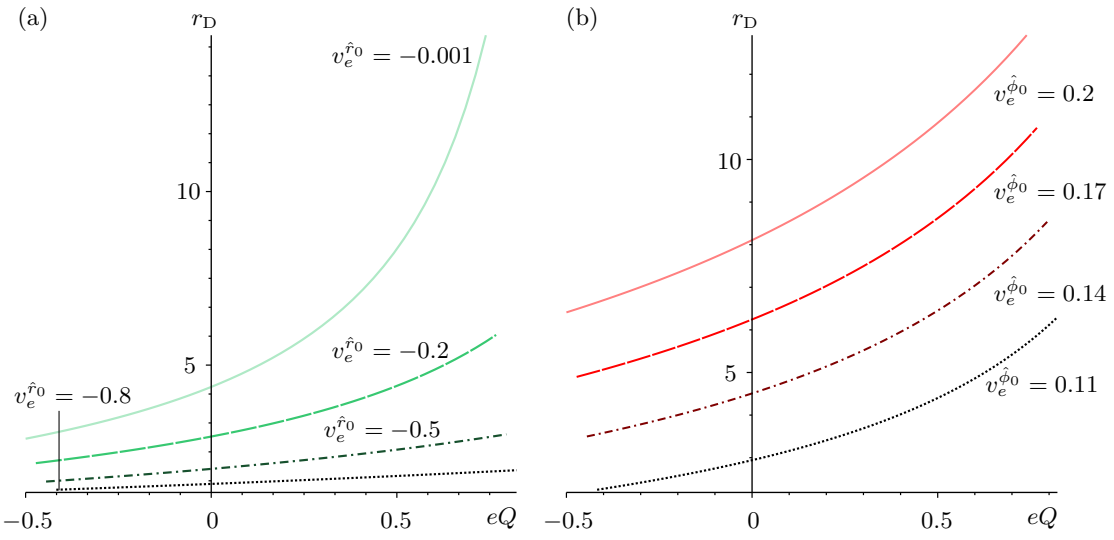

FIGURE 3.8: Outer edge r_D of the forming accretion disc as a function of eQ for $r_0 = 20$ and $a = 0.1$ for different initial conditions of the local velocity field components $(v_e^{\hat{r}_0}, v_e^{\hat{\phi}_0})$. In (a) different $v_e^{\hat{r}_0}$ are depicted for $v_e^{\hat{\phi}_0} = 0.11$. In (b) different $v_e^{\hat{\phi}_0}$ are depicted for $v_e^{\hat{r}_0} = -0.2$. The dependence of r_D on eQ increases with growing values of $v_e^{\hat{\phi}_0}$ and $v_e^{\hat{r}_0}$.

Figures 3.8 and 3.9 present the effect of the initial conditions $v_e^{\hat{r}_0}$, $v_e^{\hat{\phi}_0}$ and black hole net charge in form of eQ on the position of the outer edge r_D. According to these plots the change in r_D (dr_D/dp for $p \in \left\{v_e^{\hat{r}_0}, v_e^{\hat{\phi}_0}, eQ\right\}$) is largest for big values of the initial local velocities and eQ. A change in the position of r_D for a variation of $v_e^{\hat{r}_0}, v_e^{\hat{\phi}_0}$ or eQ is significant only if $v_e^{\hat{r}_0}, v_e^{\hat{\phi}_0}$ and eQ are chosen sufficiently big. This behavior is emphasized in table 3.1. This correlation further leads to an increasing difference between the position of the outer edge for electrons ($eQ = e_eQ$) and protons ($eQ = e_pQ$) for a bigger choice of e_eQ or the initial local velocities. This expresses itself in a rising gap between the density peaks not only for bigger values of eQ, but also of $v_e^{\hat{r}_0}$ and $v_e^{\hat{\phi}_0}$.

In case of hydrogen plasma two different values for both the ISCO and r_D are calculated for given initial conditions, one for the electrons and one for the protons. Which values for the ISCO and r_D serve as the true inner and outer edge of the fed accretion disc depends on the initial conditions. Four different scenarios of accretion discs will be discussed in the following. They arise from the fact, that the outer edge of one or both plasma particle types can be smaller than the corresponding ISCO. The specific charge of plasma particles with an opposite charge to the black hole are denoted as e_1 ($e_1Q < 0$), while e_2 denotes the specific charge of plasma particles with the same charge as the black hole ($e_2Q > 0$).

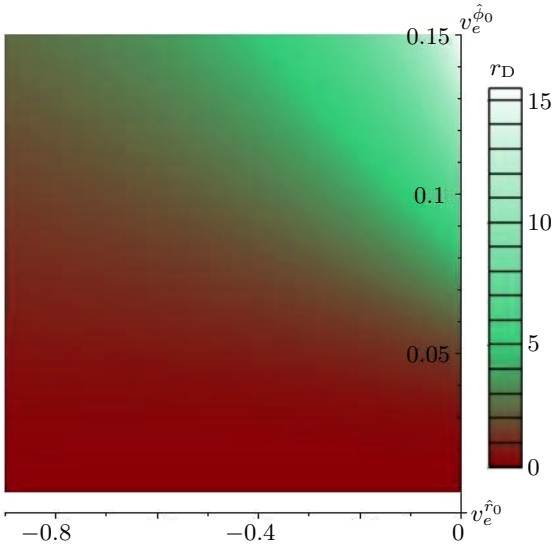

FIGURE 3.9: Outer edge r_D of the forming accretion disc as a function of $v_e^{\hat{\phi}_0}$ and $v_e^{\hat{r}_0}$ for $r_0 = 20$, $e_e Q = 0.5$ and $a = 0.1$. The changes of r_D become bigger for bigger values of $v_e^{\hat{\phi}_0}$ and $v_e^{\hat{r}_0}$.

Case 1: No main accretion disc $r_{ISCO}(e_1 Q) > r_D(e_1 Q)$ and $r_{ISCO}(e_2 Q) > r_D(e_2 Q)$

All plasma particles reach the equatorial plane at radii smaller than their corresponding ISCO. This scenario is schematically shown in Fig. 3.10 (a). All accreted plasma is bound to spiral into the black hole, and might form a minidisc during this process. It will not contribute to or form a main accretion disc. This scenario is realized for small enough $v_e^{\hat{r}_0}$ and $v_e^{\hat{\phi}_0}$, e.g. for a negatively charged black hole with $a = 0.1$, $e_2 Q = e_e Q = 0.5$, $e_1 Q = e_p Q = -0.00027$ and all values for $v_e^{\hat{r}_0}$ and $v_e^{\hat{\phi}_0}$ for which $r_D \lesssim 5.5$ (compare Figs. 3.8 and 3.9).

Case 2: Accretion disc fed by plasma particles with eQ>0 $r_{ISCO}(e_1 Q) > r_D(e_1 Q)$ and $r_{ISCO}(e_2 Q) < r_D(e_2 Q)$

All particles with a charge opposite to the black hole are bound to spiral into it. In contrast to this, the majority of streamlines for particles with the same charge as the black hole reach the equatorial plane for radii bigger than the corresponding ISCO, contributing to or forming an accretion disc. This is the case for any $r_D(e_2 Q) > r_{ISCO}(e_2 Q)$, since the density peak is located right at r_D. A schematic plot is depicted in Fig. 3.10 (b). In this scenario the accretion disc should slowly develop the same charge as the black hole, until the electromagnetic field created by the disc's charge is not negligible anymore and the description of the model breaks down. The scenario occurs for e.g. $a = 0.1$, $e_2 Q = 0.5$, $e_1 Q = -0.00027$, $v_e^{\hat{r}_0} = -0.2$ and $v_e^{\hat{\phi}_0} = 0.13$ in case of a negatively charged black hole.

Case 3: Accretion disc fed by both plasma particle types $r_{ISCO}(e_1 Q) < r_D(e_1 Q)$ and $r_{ISCO}(e_2 Q) < r_D(e_2 Q)$

The majority of the streamlines for both plasma particle types reach the equatorial plane at radii bigger than the corresponding ISCO (depicted in Fig. 3.10 (c), (d)). Since r_{D} and the ISCO are smaller for plasma particles with a charge opposite to that of the black hole than for those with a charge of the same sign as the black hole, the used model predicts an inner and outer area of the accretion disc. The inner area is dominated by oppositely charged plasma particles ($e_1 Q < 0$), while the outer area is dominated by plasma particles of the same charge ($e_2 Q > 0$) as the black hole. However, interactions between the plasma particles should not be neglected at the accretion disc and their interactions might prevent the development of differently charged areas within the accretion disc. Like in case 2, the model description beaks down, if the electromagnetic field created by the oppositely charged areas cannot be neglected anymore. This scenario occurs for sufficiently big values of $v_e^{\hat{r}_0}$ and $v_e^{\hat{\phi}_0}$, e.g. for a negatively charged black hole with $e_2 Q = 0.5$, $e_1 Q = -0.00027$ and initial local velocities $v_e^{\hat{r}_0} = -0.2$ and $v_e^{\hat{\phi}_0} \geq 0.17$.

Case 4: Accretion disc fed by plasma particles with eQ<0 $r_{\mathrm{ISCO}}(e_1 Q) < r_{\mathrm{D}}(e_1 Q)$ and $r_{\mathrm{ISCO}}(e_2 Q) > r_{\mathrm{D}}(e_2 Q)$

All particles with the same charge as the black hole are bound to spiral into it, while the majority of oppositely charged particles contribute or form the accretion disc in the equatorial plane. A schematic plot is given in Fig. 3.10 (e). In this scenario the accretion disc slowly develops a charge, which is opposite to the black hole charge. It can occur for very big values of $e_{\mathrm{e}} Q \to 1$ and sufficiently big values of $v_e^{\hat{r}_0}$ and $v_e^{\hat{\phi}_0}$. However, $r_{\mathrm{D}}(e_2)$ is always located at a bigger radius than $r_{\mathrm{D}}(e_1)$, so plasma particles with the same charge as the black hole will have to pass through the area, where the oppositely charged plasma particles are accumulated, while spiraling inwards. Interactions between the plasma particles have to be expected at this point, and the models prescription breaks down. These interactions probably prevent the oppositely charged plasma particles to actually fall into the black hole. An accretion disc, which slowly develops a charge with the same sign as the black hole, is an interesting but also rather unlikely scenario.

As already mentioned under case 1, minidiscs might form at radii smaller than the determined inner edge of the main accretion disc, where the matter is bound to spiral into the black hole [97, 98]. Particles hitting the equatorial plane for radii larger than r_{ISCO} may in principle also loose so much energy that they, as well, are bound to spiral into the black hole, contributing to or forming a minidisc. However, since the description of this process is beyond the used model, this topic will only be mentioned here and not discussed any further.

3.7 Restrictions to the Model's Application Area due to Electromagnetic Particle Interactions

The negligence of all particle interactions, especially the electromagnetic interactions, in the used model has its limits. The model predicts two local density maxima, occurring at the equatorial plane, in case of plasma accretion – one for each plasma particle type – with a very sharp density peak at its center. At the center the electromagnetic particle interactions will most likely not be negligible anymore. Arising repulsive electromagnetic forces will soften the sharp peaks. Since these peaks lie on the equatorial plane, they are additionally, and probably much more significantly, effected by the accretion disc, which is assumed to be located at the equatorial plane.

Therefore neglecting particle interactions restricts the choice for the initial particle density n_0 at r_0. The electromagnetic field, created by the accreted plasma, should still be negligible compared to the field created by the central black hole. In general, changing r_0 to bigger values raises the strength of the electromagnetic field of the infalling particles at the outer area, while at the same time the black hole's electromagnetic field falls off. Therefore n_0 has to be chosen smaller for larger values of r_0.

However, the limit for n_0 is derived primarily from an estimation of the strength of the electromagnetic field created by the density peaks at the equatorial plane, which in turn depends on the choice of r_0, the total black hole mass M, and on the position of the density peaks. The further the density peaks are located away from the black hole, the bigger becomes their contribution to the total electromagnetic field, since the black hole field falls off in radial direction. This results in smaller maximal

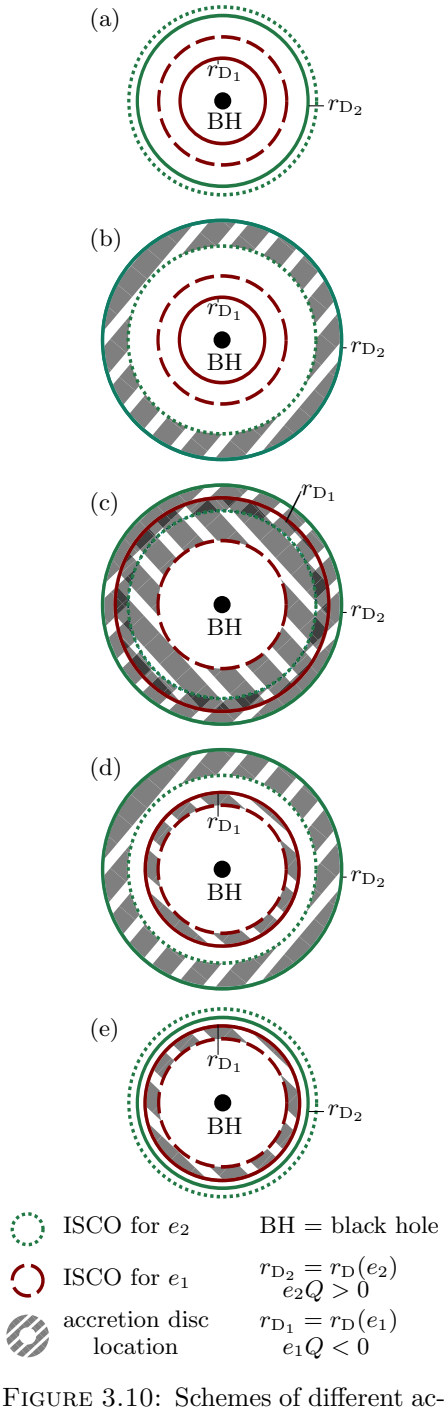

FIGURE 3.10: Schemes of different accretion disc scenarios. If the outer edge is smaller than the corresponding ISCO the respective plasma particles do not form an accretion disc. The depicted scenarios are described in detail in Sec. 3.6.2.1, case 1 - case 4.

values for n_0. While the total black hole charge Q scales with M [3], the total charge in an area volume scales with M^3. Bigger values for M therefore further restrict the choice of n_0.

To roughly estimate the upper limit of the initial particle density n_0 the electromagnetic field created by the plasma density peaks is approximated by the electric field of two charged rings around the black hole in the non-relativistic limit. According to this estimation, the plasma density is restricted to values smaller than 10-0.01 cm^{-3} for a stellar black hole with a net charge of 10^{-18} - 10^{-21}. These densities are typical for interstellar or interplanetary plasmas. The density has to be even more dilute for more massive black holes or bigger chosen values of r_0.

[3] $Q = M\,\bar{Q}$ given in the initial notation used up until Sec. 2.4.1

Chapter 4

Charged Polish Donuts in Electromagnetic Background Fields

In the second main topic the focus lies on the discussion of accretion discs with non-neutral charge distributions, and how their structure and position are effected by the presence of electromagnetic background fields.

Center of discussion is a charged, thick accretion disc, whose matter is dense enough, so that the fluid approach is applicable. Furthermore – in contrast to the approach in ideal MHD (Sec. 2.3), where the conductivity is assumed to be infinite – the discussed fluid here is non-conductive. It could describe a partly ionized, non-neutral helium plasma with high pressures, low temperatures and therefore high densities [42].

Since the scenario is treated analytically, massive simplifications of the described situation are brought to the scene. The major points of radiation, a form of energy loss of the system, and, connected to that, even the process of accretion itself will not be described by the used analytic model. The advantages however are, as mentioned in the previous chapter, a "simple" description of the pure effects of the aspect of interest, which helps gaining a basic understanding of the physical process.

First approaches to analytically describe the effects of an electromagnetic field on an accretion disc are done by Komissarov [37], who took a toroidal magnetic field in the accretion disc into account. Non-neutral accretion discs effected by a background electromagnetic field were discussed by Kovář et al. [88, 41, 42] in the Schwarzschild spacetime for a electrically charged central object, a uniform magnetic field, or a dipole magnetic field, respectively.

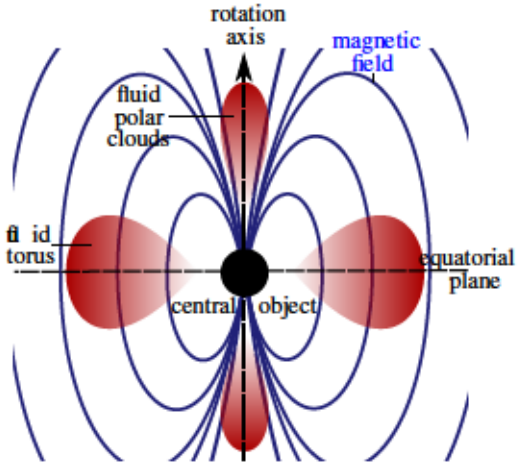

FIGURE 4.1: Sketch of the considered situation. The dipole test-field is aligned to the rotation of the compact object (e.g. a magnetar).

In this section a general procedure will be introduced to find bound structures consisting of a charged fluid in axially and reflection symmetric spacetimes and electromagnetic fields. The effects of the choice for the charge distribution and the spin of the accreting object are discussed in detail in the context of a spinning central object with a dipole magnetic field. Furthermore a summary is given of the results in [2], where charged fluid structures are considered, that are effected by a uniform magnetic background field and by an electric net charge of the spinning central object. Comparisons are drawn to the first scenario of a magnetic dipole field.

The Polish Donut model, introduced in Sec. 2.5, is used to describe the charged, thick accretion disc around some compact object as a charged, perfect, barotropic test-fluid in circular motion in the curved spacetime created by the compact object. The term "test" indicates, that the electromagnetic fields, as well as gravitational effects created by the fluid are completely neglected. A solution for a charged fluid structure around the compact object is then described by the effective potential h in Eq. (2.142).

The background field is treated as a test-field, which was introduced in Sec. 2.2.2. The described field therefore must be sufficiently small, that a negligence of its influence on the spacetime metric is justified. Both, the spacetime created by the central object, as well a the electromagnetic test-field have to be stationary and show the same axial symmetry. The spacetime metric is expressed in a spherical polar coordinate system, where it takes the form given in Eq. (2.13).

A possible situation, that will be considered later on within the framework of the introduced model, is shown in Fig. 4.1. As depicted in the example in Fig. 4.1 other than the fluid torus describing the thick accretion disc further fluid structures might be found, such as levitating tori or polar clouds [42].

4.1 Physical Characteristics of the Charged Fluid Structure

The barotropic equation of state has to be specified in order to derive the physical characteristics pressure p, energy density ε, and charge density ρ_q of the fluid from the effective potential h. In the used discussion here $p(\varepsilon)$ is specified to a polytropic equation of state

$$p = \kappa \varepsilon^{\Gamma} \,, \tag{4.1}$$

where κ and Γ are the polytropic coefficient and exponent respectively. The polytropic equation of state is a simple and widely used relation for uncharged perfect fluids. In case of high temperatures and big κ, the electrostatic effects on the equation of state can be neglected, so that the polytropic equation of state is applicable for charged fluids as well.

Pessure, energy density and specific charge density $q = \rho_q/\varepsilon$ are now expressed in terms of effective potential h, by deriving h from Eq. (2.140) for the given equation of state (4.1) and setting prefactor A in (2.140) to $A = \frac{\Gamma-1}{\Gamma}$:

$$p = \left(\frac{e^h - 1}{\kappa^{\frac{1}{\Gamma}}} \right)^{\frac{\Gamma}{\Gamma-1}} \,, \tag{4.2}$$

$$\varepsilon = \left(\frac{e^h - 1}{\kappa} \right)^{\frac{1}{\Gamma-1}} \,, \tag{4.3}$$

$$q = \frac{\rho_q}{\varepsilon} = \mathcal{K}\, e^h \,. \tag{4.4}$$

Equipotential surfaces of effective potential h coincide with surfaces of constant pressure, energy density and specific charge density.

Total mass and total charge of the charged fluid are derived by integrating rest mass density ρ_m or ρ_q over the fluid structure volume $\mathcal{V}$:

$$\mathcal{M} = \int_{\mathcal{V}} \rho_m \, d\mathcal{V} \,, \tag{4.5}$$

$$\mathcal{Q} = \int_{\mathcal{V}} \rho_q \, d\mathcal{V} \,. \tag{4.6}$$

A suitable assumption for the rest mass ρ_m of the form

$$\rho_m = \rho_m(\varepsilon, p)$$

is needed, in order to derive the mass density from the effective potential h. In a limit, where a non-relativistic approximation is valid, an appropriate estimation for ρ_m is

$$\rho_m \approx \varepsilon \,.$$

In this approximation the temperature of the fluid can be estimated. If the the pressure is of thermal nature only and no radiation or magnetic pressure [37] occur, the temperature is given by the ideal gas relation, which leads to

$$T = \frac{c^2 \langle \mu \rangle_{\mathrm{SI}}}{k_{\mathrm{B}}} \frac{p}{\rho_m} = \frac{c^2 \langle \mu \rangle_{\mathrm{SI}}}{k_{\mathrm{B}}} \left(e^h - 1 \right) ,$$

where $\langle \mu \rangle_{\mathrm{SI}}$ is the mean particle mass in the fluid and k_{B} is the Boltzmann constant, both in SI units. The temperature is determined by the composition of the fluid and overall structure of the bound fluid structure, given in terms of effective potential h. All other parameters, especially the polytropic coefficient and exponent do not effect the temperature in the fluid structure.

The rotation of the charged fluid creates a magnetic field with a magnetic field strength $\mathcal{B}$. Following the approach in [41], $\mathcal{B}$ is approximated at the edge the fluid structure by a charged ring, which contains the charge $\mathcal{Q}$ of the whole structure and rotates at the same angular velocity ω as the fluid structure at its center r_c. The approximation of the magnetic field reads for equatorial tori or polar clouds

$$\mathcal{B}_{ET} \approx \frac{\omega \mathcal{Q}}{\pi R} \qquad \text{or} \qquad \mathcal{B}_{PC} \approx \frac{R_d^2 \omega \mathcal{Q}}{\pi \left(R_d^2 + R^2 \right)^{\frac{3}{2}}} \,, \tag{4.7}$$

respectively. Here R is given by half of the equatorial torus's width, or polar cloud's hight, while R_d is given by half of the polar cloud's width. R and R_d serve to estimate the radius of the current loop in the approximation. The total mass, charge and magnetic field of the fluid structure have to be sufficiently low, so that the assumption of a test-fluid is not violated.

4.2 Construction of Charged Fluid Structures

As discussed in Sec. 2.5.4, bound structures of a charged fluid, such as a finite accretion disc, are discovered for the spacetime and electromagnetic field of choice by searching for local maxima in the effective potential h.

A procedure to find bound structures for the charged fluid is introduced in the following. Next to the required stationarity and axial symmetry the procedure assumes a reflection

symmetry at the equatorial plane ($\theta = \pi/2$) and a smooth behavior of the background field and metric in the area of the fluid structure.

Satisfaction of the necessary conditions In a first step the necessary conditions (2.144) are fulfilled for a given position (r_c, θ_c) of the structure's center. Rotation and reflection symmetry of the system require the first necessary condition ($\partial_\theta h(r_c, \theta_c) = 0$) to always be satisfied for $\theta_c = 0, \pi/2, \pi$. The procedure therefore focuses in the search for bound fluid structures to

- fluid tori centered in the equatorial plane ($\theta_c = \pi/2$) and
- polar clouds centered on the polar axis ($\theta_c = 0, \pi$).

From the second necessary condition $\partial_r h(r_c, \theta_c) = 0$ one can derive a normalization condition for $f_\mathcal{K}(S)$, the function that determines the charge distribution in the fluid structure. By introducing an arbitrary function $g(S)$ of S, normalized to 1 at the structure's center: $g(S)\big|_{r=r_c,\theta=\theta_c} = 1$, the normalization condition for $f_\mathcal{K}(S)$ is given by

$$f_\mathcal{K}(S) = b\, g(S)\,. \tag{4.8}$$

The value of b is now determined by satisfying the second necessary condition, using Eq. (2.141):

$$f_\mathcal{K}(S)(r_c, \theta_c) = \frac{\partial_r \mathcal{P}}{2\mathcal{P}} \frac{1}{\partial_r S}\Big|_{r=r_c,\theta=\theta_c} =: b\,. \tag{4.9}$$

From Eq. (4.9) it becomes apparent, that the electromagnetic force acting on the charged fluid at the extremal points of effective potential h is repulsive, if

$$\partial_r \mathcal{P}|_{r=r_c,\theta=\theta_c} > 0\,, \tag{4.10}$$

since $\partial_r S f_\mathcal{K}(S) > 0$ for repulsive electromagnetic forces along r on the fluid (see Eqs. (2.131),(2.139)).

Satisfaction of the sufficient conditions In a second step the conditions for a local minimum are fulfilled. In the discussed case, where a reflection symmetry is present at $\theta = \pi/2$, the sufficient conditions (2.145) for a maximum reduce to

$$\partial^2_{rr} h(r_c, \theta_c) < 0, \qquad \partial^2_{\theta\theta} h(r_c, \theta_c) < 0\,. \tag{4.11}$$

for $\theta_c = 0, \pi/2, \pi$, since the off-diagonal elements of Hessian $\mathcal{H}$ of h (2.143) vanish for these values of θ_c.

The sufficient conditions (4.11) can be explicitly written out by using the definition for h in Eq. (2.142):

$$0 > \frac{\Gamma - 1}{\Gamma} \left\{ -\mathcal{P}\partial_{rr}^2\mathcal{P} + (\partial_r\mathcal{P})^2 + \mathcal{P}\frac{\partial_r\mathcal{P}}{\partial_r S}\left(\partial_{rr}^2 S + \frac{f'_{\mathcal{K}}}{f_{\mathcal{K}}}(S)\ (\partial_r S)^2\right)\right\}\Big|_{r=r_c,\theta=\theta_c}, \tag{4.12}$$

$$0 > \frac{\Gamma - 1}{\Gamma} \left\{ -\partial_{\theta\theta}^2\mathcal{P} + \frac{\partial_r\mathcal{P}}{\partial_r S}\,\partial_{\theta\theta}^2 S\right\}\Big|_{r=r_c,\theta=\theta_c}. \tag{4.13}$$

Relation (4.12) can be satisfied by restricting the choice of $f_{\mathcal{K}}(S)$ for arbitrary angular velocities ω. The second inequality (4.13) restricts the choice for ω, since $f_{\mathcal{K}}(S)$ and its derivative do not appear in relation (4.13). However in the explicit case, which is discussed in the following section 4.4, $g(S)$ in Eq. (4.8) is chosen first, before satisfying both conditions (4.12)-(4.13) by a restriction to the choice of ω. This is motivated by comparing the found results with the results in [41, 42].

The outer edge of the bound structure After a local maximum is found in the effective potential, the outer edge of the fluid structure is determined by the choice for integration constant h_0. If a cusp point exists (see Sec. 2.5.4) and the equipotential curve running through it is closed, h_0 is chosen such that the equipotential curve of the cusp point marks the edge of the fluid structure:

$$h\left(r_{\text{cusp}}, \theta_c\right) = 0\,.$$

By this choice the cusp point marks the point, where matter flows out of the bound fluid structure, and is possibly accreted by the central object.

Consistency check of the model Finally it has to be made sure, that the initial assumption of a negligible electromagnetic field created by the fluid structure is still valid:

$$F^{\mu\nu}_{INT} << F^{\mu\nu}_{EXT}\,.$$

The density of the charged fluid is set sufficiently small by choosing scaling factor κ in the equation of state (4.1) accordingly. Limits to the diluteness of the fluid are given by the used magnetohydrodynamical approach, which still has to be applicable.

4.3 Rigidly Rotating, Uncharged Fluid Structures in Kerr Spacetime

Rigidly rotating, uncharged fluid structures in Kerr spacetime represent the uncharged limit of both examples for charged fluids in electromagnetic background fields, that will be treated in the following sections of this chapter. Polish Donuts in Kerr spacetime were discussed by Daigne and Font [99] for a non-constant angular momentum distribution. However, when demanding a distribution that corresponds to rigid rotation, as it will be necessary in the following charged scenarios, no solutions are found for a bound fluid structure. This will be derived in the following.

The necessary conditions for a bound solution reduces in the uncharged case to (see Eq. (2.141), $\mathcal{P} > 0$)

$$\partial_\mu \mathcal{P} = 0 \text{ for } \mu = r, \theta \,, \tag{4.14}$$

while the effective potential h (2.142) takes the form

$$h_{nocharge} = -\frac{A}{2} \ln \mathcal{P} + h_0 \,. \tag{4.15}$$

The necessary condition for $\mu = \theta$ (4.14) can only be satisfied for $\theta = 0, \pi/2, \pi$. This restricts the location of possible center of fluid structures to the equatorial plane or to the rotation axis.

On the rotation axis ($\theta = 0, \pi$), $\mathcal{P}$ reduces to

$$\mathcal{P}\Big|_{\theta=0} = \frac{\Delta(r)}{r^2 + a^2} \,, \tag{4.16}$$

which is independent from ω. It approaches one in the limit $r \to \infty$ and becomes zero at the outer horizon r_+. This behavior of $\mathcal{P}\Big|_{\theta=0}$ leads to a divergence of the effective potential $h_{nocharge}\Big|_{\theta=0,\pi}$ at the outer horizon, while it approaches h_0 for $r \to \infty$. A plot of $h_{nocharge}\Big|_{\theta=0,\pi}$ is given in Fig. 4.2 (a) for two different values of spin a. The second necessary condition is given by

$$\partial_r \mathcal{P}\Big|_{\theta=0} = 2\frac{r^2 - a^2}{\left(r^2 + a^2\right)^2} = 0 \,, \tag{4.17}$$

which is satisfied only for $r = a$. This radius always lies behind the outer Kerr-horizon r_+. Hence, no polar clouds can exist in the uncharged limit.

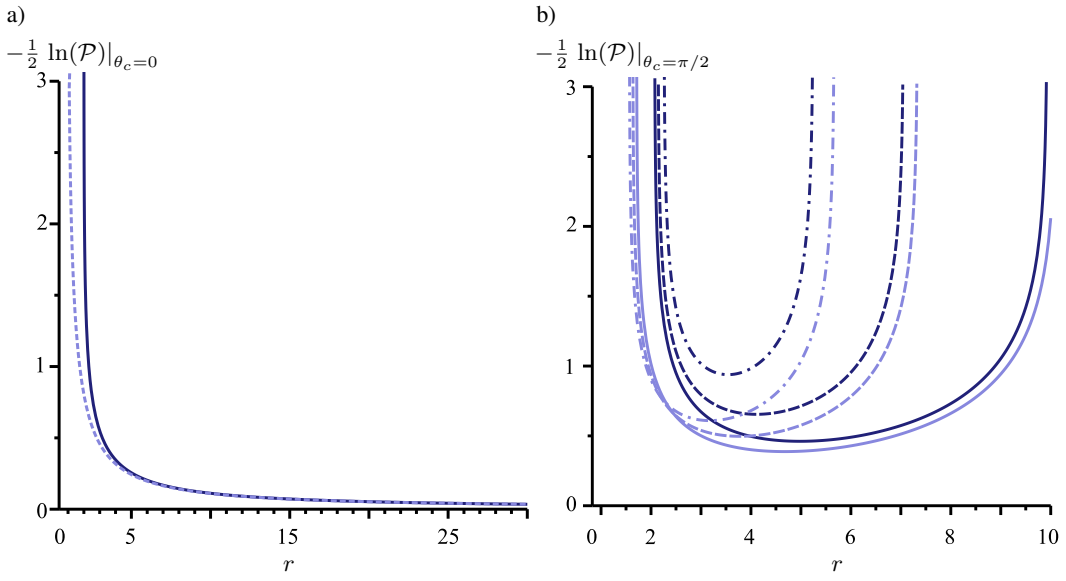

FIGURE 4.2: $-\frac{1}{2}\,\mathcal{P}|_{\theta=\theta_c}$ plotted over r for (a) $\theta_c = 0$ and (b) $\theta_c = \pi/2$. Dark and light blue lines correspond to $a = 0$ and $a = 1$ respectively. $\mathcal{P}|_{\theta=0}$, plotted in (a) is independent of ω, in contrast to $\mathcal{P}|_{\theta=\pi/2}$ plotted it (b), where solid lines correspond to $\omega = 0.09$, dashed lines to $\omega = 0.12$ and dash-dotted lines to $\omega = 0.15$. The region for r in which the plotted term shows real values shrinks with rising ω, since superluminal motion of the fluid is reached for smaller radii.

At the equatorial plane ($\theta = \pi/2$), $\mathcal{P}$ reduces to

$$\mathcal{P}\Big|_{\theta=\pi/2} = \frac{1}{r}\left(2 - r + 4a\omega - (r(r^2+a^2)+2a^2)\omega^2\right) . \tag{4.18}$$

$\mathcal{P}\Big|_{\theta=\pi/2}$ approaches $-\infty$ for $r \to \pm\infty$. The effective potential $h_{nocharge}\Big|_{\theta=\pi/2}$ takes real values only for $\mathcal{P} > 0$, which corresponds to a subluminal motion of the fluid (see Sec. 2.5.1). In Fig. 4.3 $\mathcal{P}\Big|_{\theta=\pi/2} = 0$ is plotted over r and ω for different values of the spin. Condition $\mathcal{P} > 0$ is satisfied for points (r, ω) from the area confined by the $\mathcal{P} = 0$-curve. The confined area is reflection symmetric with respect to $\omega = 0$ in case of $a = 0$, whereas it looses its symmetry for $a > 0$ – a result of the frame dragging effect. Larger values of ω are favored, especially for small radii. The ergoregion ($r_+ < r < 2$ for $\theta = \pi/2$), where the fluid has to move with the rotation of the central object ($\omega > 0$), is also reproduced in Fig. 4.3, where the confined area is located solely at $\omega > 0$ for $r < 2$. For points (r, θ), that lie on the $\mathcal{P} = 0$-curve, the circular fluid motion reaches the velocity of light, building an inner and outer limit for the expanse of a fluid structure in rigid rotation. The effective potential along the equatorial plane is depicted in Fig. 4.2 (b) for different values of a and ω. The potential is defined in between the nodes of $\mathcal{P}\Big|_{\theta=\pi/2}$, where $\mathcal{P}\Big|_{\theta=\pi/2} > 0$ and diverges at the nodes. A higher rigid rotation of the fluid reduces the range of r, where $h_{nocharge}\Big|_{\theta=\pi/2}$ takes real values, and the fluid motion is subluminal. The effective potential at the equatorial plane does not show local maxima for any value

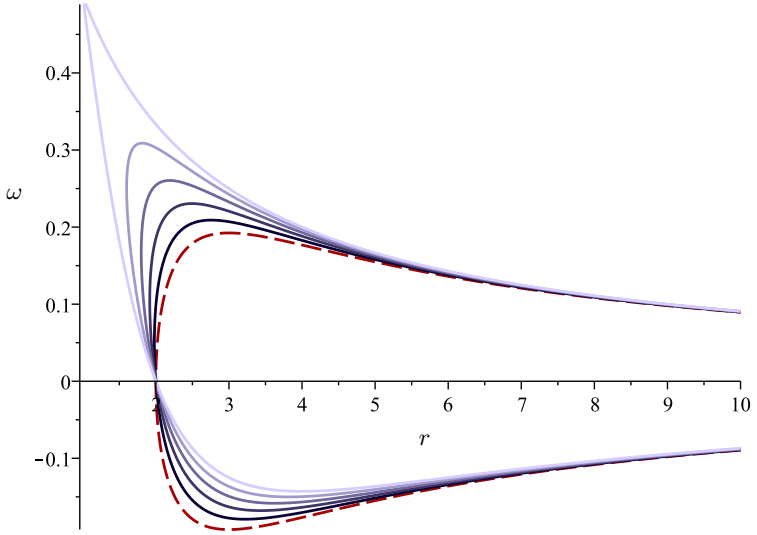

FIGURE 4.3: $\mathcal{P}|_{\theta=\pi/2} = 0$ as a function of r and ω for different values of a. The red dashed line shows the limit $a = 0$. From dark to light blue the value of a rises in 0.2- steps to $a = 1$. The fluid of the torus can only rotate at r with an ω for which $\mathcal{P}|_{\theta=\pi/2} > 0$, which is fulfilled in the area enveloped by the graphs. The shift, especially at small radii, of allowed ω to larger values for bigger a is due to the frame dragging effect.

of a and ω, since the first sufficient condition for a local maximum at $\theta = \pi/2$ (see Eq. (4.11))

$$\partial^2_{rr} h_{nocharge}\Big|_{\theta=\pi/2} = \frac{((2a^2+r^3)\omega - 2a)^2 + 2r^3}{r^3(2a^2+r^3)\,\mathcal{P}|_{\theta=\pi/2}} + \frac{(\partial_r \mathcal{P})^2}{2\mathcal{P}^2}\Big|_{\theta=\pi/2} < 0 \tag{4.19}$$

is not fulfilled for any positive r and $\mathcal{P}$. Therefore equatorial tori cannot be found as well.

To sum it up, no bound fluid structures are found in the limiting case of an uncharged fluid in rigid rotation.

4.4 Charged Fluid Structures around a Rotating Compact Object with a Dipole Magnetic Field

The introduced model and procedure is now applied to find charged fluid structures around a rotating compact object with a dipole magnetic field (e.g. a magnetar).

The rotating compact object is approximated by Kerr spacetime (2.14) (for $Q = P = 0$), while the dipole magnetic field, produced by the object, is described by the test-field of a magnetic dipole in Kerr spacetime (2.27)-(2.28), which was discussed in Sec. 2.2.2.1. The magnetic dipole has to be oriented along the rotation axis of the compact object

to obtain the symmetries which are necessary for an application of this model. The appearance of both a t- and ϕ-component in the electromagnetic potential of a magnetic dipole arises from frame-dragging and demands that the charged fluid has to be

- non-conductive ($\sigma = 0$) and
- in rigid rotation ($\omega = const.$).

More complicated spacetimes could be used to describe the rotating compact object within this model (see [100, 101] and citations within), as long as it contains the mentioned symmetries. This would however obviously complicate the analysis accordingly, which is why Kerr spacetime is used here as a description of the compact object. The discussion of the charged fluid structures in Kerr spacetime with a dipole magnetic test-field is a generalization of the scenario discussed in [42], where the Schwarzschild metric was used. A focus will therefore lie on the influence of the spin onto the position, form and occurrence of the fluid structures.

The effective potential h (2.142) shows the symmetry

$$h(a, \omega, Bf_{\mathcal{K}}(S)) = h(a, \omega, -Bf_{\mathcal{K}}(S))\,. \tag{4.20}$$

A change of $Bf_{\mathcal{K}}(S) \to -Bf_{\mathcal{K}}(S)$ indicates either a flip of the magnetic field, or a change of the fluid charge to $-\rho_q$, since $f_{\mathcal{K}}(S) = \frac{\rho_q}{p+\varepsilon}U^t$. This symmetry allows to restrict the discussion to $a > 0$.

Bound solutions for fluid structures in rigid rotation are possible only if the fluid is charged and the second term in Eq. (2.142) does not vanish. Function $f_{\mathcal{K}}(S)$ in the second term determines the charge distribution throughout the fluid structure. The interaction of the charged fluid with the electromagnetic background field causes a repulsive or attractive force (see Eqs. (2.131),(2.139)) proporional to

$$f_{\mathcal{K}}(S)\partial_\mu S = f_{\mathcal{K}}(S)(\partial_\mu A_t + \omega\partial_\mu A_\phi)\,. \tag{4.21}$$

With the right strength it stabilizes the fluid in rigid rotation, so that a bound fluid structure is formed.

In case of $\partial_r \mathcal{P} > 0$ a repulsive electromagnetic force is needed according to Eq. (4.10) to build a bound fluid structure, by preventing the charged fluid from falling onto the central object. Vice versa an attractive force is needed, wehen $\partial_r \mathcal{P} < 0$. In the effective potential $h_{nocharge}$ $\partial_r \mathcal{P} > 0$ occurs on the rotation axis for all radii and at the equatorial plane for all radii smaller than the minimum location of $h_{nocharge}\Big|_{\theta=\pi/2}$ (see Fig.4.3

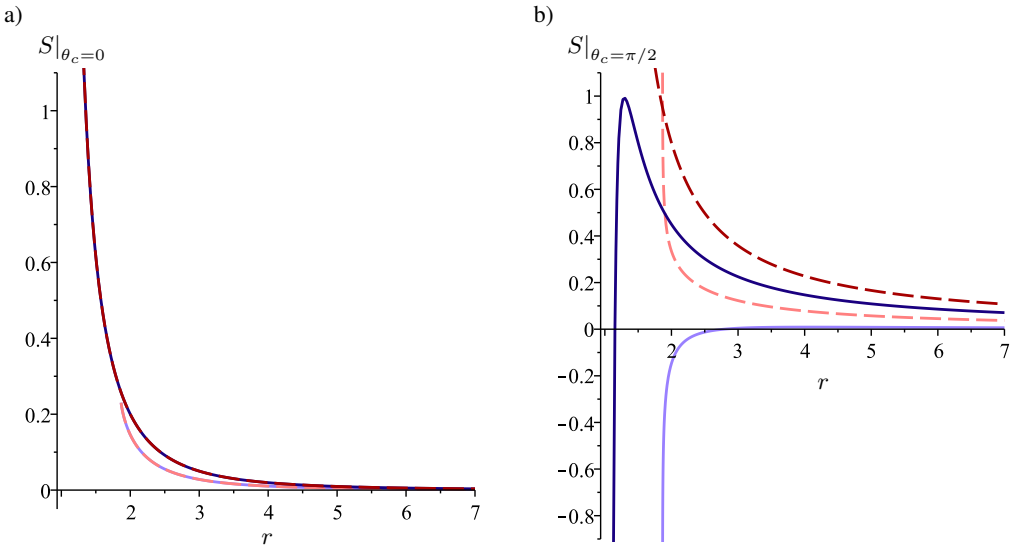

FIGURE 4.4: The potential $S|_{\theta=\theta_c}$ plotted along the radius for (a) $\theta_c = 0$ and (b) $\theta_c = \pi/2$. Light and dark red or blue lines correspond to $a = 1$ and $a = 0.5$ respectively. In (b) blue solid lines corresponds to $\omega = 0.04$, $a = 0.5$ (dark) and to $\omega = 0.21$, $a = 1$ (light). Red, dashed lines correspond to $\omega = 0.12$, $a = 0.5$ (dark) and to $\omega = 0.6$, $a = 1$ (light). While $S|_{\theta=0}$ is independent of ω and approaches for $a < 1$ a finite limit at the outer horizon, $S|_{\theta=\pi/2}$ diverges either to $+\infty$ or ∞ at the horizon, depending on the value of ω.

(a) and (b)). A repulsive force is needed in these areas to create a local maximum in r-direction. Vice versa is the case at the equatorial plane for radii bigger than the minimum location.

The electromagnetic force can be separated into an electric force term ($\sim f_{\mathcal{K}}(S)\partial_\mu A_t$) and a Lorentz force term ($\sim f_{\mathcal{K}}(S)\omega\partial_\mu A_\phi$), that contains ω. Both terms may independently result in an attractive or repulsive force along direction e_μ, which obviously depends on the choice of ω in case of the Lorentz force.

The behavior of S is shown in Fig. 4.4 at $\theta = 0$ and $\theta = \pi/2$. It approaches zero for big radii in both cases (see discussion in Sec. 2.2.2.1):

$$\lim_{r\to\infty} S|_{\theta=0,\pi/2} = 0\,.$$

On the equatorial plane S diverges to $\pm\infty$ at the outer horizon r_+, depending on the choice of ω:

$$\lim_{r\to r_+} S|_{\theta=\frac{\pi}{2}} = \begin{cases} -\infty,\ \omega < \frac{2ar_+(r_+-1)}{(a^2+r_+^2)^2-4a^2r_+} \\ +\infty,\ \omega > \frac{2ar_+(r_+-1)}{(a^2+r_+^2)^2-4a^2r_+} \end{cases}. \tag{4.22}$$

Along the symmetry axis S does not depend on ω, since $A_\phi|_{\theta=0} = 0$. At the outer horizon $S|_{\theta=0}$ does not diverge, but reaches the value

$$\lim_{r\to r_+} S|_{\theta=0} = \frac{3Ba}{4(\xi+\xi^2)}\,,$$

where $\xi = \sqrt{1-a^2}$.

In the following calculation of bound solutions for a charged fluid, $f_\mathcal{K}(S)$ is set to

$$f_\mathcal{K}(S) = k_f S^n\,. \tag{4.23}$$

Scaling factor k_f is correlated to the overall strength of the fluid charge and is determined according to Eq. (4.9) by $k_f \coloneqq b/S^n(r_c,\theta_c)$. Exponent n determines how strongly the charge distribution changes with S, which, in turn changes along the fluid structure. The choice of n is preferably picked from natural numbers ($n \in \mathbb{N}$), since S can become negative for some radii on the equatorial plane for certain ω.

4.4.1 Equatorial Tori

To discuss the location and structure of equatorial tori the procedure introduced in Sec. 4.2 is applied. Scaling factor k_f in Eq. (4.23) is determined by satisfying the necessary conditions (2.144) for a local maximum in h according to Eqs. (4.8) and (4.9). The range of possible ω a fluid tori with a center at $(r_c, \pi/2)$ can exhibit is determined by satisfying the sufficient conditions (4.12) - (4.13).

The discussion focuses on the influence of spin a and exponent n of the charge distribution function on the area of (r_c,ω), for which equatorial tori exist. Parameters n and a are the only parameters not yet determined by the model or the applied procedure, that have an influence on the structure of the effective potential. Magnetic dipole moment B and κ and Γ from the polytropic equation of state are still free to choose. Their choice is restricted by demanding that the torus' electromagnetic field is negligible compared to the background field.

The influence of spin a on the area of (r_c,ω), where equatorial tori are found, is presented in Fig. 4.5. Plotted are the areas where the first (4.12) or second (4.13) sufficient condition are satisfied. Condition $\mathcal{P} > 0$ (discussed before in Fig. 4.3) further restricts the area of solutions to solutions with subluminal motion. All conditions are satisfied at points from the white areas. A maximum exists for these points in the effective potential and an equatorial torus can be constructed. The value of k_f changes throughout the plot, since it is determined separately at each point to satisfy the first necessary condition

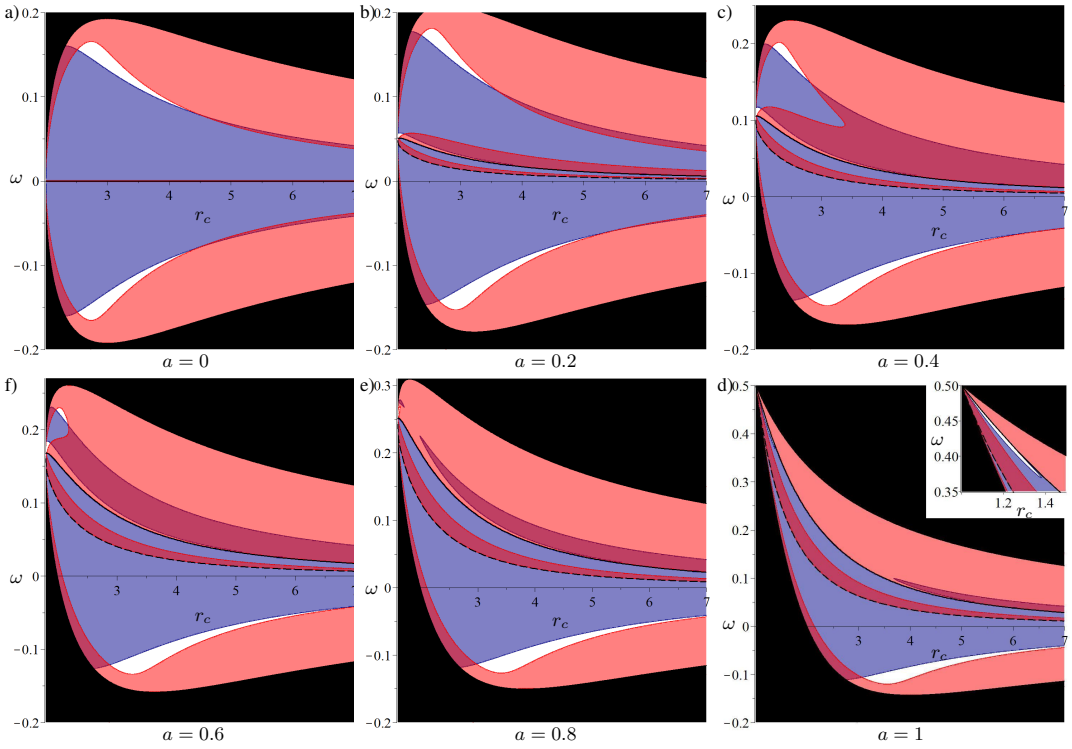

FIGURE 4.5: Map of the extremal points $(r_c, \theta_c = \pi/2)$ of effective potential h for $n = 2$ and different a. Scaling parameter k_f (Eq. (4.23)) is chosen such that the necessary conditions (2.144) are satisfied at each point in the plot and hence changes throughout the plot. The black region corresponds to $\mathcal{P} < 0$, where no solutions exist. Points in the white region correspond to local maxima of h, points in the light red region correspond to extremal points with a maximum in θ-direction only ($\partial_{rr} h > 0$), points in the blue area correspond to a maximum in r-direction only ($\partial_{\theta\theta} h > 0$). Points from the purple area describe local minima of h. $\partial_r S = 0$ and $S = 0$ are depicted as solid and dashed black lines respectively. They mark borders of the area, where extremal points have a maximum in r direction. $\partial_r S = 0$ marks further a border of the area with extremal points that have a maximum in θ direction. S and $\partial_r S$ appear in the denominators of sufficient conditions (4.11), which causes a sign flip at their roots.

in Eq. (2.144). The plot is symmetric with respect to the r-axis in the Schwarzschild limit ($a = 0$). Tori can be found for positive and negative values of ω rather close to the central object. For growing values of a the white area moves to smaller values of r_c in the co-rotating case and to bigger values of r_c counter-rotating case. The white area at $\omega > 0$ decreases in size for higher spins and nearly vanished for $a = 0.8$. For high spins, co-rotating solutions are found only very close to the outer horizon and for extremely high angular velocities ($\omega \approx 0.37 - 0.5$ for $a = 1$). Within the given set up counter-rotating tori seem to be favored in case of fast spinning central objects.

All points in the white areas lie in the range, where $\partial_r \mathcal{P} > 0$, and therefore a repulsive electromagnetic force on the fluid is needed stabilize the fluid to a bound structure (see discussion in Sec. 4.2). For $\omega < 0$ the electric and the Lorentz force term in Eq. (4.21) act in the same direction of r (see further discussion in Sec 2.2.2.1). These forces have

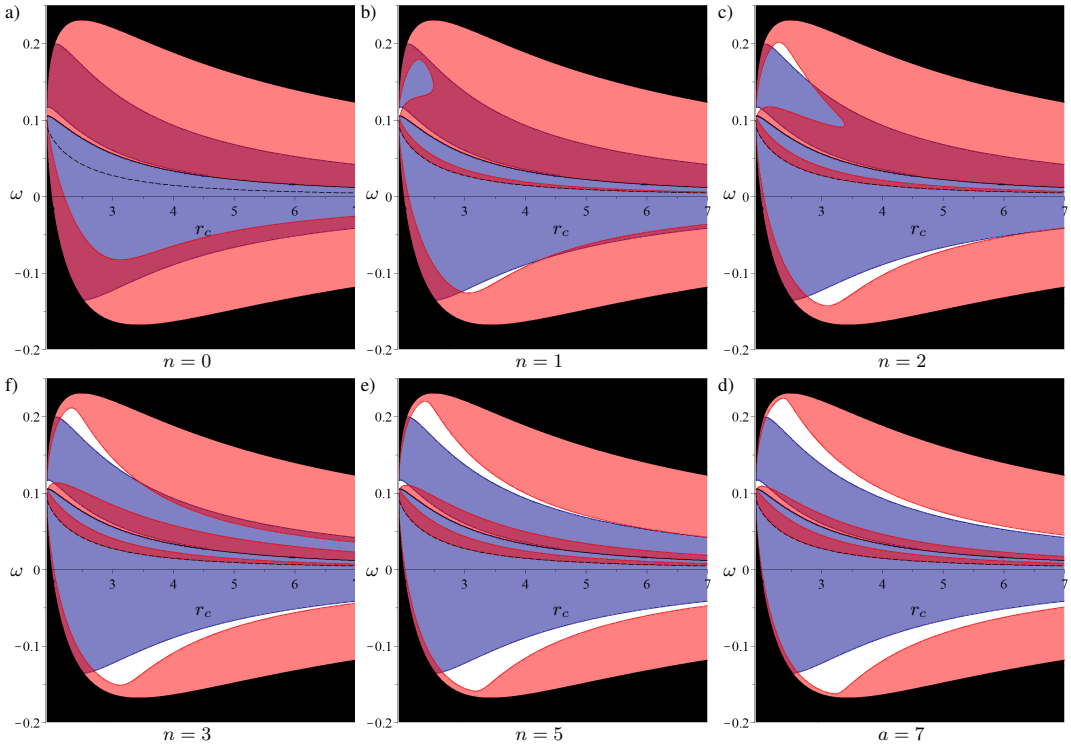

FIGURE 4.6: Map of the extremal points $(r_c, \theta_c = \pi/2)$ of effective potential h for $a = 0.4$ and different n. For a detailed description see Fig. (4.5). Higher values for n lead to a bigger white area, and therefore increase the parameter set of (r_c, ω), for which solutions for equatorial tori can be found.

to be repulsive for found solutions of equatorial tori. For $\omega > 0$, the electric and Lorentz force act in opposite directions of r. One of the two terms will dominate the divergence at $r = r_+$, and this depends, according to Eq. (4.22), on the value of ω. The dominating term leads to a repulsive force on the fluid for solutions of equatorial tori. However, the counteraction of the other force term becomes more influential for higher spins and causes a reduction of the white parameter area of tori solutions in Fig. 4.5 for co-rotating fluid tori at higher a.

In Fig. 4.6 the influence of exponent n in $f_\mathcal{K}(S) = k_f S^n$ on the area of (r_c, ω), where equatorial tori are found, is presented. The choice of n determines how strongly the charge distribution changes along the torus. Big values of n correspond to high changes in the charge density along the equatorial tori. As one can see in Fig. 4.6, bigger values of n increase the parameter area of (r_c, ω), for which equatorial tori exist. No solution can be found for $n = 0$ (see Fig. 4.6 (a) for $a = 0.4$), which corresponds to the simplest case of $f_\mathcal{K}(S) = const.$. The picture does not change for other spin values $0 \leq a \leq 1$.

Parameter n influences the area of possible solutions only by its contribution to the first sufficient condition (4.12), where it enters the expression at $\frac{f'_\mathcal{K}}{f_\mathcal{K}}(S) = n/S$. If the prefactor for n in Eq. (4.12) is negative – which is the case for $\partial_r \mathcal{P}\, \partial_r S/S < 0$

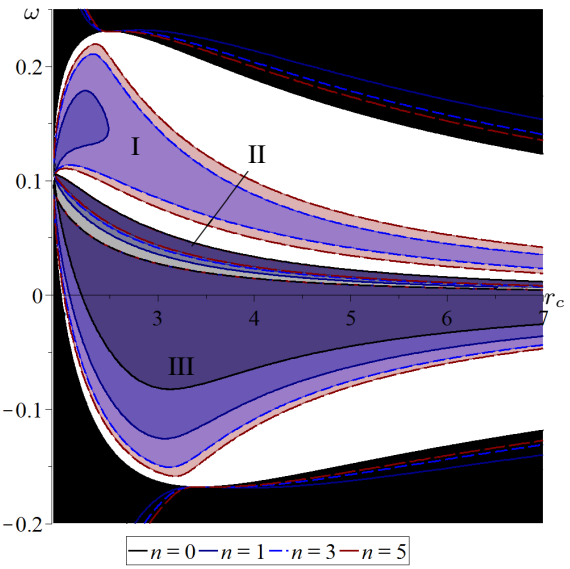

FIGURE 4.7: Map of the extremal points $(r_c, \theta_c = \pi/2)$ of effective potential h for $a = 0.4$ and different n. Scaling parameter k_f (Eq. (4.23)) is chosen such that necessary conditions (2.144) are satisfied at each point and hence changes throughout the plot. Points in the colored area between the curves correspond to a maximum in radial direction. Area I and II, of the three areas (I,II,III), where maxima in r can be found, grow for bigger n, while area II shrinks for bigger n. No solutions exist in the black area, where $\mathcal{P} < 1$.

– the area of (r_c, ω), where the first sufficient condition holds, increases for rising n. The development regarding n of the area, where the first sufficient condition holds, is depicted in Fig. 4.7. This area is also represented in Fig. 4.6 as a combination of the blue and white area. The prefactor of n $(\partial_r \mathcal{P}\, \partial_r S/S)$ is negative for points from regions I and III in Fig. 4.7. These regions therefore grow for an increasing n, whereas region II, where $\partial_r \mathcal{P}\, \partial_r S/S > 0$, shrinks.

Regions I and III contribute to the white areas in Fig. (4.6), where both sufficient conditions are satisfied. Higher changes in the charge distribution (indicated by bigger n) therefore lead to a bigger range of parameters (r_c, ω), for which solutions for equatorial tori exist.

Now that the parameter range is discussed, for which equatorial tori can in general be found, the focus turns to how a change in the spin of the central black hole or the angular velocity of the fluid effects the structure of the effective potential h. For this a family of solutions of the negative effective potential along the equatorial plane $(-h(r, \pi/2))$ is plotted for different a (Fig. 4.8 (a)) and different values of ω (Fig. 4.8 (b)), but otherwise fixed parameters n and $\mu_k := k_f(\omega B)^{n+1}$. The new parameter μ_k is fixed at this point instead of scaling parameter k_f to make a comparison with earlier related studies of bound charged structures [41, 42, 2] easier. The plotted curves of $-h(r, \pi/2)$ show the same structure as in the Schwarzschild case, discussed in [42].

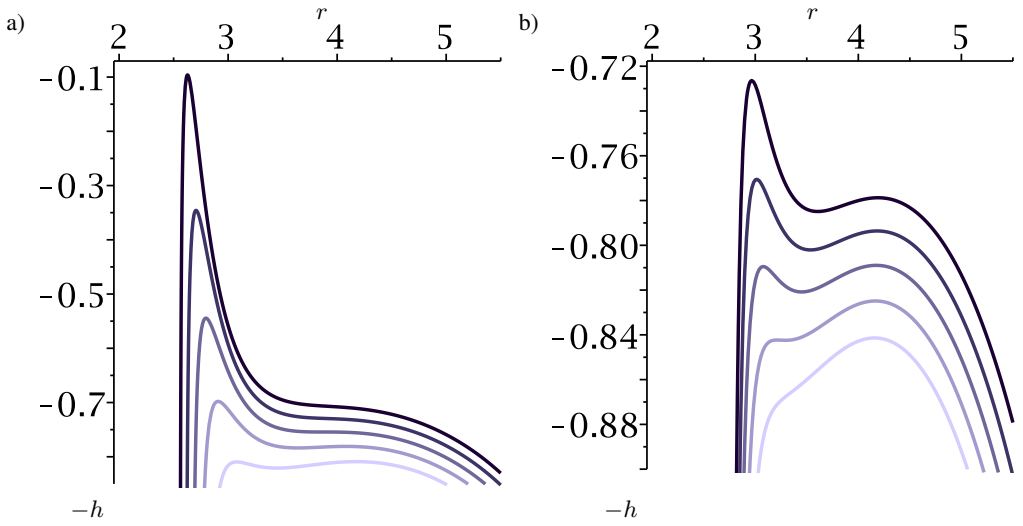

FIGURE 4.8: Negative effective potential $-h$ along the equatorial plane for $n = 2, \mu_k = k_f\,(\omega B)^{n+1} = -1.929$ and different values of (a) spinning parameter a and (b) angular velocity ω. In (a) $\omega = -0.1129$, and a runs from 0.7 (dark blue) to 1 (lightest blue) in steps of $\Delta a = 0.075$. In (b) $a = 1$ and ω runs from -0.1109 (dark blue) to -0.1149 (lightest blue) in steps of $\Delta\omega = -0.001$. Due to rigid rotation the area of r, where a fluid tori exist, shrinks with a growing value of $|\omega|$. The same behavior is found in (a) for a shrinking value of a. For bigger a and bigger $|\omega|$ ($\omega < 0$) the torus center moves to smaller radii.

Due to the assumption of rigid rotation the extrema of the curve $-h(r, \pi/2)$ move closer together for bigger absolute values of the angular velocity $|\omega|$, since the distance of the radii, where $\mathcal{P}$ becomes zero and the effective potential diverges, becomes smaller for bigger $|\omega|$ (see Fig. 4.8 (a)). The same effect appears for higher spins a (see Fig. 4.8 (b)) in case of negative ω. Intuitively this can be traced back to the frame dragging effect, due to which the same ω appears smaller in a LNRF in case of bigger a. The torus' center (depicted in Fig. 4.8 as a minimum in $-h$) shifts to a smaller radius for increasing values of a or ω. By decreasing the chosen a or ω for the given parameter set (n, μ_k, ω) or (n, μ_k, a) from $a = 1$ or $\omega = -0.1109$ a minimum and maximum in $-h(r, \pi/2)$ merge at one point and no bound solution exists anymore for the respective set of parameters and smaller values of a or ω.

The restriction of ω to $\omega > -0.1139$ for the given set of parameters is analogous to the lower limit ℓ_{ms} of the specific angular momentum ℓ in the uncharged Schwarzschild case, which was discussed in Sec. 2.5.4.

An analogue to the upper limit ℓ_{mb}, determined by the the marginally bound orbit, can be found in both plots (a) and (b) in Fig. 4.8 at the point, where the inner maximum of $-h$ takes a bigger value than the outer maximum. These points provide a lower limit for a and an upper limit for ω, beyond which no inner cusp can occur for a tori solution.

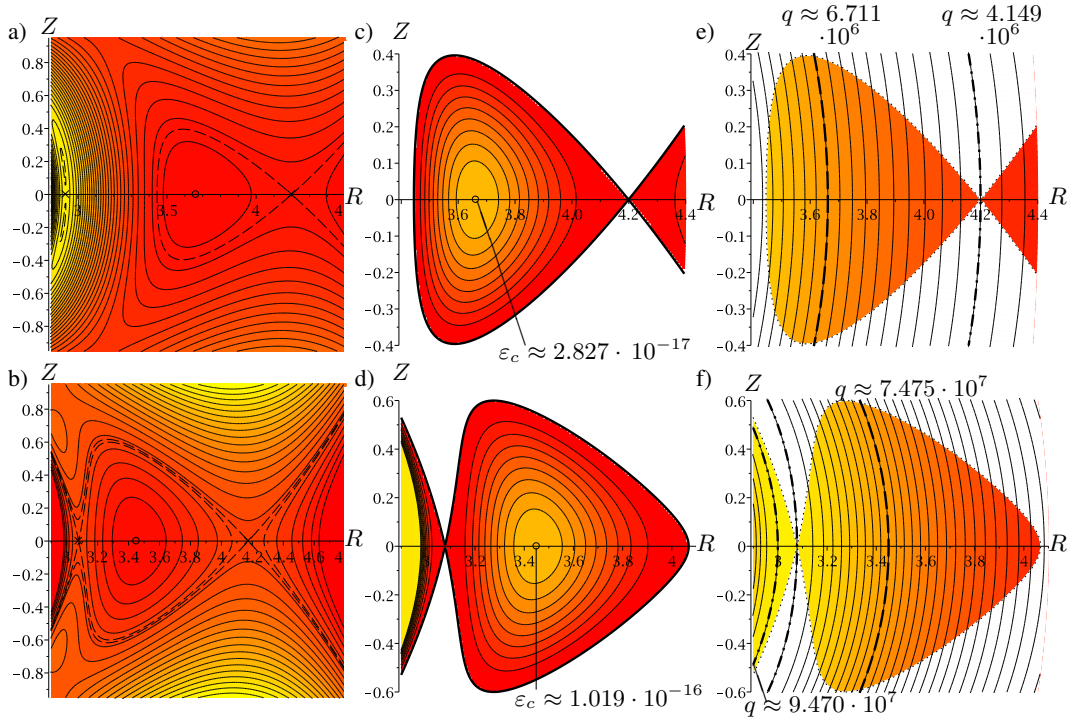

FIGURE 4.9: Two examples A (a,c,e) and B (b,d,f) of a charged equatorial torus with $n = 2$, $\mu_k = k\,(\omega B)^{n+1} = -1.929$ and $a = 1$. In example A (first row) $\omega = -0.11$, while in example B (second row) $\omega = -0.1129$. Presented is for both examples the effective potential as $-h$ in the first column (a,b), the energy density ε in the second column (c,d) and the specific charge distribution q in the third column (e,f). A red shade indicates smaller values, while a yellow shade indicates bigger values in all plots. The torus center is marked with a small circle in (a-d), where the energy density reaches its maximal value ε_c, it becomes zero at the edge of the torus. Equipotential curves of the cusp points are plotted as dashed lines in (a,b). Example A shows an outer cusp, allowing matter to outflow from the torus through the cusp away from the central object. The specific charge decreases towards bigger radii. Example B shows an inner cusp, allowing matter to outflow through the cusp onto the central object. The specific charge decreases towards bigger radii.

New introduced by the assumption of rigid rotation is the possibility for a tori solution to posses an outer cusp, from which material outflows away from the central object. These fluid tori are possible for parameter sets (n, μ_k, a, ω) depicted in Fig. 4.8, that lead to a $-h(r, \pi/2)$ with an outer maximum taking a smaller value than the inner one. According to Fig. 4.8, a slight change in ω or a can change the found fluid tori from one with an inner cusp to one with an outer cusp or a total vanish of the bound solution.

Finally two specific examples for equatorial tori are presented in Fig. 4.9 for a spin $a = 1$ of the central object. Depicted are for each example the negative effective potential $-h(r, \theta)$, the energy density and specific charge distribution of the fluid torus. The parameters (n, μ_k, a, ω), for which the examples are calculated, differ only in ω, analogous to $-h(r, \pi/2)$ plotted in Fig. 4.8 (b). In the first example with $\omega = -0.11$ an outer cusp is formed, while in the second example with a smaller angular velocity $\omega = -0.1129$ the

	Example 1	Example 2
$\mathcal{Q}$	$1.51 \cdot 10^{-9}$	$1.34 \cdot 10^{-}8$
$\mathcal{B}_{ET}$	$\sim -10^{-10}$	$\sim - \cdot 10^{-9}$
ε_c	$2.827 \cdot 10^{-17}$	$1.091 \cdot 10^{-16}$
p_c	$5.247 \cdot 10^{-20}$	$4.984 \cdot 10^{-19}$
q_c	$6.711 \cdot 10^{6}$	$7.457 \cdot 10^{7}$

TABLE 4.1: Physical characteristics total charge $\mathcal{Q}$, approximated magnetic field strength of the fluid $\mathcal{B}_{ET}$, central energy density ϵ_c, central pressure p_c and the specific charge at the center q_c of the two examples for an equatorial torus presented in Fig. 4.9.

found fluid structure exhibits an inner cusp. Both structures are located at rather small radii. Inner cusps on the equatorial plane can only occur for angular velocities ω for which one finds a local maximum at $r_{c,1}$ and an extremum at $r_{c,2} < r_{c,1}$, that exhibits a local maximum in θ- direction only. According to the discussion in Fig. 4.5 and 4.6, this is the case for ω, at which the white area is neighbored at smaller r_c by the bright red region. This combination occurs only for comparably big $|\omega|$ at rather small values of r_c. In both examples the charge distribution decreases towards bigger radii. The fluid is therefore more strongly charged closer to the central object.

The internal magnetic field created by the fluid torus has to be negligible compared to the background dipole field. To assure this, the polytropic coefficient κ is chosen sufficiently big. Bigger values for κ correspond to stronger diluted fluids and smaller pressures. On the other side, the choice of κ has no influence on the strength of the specific charge distribution (see Eqs. (4.2)-(4.4)). The magnetic field strength created by the fluid at the edge of the torus is estimated using the approximation given in Eq. (4.7). For the examples in Fig. 4.9 the remaining free parameters are set to

$$B = 4.2 \cdot 10^{-7}\,, \qquad \Gamma = \frac{5}{3}\,, \qquad \kappa = 2 \cdot 10^{8}\,. \tag{4.24}$$

The choice of B corresponds to a magnetic field strength of $B_{SI} = 10^8 T$ in SI units at the equatorial plane and $r = 3$, which is a typical field strength for a magnetar [7]. The chosen value of Γ corresponds to an adiabatic process in the non-relativistic limit. The value changes to $\Gamma = 4/3$ in the ultra-relativistic limit [74], however the specific choice of Γ is not critical for the overall discussion of the depicted examples. These choices lead to the physical characteristics (total charge $\mathcal{Q}$, approximated magnetic field strength of the fluid $\mathcal{B}_{ET}$, central energy density ϵ_c, central pressure p_c and the specific charge at the center q_c) given in table 4.1 for the two discussed examples. They were calculated using Eqs. (4.1)-(4.7). The approximated magnetic field strength $\mathcal{B}_{ET}$ of the torus is sufficiently small to be negligible compared to the background dipole field at the radii the torus is located.

	Example 1	Example 2
$\mathcal{Q}_{\mathrm{SI}}$ in As	$2.59 \cdot 10^{11}$	$2.30 \cdot 10^{12}$
$\rho_{m,c_{\mathrm{SI}}}$ in $\frac{\mathrm{kg}}{\mathrm{m}^3}$	$1.746 \cdot 10^{4}$	$6.739 \cdot 10^{4}$
$p_{c_{\mathrm{SI}}}$ in Pa	$2.913 \cdot 10^{18}$	$2.766 \cdot 10^{19}$
$q_{c_{\mathrm{SI}}}$ in $\frac{\mathrm{As}}{\mathrm{kg}}$	$5.783 \cdot 10^{-4}$	$6.426 \cdot 10^{-3}$

TABLE 4.2: Physical characteristics: total charge $\mathcal{Q}_{\mathrm{SI}}$, central mass density $\rho_{m,c_{\mathrm{SI}}}$, central pressure $p_{c_{\mathrm{SI}}}$ and the charge density per mass density at the center $q_{c_{\mathrm{SI}}}$ of the two examples for an equatorial torus presented in Fig. 4.9.

By roughly approximating the rest-mass density with the non-relativistic limit $\rho_m \approx \varepsilon$, the physical characteristics given in table 4.1 correspond to a total charge, central density, central pressure and charge density per mass density listed in table 4.2 for a compact object with one solar mass in SI-units. By comparing these values with the pressure and mass density of the sun core

$$p_{c(\mathrm{sun})} \sim 10^{16}\ \mathrm{Pa} \qquad\qquad \rho_{m,c_{(\mathrm{sun})}} \sim 10^{5}\,\frac{\mathrm{kg}}{\mathrm{m}^3}\,, \tag{4.25}$$

one can see, that the central pressure of both examples of an equatorial tori exceeds the the pressure of the sun core by far. At these pressures the negligence of radiation and the resulting additional radiation pressure and energy loss might not be a good approximation anymore. This can be avoided by assuming an even bigger value of κ, which leads to smaller central pressures and mass densities for the found structures.

4.4.2 Polar Clouds

In contrast to the discussion of charged fluid structures in the vicinity of a dipole magnetic field in Schwarzschild spacetime [42], solutions for polar clouds exist when considering a rotating central object. The rotation induces an electric field on the rotation axis, which is given by

$$E_t\big|_{\theta=0,\pi} = F_{rt}\big|_{\theta=0,\pi} = -\frac{3aB}{\xi^2(r^2+a^2)}\left((r^2-a^2)\frac{1}{2\xi}\ln\frac{r-1+\xi}{r-1-\xi} - r - a^2\right). \tag{4.26}$$

It provides the repulsive force, that is needed to stabilize the fluid to a bound structure and prevents it from falling onto the central object. All other components of the electromagnetic field tensor $F_{\mu\nu}$ (2.6) vanish for $\theta = 0, \pi$, since A_ϕ and its derivatives vanish on the polar axis. The polar clouds are symmetric with respect to the equatorial plane.

The discussion of polar clouds proceeds analogous to the one of the equatorial tori in the previous section. The existence and location of local maxima in h on the rotation axis is discussed like before for the parameter set (ω, n, a). Again, parameter k_f in Eq. (4.23)

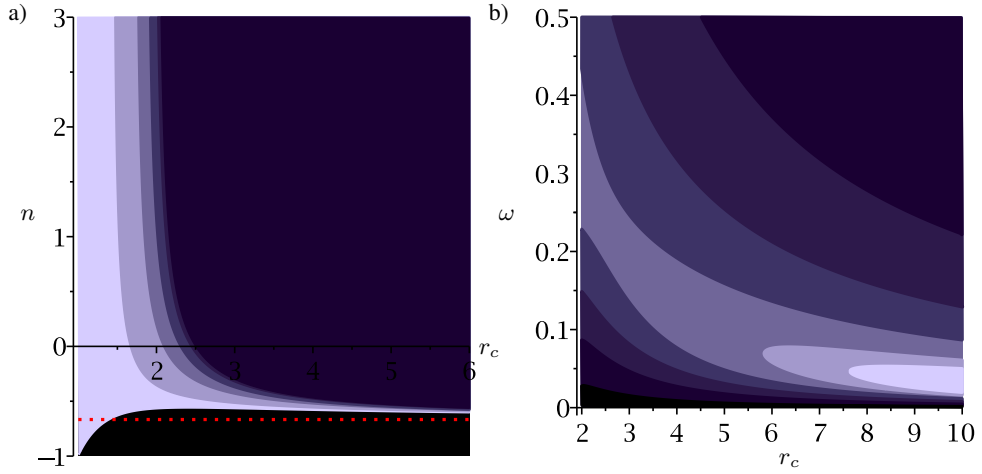

FIGURE 4.10: Map of the extremal points $(r_c, \theta_c = 0)$ of effective potential h for different values of a plotted over n (a) and ω (b). Scaling parameter k_f (Eq. (4.23)) is chosen such that necessary conditions (2.144) are satisfied at each point and hence changes throughout the plot. a) Points in the dark blue area satisfy the first sufficient condition of a local maximum in h (4.11) (which is independent of ω) for $a = 0.1$. The area grows for bigger values of a (indicated by lightening up the blue coloring) from $a = 0.3, 0.5, 0.7, 0.9$ to $a = 1$. The red line depicts a lower limit for n below which the first sufficient condition is not satisfied at $r_c \to \infty$. b) Pints in the dark blue area satisfy the second sufficient condition in (4.11) (which is independent of n) for $a = 1$. The area grows for smaller a from $a = 0.9, 0.7, 0.5, 0.3$ to $a = 0.1$, indicated by lightening up the blue coloring. For large a, there is a minimal r_c for which the second sufficient condition is satisfied.

is determined by satisfying the fist necessary condition (2.144) for local maxima in h. The range of r_c, for which the two sufficient conditions (4.12)-(4.13) can be satisfied, is depicted in Fig. 4.10, depending on the parameter set (ω, n, a). The first sufficient condition is independent of ω, while the second one is independent of exponent n for $\theta_c = 0$. It is therefore more descriptive to plot the ranges for which the sufficient conditions are satisfied, in separate plots – the first sufficient condition for (r_c, n) in Fig. 4.10 (a) and the second one for (r_c, ω) in Fig. 4.10 (b).

Both sufficient conditions can always be satisfied for sufficiently big values of r_c, and therefore solutions for polar clouds always exist with a center at large radii. The range of r_c for which the fist sufficient condition is satisfied grows with higher spins, while on the other hand the range for which the second sufficient condition is satisfied shrinks with higher spins. For all spins $0 < a \leq 1$ a lower limit occurs for r_c, below which no polar cloud solution exists, either because the first or the second sufficient condition cannot be satisfied. Even though solutions for polar clouds can be found at arbitrarily large r_c and for arbitrarily small a a very strongly charged fluid is required in these cases, since parameter k_f diverges for $\partial_r S \to 0$, which is reached for $r_c \to \infty$ or $a \to 0$ (see Eqs. (4.9) and (4.23)).

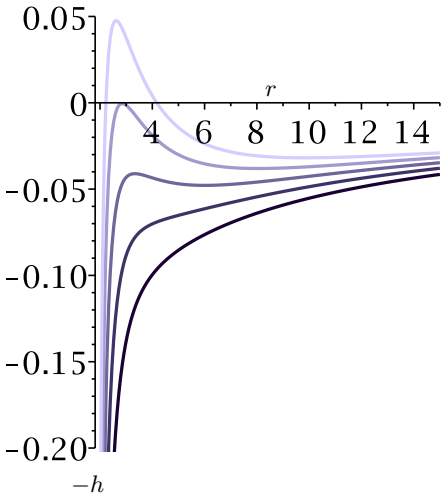

FIGURE 4.11: Negative effective potential $-h$ along the equatorial plane for $n = -1/2, \mu_k = k\,(\omega B)^{n+1} = -0.596$ and different values of a. The effective potential is independent of ω along the rotational axis. Spinning parameter a runs from 0.2 (dark blue) to 0.4 (lightest blue) in steps of $\Delta a = 0.05$. For bigger a $-h$ develops a minimum, which is necessary for a bound solution. The clouds center moves to bigger radii.

In the limit $r_c \to \infty$ solutions exist only for $n > -2/3$, which is depicted as a red dotted line in Fig. 4.10 (a). For most spins a this is also a general lower limit for n, below which no polar cloud solutions are possible. The lower limit for n diverges in these cases to $+\infty$ for $r_c \to r_+$. For spin values very close to the extreme case $a = 1$ (e.g. $a > 0.99$) the first sufficient condition can also be satisfied for $n < -2/3$ close to r_+. In the extreme case $a = 1$ the condition is satisfied for $n > -1$ at $r_c = r_+$. However, no polar cloud solutions with $n < -2/3$ can be found, since the second sufficient condition is not satisfied close to r_+ for a spin close to one.

According to the plot for the second sufficient condition polar cloud solutions can only be found for co-rotating clouds for any spin $0 < a \leq 1$ of the central object. An attractive force towards the rotation axis, produced by the Lorentz-force on the rotating charged fluid ($f_{\mathcal{K}}(S)\partial_\theta S < 0$ at some area $0 < \theta < \Delta\theta$), is necessary to find a local maximum of h at the poles. A local maximum further requires a repulsive force in r-direction, which is created on the polar axis solely by an interaction of the charged fluid with the electric field (4.26), which arises from $A_t \neq 0$. All other components of the electromagnetic field vanish. This requirement determines the torus' charge ($f_{\mathcal{K}}(S)\partial_r A_t\big|_{\theta=0,\pi} > 0$). Since $\partial_r A_t(r, \theta = 0) < 0$, $f_{\mathcal{K}}(S)$ has to be negative on the polar axis as well as in some area $0 < \theta < \beta$, for which $S(r, \theta)$ does not change its sign. An attractive force can now only be achieved close to the polar axis, if $\partial_\theta S = \partial_\theta A_t + \omega\partial_\theta A_\phi > 0$. Since $\partial_\theta A_t < 0$ and $\partial_\theta A_\phi > 0$ for $0 < \theta < \pi/2$ and $r > r_+$, this condition can only be satisfied in the co-rotating case $\omega > 0$. This result coincides with the one found in [2] for a homogeneous magnetic test-field and a central object without a net charge ($e = 0$ in their notation).

	polar cloud
$\mathcal{Q}$	$3.099 \cdot 10^{-8}$
$\mathcal{B}_{PC}$	$\sim 10^{-10}$
ε_c	$5.007 \cdot 10^{-17}$
p_c	$1.360 \cdot 10^{-19}$
q_c	$-1.730 \cdot 10^{7}$

TABLE 4.3: Physical characteristics total charge $\mathcal{Q}$, approximated magnetic field strength of the fluid $\mathcal{B}_{PC}$, central energy density ϵ_c, central pressure p_c and the specific charge at the center q_c of the polar cloud presented in Fig. 4.12.

Since the fluid velocity approaches zero right on the rotation axis, no restriction is given by $\mathcal{P} > 0$ on the range of possible values for r_c.

The focus turns now to how a change in the spin of the central object effects the structure of the effective potential h. A family of solutions of the negative effective potential along the rotation axis ($-h(r,0)$) is plotted for different spins a but otherwise fixed parameters n and μ_k in Fig. 4.11. The repulsive effect on the fluid by the electric field (4.26) grows for higher spins a, since the field is evoked by the frame dragging. This correlation manifests in the plot as a growth of the maximum in $-h(r,0)$ for rising a. Bigger spins further shift the torus center (depicted in Fig. 4.11 as a minimum in $-h$) towards bigger radii. The negative effective potential $-h(r,0)$ shown in Fig. 4.11 has the same structure as the one for an uncharged fluid torus in Schwarzschild spacetime with a constant angular momentum ℓ, which was discussed in Sec. 2.5.4. Analogous to the lower $\ell_{(ms)}$ and upper limit $\ell_{(mb)}$ for ℓ a lower limit is found for a, below which now polar cloud solution exists as well as an upper limit, above which polar cloud solutions cannot develop an inner cusp point through which matter could be accreted by the central object. Solutions with an outer cusp on the rotation axis cannot exist, since the effective potential $h(r, \theta = 0, \pi)$ approaches zero for $r \to \infty$ and cannot have a third extremum. However, outflows away from the central object might still occur at cusp points located at $\theta \neq 0$.

	polar cloud
$\mathcal{Q}_{\mathrm{SI}}$ in As	$5.31 \cdot 10^{12}$
$\rho_{m,c_{\mathrm{SI}}}$ in $\frac{\mathrm{kg}}{\mathrm{m}^3}$	$3.093 \cdot 10^{4}$
$p_{c_{\mathrm{SI}}}$ in Pa	$7.552 \cdot 10^{18}$
$q_{c_{\mathrm{SI}}}$ in $\frac{\mathrm{As}}{\mathrm{kg}}$	$-1.491 \cdot 10^{-3}$

TABLE 4.4: Physical characteristics: total charge $\mathcal{Q}_{\mathrm{SI}}$, central mass density $\rho_{m,c_{\mathrm{SI}}}$, central pressure $p_{c_{\mathrm{SI}}}$ and the charge density per mass density at the center $q_{c_{\mathrm{SI}}}$ of the polar cloud presented in Fig. 4.9.

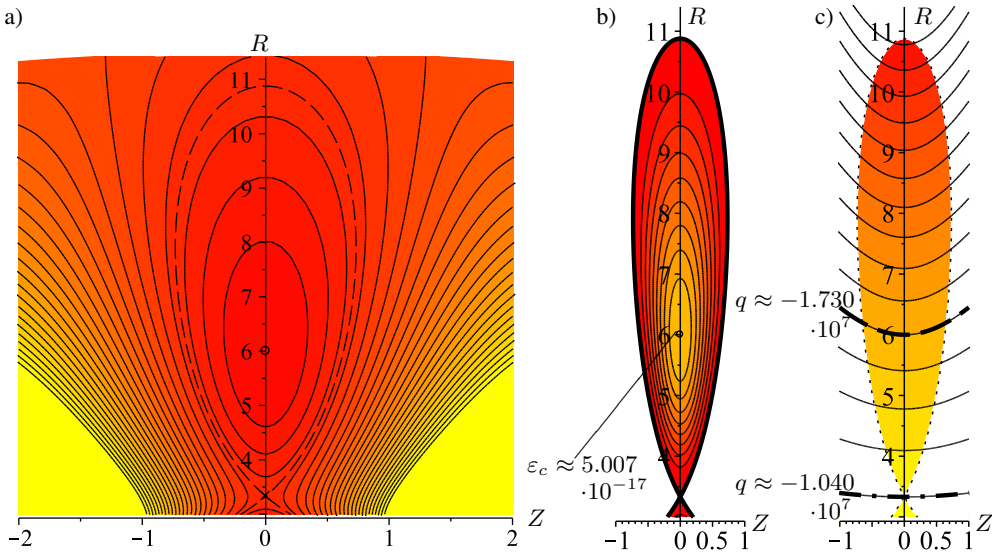

FIGURE 4.12: Example of a charged polar cloud with $n = -0.5$, $\mu_k = k\,(\omega B)^{n+1} = -0.596$, $a = 0.3$ and $\omega = 0.1$. Presented is the effective potential as $-h$ in (a), the energy density ε in (b) and the specific charge distribution q in (c). A red shade indicates smaller values, while a yellow shade indicates bigger values in all plots. The torus center is marked with a small circle in (a) and (b), where the energy density reaches its maximal value ε_c. It becomes zero at the edge of the torus. The equipotential curve of the cusp is plotted as a dashed line in (a). The depicted solution shows an inner cusp, allowing matter to outflow through the cusp onto the central object. The absolute value of the specific charge $|q|$ decreases towards bigger radii.

An example for a polar cloud is presented in Fig. 4.12 for $n = -0.5$, $\mu \approx -0.596$, $\omega = 0.1$ and $a = 0.3$ with its center at $r_c = 6$. The parameters of the polytropic equation (κ, Γ) and B are are set as given in Eq. (4.24), which leads to the physical characteristics of the polar cloud as given in table 4.3. In contrast to the charge distribution for the found equatorial tori, the absolute value of the specific charge distribution $|q|$ increases towards bigger radii in the depicted example of a polar cloud.

The total charge, central density, central pressure and charge density per mass density in SI units, that correspond to the physical characteristics listed in table 4.3, is calculated for a compact object with one solar mass in table 4.4. The central pressure of the polar cloud exceeds the pressure of the sun core for the assumed values of the polytropic coefficient and exponent κ and Γ like the examples for an equatorial tori. Again this could be avoided, by assuming a bigger κ.

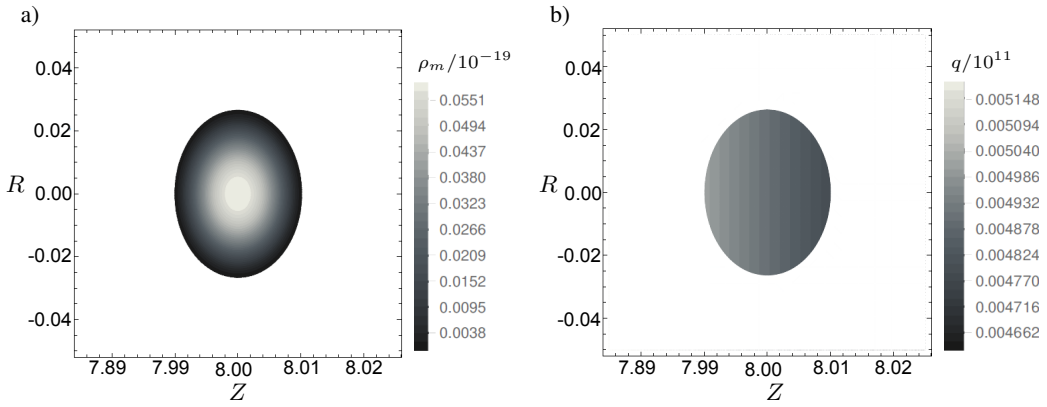

FIGURE 4.13: Example for (a) the mass density ρ_m and (b) specific charge distribution q of an equatorial tori around a charged ($Q/H = -1/8.78$), spinning ($a = 0.9$) compact object in a uniform magnetic field. The tori rotates with an angular velocity $\omega = 0.001$. Mass density and specific charge distribution are calculated for the parameters $\Gamma = 5/3$ and $\kappa = 10^8$ of a polytropic equation of state. Picture taken from Trova et al. [2].

4.5 Charged Fluid Structures around a Charged, Rotating Compact Object in a Uniform Magnetic Field

This chapter serves to summarize the discussion of charged fluid structures around a charged, spinning compact object, that is located in a uniform magnetic background field [2]. The set up is a generalization of the scenario discussed by [41] for a non-rotating central object. Comparisons are drawn to the results from the discussion in the previous section, where a magnetic dipole field and no net charge of the compact object was considered instead.

The Kerr metric is used to describe the central compact object, like in the previous example. To maintain the needed symmetries, the considered uniform magnetic field has to be oriented parallel to the rotational axis of the central object. The electromagnetic field, caused by the object's net charge and uniform magnetic background field, is described by the corresponding test field in Kerr spacetime, given by Wald [45], Stuchlík and Kološ [102]:

$$A_t^{(uniform)} = \frac{H}{2}\left(g_{t\phi} + 2ag_{tt} - \frac{Q}{H}(g_{tt}+1)\right), \tag{4.27}$$

$$A_\phi^{(uniform)} = \frac{H}{2}\left(g_{\phi\phi} + 2ag_{t\phi} - \frac{Q}{H}g_{t\phi}\right), \tag{4.28}$$

where H is the field strength of the uniform magnetic field, and $g_{\mu\nu}$ are the metric coefficients of Kerr spacetime. A polytropic equation of state (4.1) is considered for the charged fluid. Since the electromagnetic potential contains a t- and ϕ-component it is again necessary to assume rigid rotation for the charged fluid. The uniform magnetic

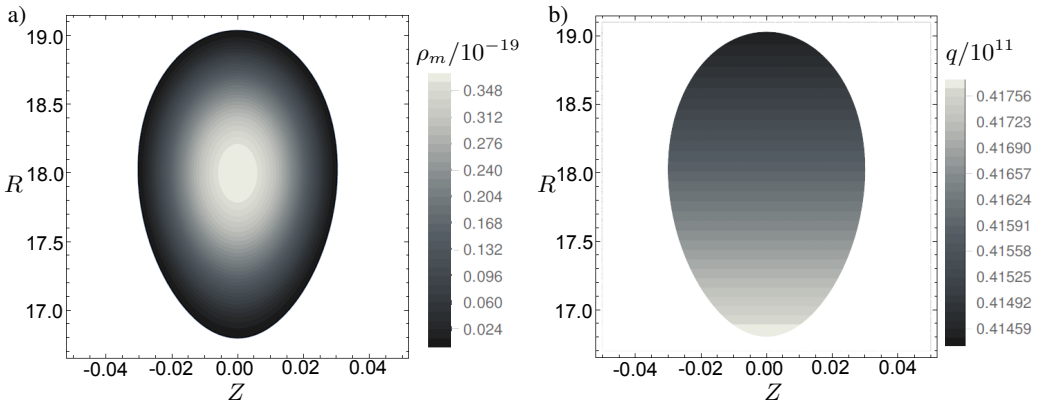

FIGURE 4.14: Example for (a) the mass density ρ_m and (b) specific charge distribution q of a polar cloud of a charged ($Q/H = 4.17$), spinning ($a = 0.9$) compact object in a uniform magnetic field. The cloud rotates with an angular velocity $\omega = 0.001$. Mass density and specific charge distribution are calculated for the parameters $\Gamma = 5/3$ and $\kappa = 10^6$ of a polytropic equation of state. Picture taken from Trova et al. [2].

background field is caused by distant sources and assumed to have a strength of $H \sim 10^{-11}$, which corresponds to $H_{SI} \sim 10^6$ T.

In the search for equatorial tori a charge distribution function

$$f_{\mathcal{K}}(S) \propto S^{-2} \tag{4.29}$$

was assumed. The discussion focused on a fixed ratio of $Q/H = -1/8.78$ in order to compare the results with the results in [41]. However, according to Wald [45], a black hole in a uniform magnetic field tends to charge up to a ratio $Q/H = 2a$. For $Q/H = -1/8.78$ co-rotating tori are preferred over counter-rotating tori for higher spins of the central object. The solutions for counter-rotating tori actually vanish for higher values of the spin ($a \gtrsim 0.5$). This behavior is complementary to the one observed in case of a dipole magnetic background field. The cause does not necessarily be the different shapes of the considered magnetic fields, but could also be traced back to the additional field from the electric net charge of the compact object. An example for an equatorial tori and its charge distribution is presented in Fig. 4.13 for $a = 0.9$ and $Q/H = -1/8.78$. Integration constant h_0 (see Eq. (2.142)) is chosen such, that a very thin equatorial tori is formed, compared to the examples presented in Fig. 4.9. The solution is compared in [2] to the one derived for a very small spin ($a = 0.01$). It was constructed very thin in order to keep its electric self-field negligible compared to the electric background field for a polytropic constant $\kappa = 10^8$.

Polar clouds were searched for a charge distribution

$$f_{\mathcal{K}}(S) \propto S\,. \tag{4.30}$$

In contrast to the case of a non-rotating compact object, polar clouds are found for both limiting cases (i) $H \neq 0$, $Q = 0$ and (ii) $H = 0$, $Q \neq 0$. The effect of frame dragging enables the existence of polar clouds by evoking electric or magnetic components in an originally purely magnetic or electric field. Only co-rotating polar clouds can be found in the limiting case (i). The same result was found in the previously discussed scenario of a magnetic dipole field. The restriction to co-rotating clouds is removed, when an electric net charge of the compact object is additionally considered. For a ratio of $Q/B = 4.17$ counter-rotating polar clouds are favored. An example for a polar cloud and its charge distribution is presented in Fig. 4.14 for $a = 0.9$ and $Q/B = 4.17$. Again, a small fluid structure is presented, compared to the example shown in Fig. 4.12. The electric self-field of this small structure is sufficiently small to be negligible compared to the electric background field, even for a polytropic constant $\kappa = 10^6$.

Chapter 5

Summary and Conclusion

In two different scenarios the issue of how the presence of charge can influence the accretion process onto a spinning central object was approached mainly analytically.

In the first scenario the center of discussion was the effect of a realistic black hole net charge of the order $Q \sim 10^{-18} - 10^{-21}$ on the accretion process of hydrogen plasma. The test-particle approach was used to describe the motion of the plasma particles when accreted by an electrically charged and spinning black hole, as described by the Kerr-Newman spacetime. A number of physical effects are neglected in this approach, that are usually present in accretion processes caused by short and long range particle interactions. This allows to focus on relativistic effects and the influence of the black hole net charge. Within the applied model, big net charges of $Q \sim 1$ lead to a plasma particle motion, that deviates only slightly from a radial infall due to the frame dragging effect of a spinning black hole. Even though the influence of a realistic net charge is unimportant in terms of spacetime curvature, a discussion of the ISCO of charged particles in Kerr-Newman spacetime revealed, that its location is very sensitive to a change of the black hole net charge within the realistic range. Up to four different values for the ISCO are found for charged particles for a given black hole spin and net charge. They are connected to the four combination possibilities of a same or opposite charged particle and black hole and a direct or retrogate particle orbit. Moreover, the ISCO is used to determine the inner edge of the accretion disc at the equatorial plane. The accretion process was discussed by analyzing the effect of the available parameters on the streamlines, velocity field, density field and on the outer and inner edges of the forming accretion disc. The black hole spin a has a rather small effect on the accretion process and the disc edges, but the frame dragging effect, which was already discussed in [82], was recovered. Two density peaks arise in the accretion process at the equatorial plane, created by the two different particle types of hydrogen plasma. Their position is influenced by all

parameters of the model, especially by the initial velocities of the plasma particles and the net charge of the black hole, which affects predominantly the peak distance. The effect of the black hole net charge on the plasma course in the accretion process becomes stronger, the slower the initial radial infall and the higher the initial angular velocity of the plasma. The negligence of the electromagnetic field created by the plasma in the used model strongly restricts its applicability to rather small initial plasma particle densities of $10 - 10^{-2}\,\mathrm{cm}^{-3}$, especially due to the arising density peaks at the equatorial plane. These densities are typical for interstellar to interplanetary plasmas.

Four different accretion disc scenarios are possible according to the applied plasma accretion model, which are caused by the possibility, that the biggest radius at which one particle type hits the equatorial plane might be smaller than the radius of the corresponding ISCO. All accreted particles will have to spiral into the black hole in the first case. Only one particle type contributes to the accretion disc in the second and fourth case, so that the disc will slowly develop a charge. At one point the arising electromagnetic field of the disc cannot be neglected anymore and the model's description breaks down. The majority of both particle types contributes to the accretion disc in the third case. An inhomogeneous charge distribution is formed, where particles with a charge attracted by the black hole are located in the inner area of the disc, closer to the black hole. This distribution might be washed out due to the particle interactions within the accretion disc. Otherwise the description of the model breaks down at the point where the electromagnetic field created by the accretion disc cannot be neglected anymore.

In the second scenario the focus lay on geometrically thick accretion discs with a non-neutral charge distribution, and how charge distribution and the spin of the central object effect the structure and existence of such accretion discs, while they are located in the vicinity of electromagnetic background fields. The charged, accreted matter was described in the fluid approach, while the Polish Donut model was applied to search for bound fluid structures around the central object. The model considers stationary and axially symmetric spacetimes in which the fluid moves on circular orbits. The considered electromagnetic background field was treated as a test field, that must also exhibit stationarity and axial symmetry. Compared to the electromagnetic background field the field created by the fluid was assumed to be negligible. The fluid was further described by a polytropic equation of state. A condition for the conduction current was found, that ensures the self-consistency of the model. Otherwise the overall conduction of the charged fluid must be assumed to vanish. To satisfy the integrability condition arising from the resulting pressure equations, a condition on the structure of the charge distribution was formulated. It restricts the charge distribution to be determined by a function of the electromagnetic potential of the background field. Furthermore rigid

rotation of the fluid has to be assumed, if the electromagnetic potential contains both an electric and a magnetic component. After assuming reflection symmetry with respect to the equatorial plane for the whole setup, a procedure was introduced, with which bound fluid structures can be constructed, that have their center either in the equatorial plane (equatorial tori) or along the axis of symmetry (polar clouds) for any spacetime and background field that satisfy the symmetry conditions.

The second part of the discussion focused on the explicit scenario of a Kerr spacetime with a dipole magnetic background field, which is a direct generalization of the Schwarzschild case discussed in [42]. The setup mimics a compact, spinning object with a dipole magnetic field, that is aligned with the rotation axis (e.g. a compact, spinning neutron star, that produces a magnetic dipole field aligned with its rotation axis). The behavior of the electromagnetic potential of the dipole was discussed. This was necessary to understand the later results on the parameter range, for which bound fluid structures exist. The existence conditions for equatorial tori and polar clouds were studied in detail. In the uncharged limit, where either the fluid is neutral, or no electromagnetic background field exists, neither equatorial tori, nor polar clouds exist for a rigidly rotating fluid. In the general case the spin of the central object has a major impact on the region in parameter space, where bound fluid structures are found. This could be traced back to the interplay of the electromagnetic test field and frame dragging, which induces an electric component to the electromagnetic field, that describes the magnetic dipole on Kerr spacetime. It causes a preference for counter-rotating equatorial tori for rising spins of the central object. Polar clouds do not exist in the non-rotating case, since the effects of the magnetic field vanish along the symmetry axis. In the rotating case the induced electric field balances the gravitational attraction for the right charging of the fluid, and polar cloud solutions are found. In both cases of counter-rotating equatorial tori, and of polar clouds the center of solutions are found further away from the central object the faster the object rotates. The structure of the charge distribution within the fluid is described by a power law and was varied by changing its exponent n. It determines how fast the charge density changes throughout the torus. Higher values of n broaden the range of angular velocities ω and radii of the torus center r_c for which polar clouds or equatorial tori are found. Furthermore fluid structures, which allow an outflow towards or away from the central object were discussed, encoded by the existence of an inner or outer cusp in the effective potential, respectively. A slight variation in the used set of parameters (like the angular velocity of the fluid or the spin of the central object) can turn an equatorial tori with an inner cusp to one with an outer one. No outer cusps occur in the solutions of polar clouds. Examples were presented, that show an inner or outer cusp and only have a slight variation in the parameter set.

The polytropic coefficient of the fluid was chosen such that the fluid density is small enough, so that the electromagnetic field of the found fluid structure is negligible. Big values of the polytropic coefficient connect higher pressures to the same fluid density. In the discussed examples it was chosen such, that central densities of about $\rho_{m,c\mathrm{SI}} \sim 10^4 \frac{\mathrm{kg}}{\mathrm{m}^3}$ occur, ten times denser than water, while the calculated pressure $p_{c\mathrm{SI}} \sim 10^{18} \frac{\mathrm{kg}}{\mathrm{m}^3}$ exceeds the pressure at the core of the sun by far. At these pressures the negligence of radiation and the resulting additional radiation pressure and energy loss might not be a good approximation anymore. However this can be avoided by choosing even bigger values for the polytropic coefficient.

Because of their simplicity, analytical models have their limits. They describe very idealized scenarios, that will hardly be met in reality. Nevertheless, the analytical treatment of these two scenarios of charged accretion processes allows to draw the following conclusions. Realistic electric net charges of black holes can have a non-negligible effect on plasma accretion, due to electromagnetic interactions of black hole and plasma, which deviates the course of electrons from the ion's. In combination with the strong effect on the existence and location of the ISCO, this further points to an influence on the shape of the accretion disc. The results motivate to look for observable effects of a black hole charge on the emitted spectrum, like it was done very recently by Zajaček et al. [48]. Electromagnetic interactions of geometrically thick accretion discs with external fields open new possibilities to stabilize the fluid from gravitational attractions. These possibilities widen, when frame dragging effects mix the magnetic and electric components of the external field. It leads to the existence of rigidly rotating, charged polar clouds, the preference of one rotational direction of the disc, or geometrically thick discs with outer cusps. Next to the angular momentum distribution in the thick disc, its charge distribution will also effect the disc structure.

Chapter 6

Outlook: Arising Questions and the Next Steps

The discussion of charged fluid structures around spinning compact objects is everything but finished. The very next steps that come to mind are the following.

1. So called off-equatorial tori exist, when charged fluids with constant angular momentum distributions are considered in Schwarzschild spacetime. Can comparable structures be found in case of a charged fluid in rigid rotation, when considering Kerr spacetime?

2. The remaining choice for the charge distribution opens the question, if the distribution can generally be chosen such that the total charge of the fluid structures vanishes. If that was the case, the accreted matter could originally have been quasi-neutral, but a charge distribution was evoked during the accretion process and the formation of the disc in the vicinity of an electromagnetic background field.

3. Different choices in the angular momentum distribution lead to very different structures of the corresponding disc solutions (see [30, 31]). Is it possible to achieve a comparable result, with suitable choices for the charge distribution? Since this work focused mainly on the existence of bound solutions, and whether these solutions posses an inner or outer cusp point, this question is still left to be answered.

4. The extended Polish Doughnut model of charged fluids in electromagnetic background fields can also be applied to more complex, but also more realistic spacetimes and electromagnetic test fields. A quadrupole term or even higher terms of the electromagnetic field can be considered, as well as more realistic spacetimes, which are more suitable to describe neutron stars.

A very important subsequent subject is the stability discussion the charged, thick accretion discs. Stability discussions of uncharged tori pointed to non-constant angular momentum distributions in the tours. Further stability discussions could lead to the preference of certain charge distributions in the charged structures. One major issue is the assumption of a non-conducting fluid. Plasmas usually display high conductivities, which motivates the assumption of infinite conductivity in ideal MHD. However the charged, thick disc model is also applicable, if the conduction current is restricted to a certain direction (see Sec. 2.5.1). In case of a purely magnetic field, the conduction current should be parallel to the magnetic field lines. This orientation is actually expected to be naturally formed by Henriksen and Rayburn [90] in pulsar magnetospheres due to a high resistivity transverse to the magnetic field. The stability of the found charged fluid structures should therefore also be checked regarding small deviations of the conduction current from the direction it is restricted to in the charged, thick disc model.

The Polish Donut model, complemented with Komissarov's toroidal magnetic field, was adapted by Vincent et al. [36] to calculate emission spectra e.g. of Sgr A*. A nice application of the extended Polish Doughnut model – leading to results that can be compared to observation – would be to use it for calculating the emission spectra in the presence of strong magnetic background fields. However one needs to clarify first, how the external magnetic field might effect the process which leads to synchrotron radiation.

In a long-term goal one can strive to consider electromagnetic and gravitational self-fields of the accreted material as well as viscous effects in the presented analytic models. First steps in the implementation of gravitational self-fields to the extended Polish Donut model were already undertaken by Trova et al. [103]. In general self-gravitational effects have been intensely studied numerically and analytically in the last decades [104]. Other than stabilizing effects in terms of geometrically thick accretion discs [105], it also causes so called gravitational instabilities, that lead to a redistribution of angular momentum in accretion discs. The existence of gravitational instabilities is therefore supposed to fasten the actual process of accretion. It can also lead to a defragmentation of the accretion disc. Clumps of matter form, out of which stars (in case of an AGN) or planets (in case of protoplanetary discs) are supposed to emerge eventually. The correct treatment of viscosity is another big issue. Up until now it still remains unresolved to find a fundamental, GR description of viscosity for accretion processes, that goes beyond the extremely simplified, ad-hoc α-prescription. This description is absolutely necessary, since there is no verification, that the α-prescription of viscosity is a good approximation in strong gravity close to the accreting compact object. The presence of viscous effects plays an important role in the fragmentation processes caused by self-gravitational effects, since its strength can enforce or suppress the process. An accurate

description of viscosity and the consideration of internal and external electromagnetic fields in a GR framework could lead to new results regarding the overall structure of thick accretion discs, fragmentation processes and the efficiency of angular momentum transport, which is essential for the efficiency of an accretion process.

The final proposal for a follow-up work is motivated out of theoretical interest, but its actual astrophysical realization is quite visionary. It covers the consideration of central objects with magnetic monopoles in accretion processes. The interaction of electrically charged particles with the monopole field breaks the reflection symmetry with respect to the equatorial plane. As a result, an accretion disc would not form in a declared plane. Its location, if it does form, is unclear. While the test-particle approach of plasma accretion, as discussed in Sec. 3, is suited to clarify a possible position of the disc, the Polish Donut model could give hints on its geometrical structure. Magnetic monopoles have never been observed, and their existence is likely to be purely theoretical, but if they do exist in black holes, they might be revealed by the structure of their accretion discs.

Appendix A

ISCOs in Kerr-Newman Spacetime

The following set of equations needs to be solved for coordinate r and the three constants of motion E, l and K to find the ISCO of a charged test particle in the equatorial plane for $P = 0$.

$$\begin{aligned} \mathbf{R}(r) &= 0\,, \\ \mathbf{R}'(r) &= 0\,, \\ \mathbf{R}''(r) &= 0\,, \\ \Theta(\pi/2) &= 0\,, \\ \Theta'(\pi/2) &= 0\,. \end{aligned} \tag{A.1}$$

The last equation in (A.1) is automatically fulfilled for $\theta = \pi/2$, while the second last equation leads to the relation

$$K = (aE - l)^2\,. \tag{A.2}$$

A polynomial of order four is deduced for $\sqrt{K}$, by implementing relation A.2 into the first two equations in (A.1). It takes the form

$$f_1(u, \sqrt{K}) = A\sqrt{K}^4 + B\sqrt{K}^3 + C\sqrt{K}^2 + D\sqrt{K} + E = 0\,, \tag{A.3}$$

where $u = 1/r$, and

$$\begin{aligned}
A =& \left(4Q^4 + 4Q^2a^2\right)u^6 + \left(-12Q^2 - 4a^2\right)u^5 + \left(4Q^2 + 9\right)u^4 - 6u^3 + u^2\,,\\
B =& 4aeQu^3\left(Q^2u^2 + a^2u^2 - 2u + 1\right)\,,\\
C =& \left(4Q^4 + 4Q^2a^2 - Q^2(eQ)^2 - a^2(eQ)^2\right)u^4 + \left(-10Q^2 - 2a^2 + 2(eQ)^2\right)u^3\\
&+ \left(2Q^2 - 2a^2 - (eQ)^2 + 6\right)u^2 - 2u\,,\\
D =& B\,u^2\,,\\
E =& \left(Q^4 + 2Q^2a^2 - Q^2(eQ)^2 + a^4 - a^2(eQ)^2\right)u^2 + \left(-2Q^2 - 2a^2 + 2(eQ)^2\right)u\\
&- (eQ)^2 + 1\,.
\end{aligned} \tag{A.4}$$

A second equation $f_2(u, \sqrt{K}) = 0$ is deduced from the second and third equation in (A.1). When considering very small black hole charges, for which $Q \to 0$, but $eQ \neq 0$, $f_2(u, \sqrt{K})$ reduces to

$$\begin{aligned}
f_2 =& 6\left(a\sqrt{K}^3 - a^2eQK\right)u^2 + 6\left(a(eQ)^2\sqrt{K} - eQK\right)u + eQ\left(a^2 + K\right) - (eQ)^3 - 2a\sqrt{K}\\
=& 0\,.
\end{aligned} \tag{A.5}$$

Now $f_2(u, \sqrt{K})$ easily can be solved for $u = 1/r$, and the two solutions u_1, u_2 are then implemented into $f_1(u, \sqrt{K})$ for $Q \to 0$ and $eQ \neq 0$. The resulting equations $f_1(u = u_{1,2}, \sqrt{K})$ are solved numerically for $\sqrt{K}$ and lead to four different solutions for every given set of parameters (a, eQ).

Appendix B

Behavior of a Dipole Magnetic Test-Field in Kerr Spacetime

The logarithmic term in the potential of a dipole magnetic test-field in Kerr spacetime can be expressed in its Taylor expansion for $x = 1/r$:

$$\begin{aligned}
\frac{1}{2\xi}\ln\frac{r-1+\xi}{r-1-\xi} =& \frac{1}{2\xi}\left(\ln\left(1-(1-\xi)x\right)-\ln\left(1-(1+\xi)x\right)\right)\\
=& \frac{1}{2\xi}\sum_{n=1}^{\infty}\frac{(1+\xi)^n-(1-\xi)^n}{n}x^n\\
=& \frac{1}{2\xi}\sum_{n=1}^{\infty}\sum_{k=0}^{n}\frac{1}{n}\binom{n}{k}\left(\xi^k-(-1)^k\xi^k\right)x^n\\
=& \sum_{n=1}^{\infty}\left(1+\sum_{k=2}^{\frac{n+1}{2}}\frac{1}{n}\binom{n}{2k-1}\xi^{2(k-1)}\right)\frac{1}{r^n} > \sum_{n=1}^{\infty}\frac{1}{r^n}=\frac{1}{r-1}
\end{aligned} \tag{B.1}$$

One can derive that $A_\phi^{(dipole)} > 0$ for $r > r_+$, $B > 0$ and for all θ by the following consideration:

Since the prefactor $(\Sigma - 4ra^2)$ of the logarithmic term in $A_\phi^{(dipole)}$ (see Eq. (2.28)) is positive for all $r > r_+$, it is sufficient to show that

$$(r-1)\rho^2+2\,r\,(r+a^2)-\left(((r^2+a^2)^2-\Delta a^2\sin^2\theta)-4\,r\,a^2\right)\sum_{n=1}^{\infty}\frac{1}{r^n}<0 \text{ for all } r>r_+,\theta\,. \tag{B.2}$$

It can be rewritten as

$$-(1-a^2)(r+1)-(1-a^2)(1-a^2\cos^2\theta)\sum_{n=1}^{\infty}\frac{1}{r^n}<0\,, \tag{B.3}$$

which is obviously true for $r > r_+$ and $|a| < 1$. Therefore $A_\phi^{(dipole)}$ is positive for $r > r_+$, $|a| < 1$ and $B > 0$.

The qualitative behavior of $A_t^{(dipole)}$ is complimentary along r for $\theta = 0$ and $\theta = \pi/2$. $A_t^{(dipole)}$ reduces at $\theta = \frac{\pi}{2}$ to

$$A_t^{(dipole)}\Big|_{\theta=\frac{\pi}{2}} = -\frac{3}{2}\frac{aB}{\xi^2\rho^2}\left\{r(r-1)\,\frac{1}{2\xi}\ln\frac{r-1+\xi}{r-1-\xi} - r\right\}. \tag{B.4}$$

Since $\frac{1}{2\xi}\ln\frac{r-1+\xi}{r-1-\xi} > \frac{1}{r-1}$, $A_t^{(dipole)}\Big|_{\theta=\frac{\pi}{2}} < 0$ holds if

$$-\frac{3}{2}\frac{aB}{\xi^2\rho^2}\left\{r(r-1)\,\frac{1}{r-1} - r\right\} \leq 0 \tag{B.5}$$

for $0 < a < 1$ and $B > 0$. This is always the case, since the left-hand side reduces to zero. Therefore $A_t^{(dipole)}\Big|_{\theta=\frac{\pi}{2}}$ is negative for $0 < a < 1$ and $B > 0$.

To prove, that $A_t^{(dipole)}\Big|_{\theta=0} > 0$ holds for all $r > r_+$, $0 < a < 1$ and $B > 0$, it is sufficient to show, that its derivative satisfies

$$\partial_r A_t^{(dipole)}\Big|_{\theta=0} < 0 \text{ for } r > r_+,\ 0 < a < 1 \text{ and } B > 0\,.$$

$A_t^{(dipole)}\Big|_{\theta=0}$ diverges at $r \to r_+$ to $+\infty$ and approaches zero for $r \to \infty$. An overall negative derivative therefore restricts the value of $A_t^{(dipole)}\Big|_{\theta=0}$ to positive values. The derivative is given by

$$\partial_r A_t^{(dipole)}\Big|_{\theta=0} = -\frac{3}{2}\frac{aB}{\xi^2\rho^2}\left\{\Big(2(r-1)\rho^2 - \Delta\Big)\,\frac{1}{2\xi}\ln\frac{r-1+\xi}{r-1-\xi} - 2\rho^2 + r - 1\right\} \tag{B.6}$$

As the prefactor of the logarithm is positive for all $r > r_+$, the logarithm can yet again be approximated by $\frac{1}{r-1}$ and $\partial_r A_t^{(dipole)}\Big|_{\theta=0} > 0$ holds for all $r > r_+$, $0 < a < 1$ and $B > 0$, since

$$\begin{aligned} &-\frac{3}{2}\frac{aB}{\xi^2\rho^2}\left\{\Big(2(r-1)\rho^2 - \Delta\Big)\,\frac{1}{r-1} - 2\rho^2 + r - 1\right\} \\ =&-\frac{3}{2}\frac{aB}{\xi^2\rho^2}\,\frac{1-a^2}{r-1} < 0 \end{aligned} \tag{B.7}$$

for the given conditions. Hence, $A_t^{(dipole)}\Big|_{\theta=0}$ is positive for all $r > r_+$.

Bibliography

[1] K. Schroven, E. Hackmann, and C. Lämmerzahl. Relativistic Dust Accretion of Charged Particles in Kerr-Newman Spacetime. *Phys. Rev. D*, 96:063015, 2017.

[2] A. Trova, K. Schroven, E. Hackmann, V. Karas, J. Kovář, and P. Slaný. Equilibrium Configurations of a Charged Fluid around a Kerr Black Hole. *Phys. Rev. D*, 97:104019, 2018.

[3] K. Schroven, A. Trova, E. Hackmann, and C. Lämmerzahl. Charged Fluid Structures around a Rotating Compact Object with a Magnetic Dipole Field. *Phys. Rev. D*, 98:023017, 2018.

[4] B. P. Abbott, R. Abbott, T. D. Abbott, M. R. Abernathy, F. Acernese, K. Ackley, C. Adams, T. Adams, P. Addesso, R. X. Adhikari, and et al. Observation of Gravitational Waves from a Binary Black Hole Merger. *Phys. Rev. Lett.*, 116: 061102, 2016.

[5] B. P. Abbott, R. Abbott, T. D. Abbott, F. Acernese, K. Ackley, C. Adams, T. Adams, P. Addesso, R. X. Adhikari, V. B. Adya, and et al. Multi-messenger Observations of a Binary Neutron Star Merger. *Astrophys.l J. Lett.*, 848(2):L12, 2017.

[6] C. W. Misner, K. S. Thorne, and J. A. Wheeler. *Gravitation.* W. H. Freeman, 1973.

[7] V. M. Kaspi and A. M. Beloborodov. Magnetars. *Annu. Rev. Astron. Astrophys.*, 55(1):261–301, 2017.

[8] R. A. Hulse and J. H. Taylor. Discovery of a Pulsar in a Binary System. *Astrophys. J.*, 195:L51–L53, January 1975.

[9] J. Frank, A. King, and D. J. Raine. *Accretion Power in Astrophysics: Third Edition.* Cambridge University Press, 2002.

[10] J.-H. Woo and C. M. Urry. Active Galactic Nucleus Black Hole Masses and Bolometric Luminosities. *Astrophys. J.*, 579(2):530, 2002.

[11] M. C. Begelman, R. D. Blandford, and M. J. Rees. Theory of Extragalactic Radio Sources. *Rev. Mod. Phys.*, 56:255–351, 1984.

[12] R. D. Blandford and R. L. Znajek. Electromagnetic Extraction of Energy from Kerr Black Holes. *Mon. Not. R. Astron. Soc.*, 179(3):433–456, 1977.

[13] L. Fernández-Jambrina and L. M. González-Romero. *Current Trends in Relativistic Astrophysics*. Springer-Verlag Berlin Heidelberg, 2003.

[14] B. V. Somov. *Plasma Astrophysics, Part I*. Springer Verlag US, New York, 2006.

[15] F. F. Chen. *Introduction to Plasma Physics and Controlled Fusion*, volume 1. Springer Verlag US, New York, 1984.

[16] K. H. Prendergast and G. R. Burbidge. On the Nature of some Galactic X-ray Sources. *Astrophys. J.*, 151:L83–L88, 1968.

[17] H. Bondi. On Spherically Symmetrical Accretion. *Mon. Not. R. Astron. Soc.*, 112: 195, 1952.

[18] F. C. Michel. Accretion of Matter by Condensed Objects. *Astrophys. Space Sci.*, 15:153–160, 1972.

[19] S. L. Shapiro. Accretion onto Black Holes: The Emergent Radiation Spectrum. *Astrophys. J.*, 180:531–546, 1973.

[20] R. K. Ulrich. An Infall Model for the T Tauri Phenomenon. *Astrophys. J.*, 210: 377–391, 1976.

[21] A. F. Illarionov and A. M. Beloborodov. Free-fall Accretion and Emitting Caustics in Wind-fed X-ray Sources. *Mon. Not. R. Astron. Soc.*, 323(1):159–166, 2001.

[22] E. Tejeda, S. Mendoza, and J. C. Miller. Analytic Solutions to the Accretion of a Rotating Finite Cloud towards a Central Object - II. Schwarzschild Space-time. *Mon. Not. R. Astron. Soc.*, 419:1431–1441, 2012.

[23] N. I. Shakura and R. A. Sunyaev. Black Holes in Binary Systems. Observational Appearance. *Astron. Astrophys.*, 24:337–355, 1973.

[24] I. D. Novikov and K. S. Thorne. Astrophysics of black holes. In C. Dewitt and B. S. Dewitt, editors, *Black Holes (Les Astres Occlus)*, pages 343–450, 1973.

[25] F. Yuan and R. Narayan. Hot Accretion Flows Around Black Holes. *Annual Review of Astron. Astrophys.*, 52(1):529–588, 2014.

[26] S. L. Shapiro, A. P. Lightman, and D. M. Eardley. A Two-temperature Accretion Disk Model for Cygnus X-1 - Structure and Spectrum. *Astrophys. J.*, 204:187–199, 1976.

[27] L. G. Fishbone and V. Moncrief. Relativistic Fluid Disks in Orbit around Kerr Black Holes. *Astrophys. J.*, 207:962–976, 1976.

[28] M. A. Abramowicz, M. Jaroszyński, and M. Sikora. Relativistic, Accreting Disks. *Astron. Astrophys.*, 63:221–224, 1978.

[29] M. Kozłowski, M. Jaroszyński, and M. A. Abramowicz. The Analytic Theory of Fluid Disks Orbiting the Kerr Black Hole. *Astron. Astrophys.*, 63:209–220, 1978.

[30] L. Qian, M. A. Abramowicz, P. C. Fragile, J. Horák, M. Machida, and O. Straub. The Polish Doughnuts Revisited - I. The Angular Momentum Distribution and Equipressure Surfaces. *Astron. Astrophys.*, 498(2):471–477, 2009.

[31] V. Witzany and P. Jefremov. New Closed Analytical Solutions for Geometrically Thick Fluid Tori Around Black Holes - Numerical Evolution and The Onset of the Magneto-Rotational Instability. *Astron. Astrophys.*, 614:A75, 2018.

[32] P. Slaný and Z. Stuchlík. Relativistic Thick Discs in the Kerr–de Sitter Backgrounds. *Class. Quantum Grav.*, 22(17):3623, 2005.

[33] H. Kucáková, P. Slaný, and Z.Stuchlík. Toroidal Configurations of Perfect Fluid in the Reissner-Nordström-(anti-)de Sitter Spacetimes. *J. Cosmol. Astropart. Phys.*, 2011(01):033, 2011.

[34] Z. Meliani, F. H. Vincent, P. Grandclément, E. Gourgoulhon, R. Monceau-Baroux, and O. Straub. Circular Geodesics and Thick Tori Around Rotating Boson Stars. *Class. Quantum Grav.*, 32(23):235022, 2015.

[35] P. I. Jefremov and V. Perlick. Circular Motion in NUT Space-time. *Class. Quantum Grav.*, 33(24):245014, 2016.

[36] F. H. Vincent, W. Yan, O. Straub, A. A. Zdziarski, and M. A. Abramowicz. A Magnetized Torus for Modeling Sagittarius A* Millimeter and Images and Spectra. *Astron. Astrophys.*, 574:A48, 2015.

[37] S. S. Komissarov. Magnetized Tori around Kerr Black Holes: Analytic Solutions with a Toroidal Magnetic Field. *Mon. Not. R. Astron. Soc.*, 368(3):993–1000, 2006.

[38] M. Wielgus, P. C. Fragile, Z. Wang, and J. Wilson. Local Stability of Strongly Magnetized Black Hole Tori. *Mon. Not. R. Astron. Soc.*, 447(4):3593–3601, 2015.

[39] P. C. Fragile and A. Sądowski. On the Decay of Strong Magnetization in Global Disc Simulations with Toroidal Fields. *Mon. Not. R. Astron. Soc.*, 467(2):1838–1843, 2017.

[40] H. Kucáková, P. Slaný, and Z. Stuchlík. Toroidal Configurations of Perfect Fluid in the Reissner-Nordström-(anti-)de Sitter Spacetimes. *Journal of Cosmology and Astroparticle Physics*, 2011(01):033, 2011.

[41] J. Kovář, P. Slaný, C. Cremaschini, Z. Stuchlík, V. Karas, and A. Trova. Electrically Charged Matter in Rigid Rotation around Magnetized Black Hole. *Phys. Rev. D*, 90:044029, 2014.

[42] J. Kovář, P. Slaný, C. Cremaschini, Z. Stuchlík, V. Karas, and A. Trova. Charged Perfect Fluid Tori in Strong Central Gravitational and Dipolar Magnetic Fields. *Phys. Rev. D*, 93:124055, 2016.

[43] J. R. Wilson. Some Magnetic Effects in Stellar Collaps and Accretion. *Ann. N. Y. Acad. Sci.*, 262(1):123–132, 1975. ISSN 1749-6632.

[44] T. Damour, R. S. Hanni, R. Ruffini, and J. R. Wilson. Regions of magnetic support of a plasma around a black hole. *Phys. Rev. D*, 17:1518–1523, Mar 1978.

[45] R. M. Wald. Black Hole in a Uniform Magnetic Field. *Phys. Rev. D*, 10:1680–1685, 1974.

[46] Tong Liu, Gustavo E. Romero, Mo-Lin Liu, and Ang Li. Fast Radio Bursts and Their Gamma-Ray or Radio Afterglows as Kerr–Newman Black Hole Binaries. *Astrophys. J.*, 826(1):82, 2016.

[47] A. Nathanail, E. R. Most, and L. Rezzolla. Gravitational Collapse to a Kerr–Newman Black Hole. *Mon. Not. R. Astron. Soc.*, 469(1):L31–L35, 2017.

[48] M. Zajaček, A. Tursunov, A. Eckart, and S. Britzen. On the Charge of the Galactic Centre Black Hole. *Mon. Not. R. Astron. Soc.*, 480(4):4408–4423, 2018.

[49] I. Contopoulos, A. Nathanail, and D. Pugliese. The Orthogonal Gamma-Ray Burst Model. *Astrophys. J. Lett.*, 780(1):L5, 2014.

[50] H. Falcke and L. Rezzolla. Fast Radio Bursts: The Last Sign of Supramassive Neutron Stars. *Astron. Astrophys.*, 562:A137, 2014.

[51] R. M. Wald. *General Relativity*. University of Chicago Press, 2010.

[52] H. Reissner. Über die Eigengravitation des elektrischen Feldes nach der Einsteinschen Theorie. *Ann. Phys. (Berlin)*, 355(9):106–120, 1916.

[53] G. Nordström. On the Energy of the Gravitation field in Einstein's Theory. *Proc. K. Ned. Akad. Wet.*, 20:1238–1245, 1918.

[54] E. T. Newman, E. Couch, K. Chinnapared, A. Exton, A. Prakash, and R. Torrence. Metric of a Rotating, Charged Mass. *J. Math. Phys. (N.Y.)*, 6:918, 1965.

[55] P. Goddard and D. I. Olive. Magnetic Monopoles in Gauge Field Theories. *Rep. Prog. Phys.*, 41(9):1357, 1978.

[56] P. O. Mazur. Proof of Uniqueness of the Kerr-Newman Black Hole Solution. *J. Phys. A: Math. Gen.l*, 15(10):3173, 1982.

[57] D. M. Eardley and W. H. Press. Astrophysical Processes Near Black Holes. *Annu. Rev. Astron. Astrophys.*, 13:381–422, 1975.

[58] T. Damour, R. S. Hanni, R. Ruffini, and J. R. Wilson. Regions of Magnetic Support of a Plasma around a Black Hole. *Phys. Rev. D*, 17:1518–1523, 1978.

[59] J. R. Wilson. Some Magnetic Effects in Stellar Collaple and Accretion. *Ann. N.Y. Acad. Sci.*, 262(1):123–132, 1975.

[60] S. Ray, A. L. Espíndola, M. Malheiro, J. P. S. Lemos, and V. T. Zanchin. Electrically Charged Compact Stars and Formation of Charged Black Holes. *Phys. Rev. D*, 68:084004, 2003.

[61] G. W. Gibbons. Vacuum Polarization and the Spontaneous Loss of Charge by Black Holes. *Commun. Math. Phys.*, 44(3):245–264, 1975.

[62] R. S. Hanni. Limits on the Charge of a Collapsed Object. *Phys. Rev. D*, 25: 2509–2514, 1982.

[63] S. A. Teukolsky. Rotating Black Holes: Separable Wave Equations for Gravitational and Electromagnetic Perturbations. *Phys. Rev. Lett.*, 29:1114–1118, 1972.

[64] S. Chandrasekhar. *The Mathematical Theory of Black Holes*. Oxford University Press, New York, 1 edition, 1983.

[65] J. A. Petterson. Stationary Axisymmetric Electromagnetic Fields around a Rotating Black Hole. *Phys. Rev. D*, 12:2218–2225, 1975.

[66] I. G. Moss. Black Holes with Current Loops Revisited. *Phys. Rev. D*, 83:124046, 2011.

[67] J. Bičák and L. Dvořák. Stationary Electromagnetic Fields around Black Holes. II. General Solutions and the Fields of Some Special Sources Near a Kerr Black Hole. *General Relativity and Gravitation*, 7(12):959–983, 1976.

[68] A. R. Prasanna and C. V. Vishveshwara. Charged Particle Motion in an Electromagnetic Field on Kerr Background Geometry. *Pramana*, 11(4):359–377, 1978.

[69] A. R. Prasanna and S. Sengupta. Charged Particle Trajectories in the Presence of a Toroidal Magnetic Field on a Schwarzschild Background. *Phys. Lett. A*, 193(1): 25 – 30, 1994.

[70] M. Takahashi and H. Koyama. Chaotic Motion of Charged Particles in an Electromagnetic Field Surrounding a Rotating Black Hole. *Astrophys. J.*, 693(1):472, 2009.

[71] G. K. Parks. *Physics of Space Plasmas - An Introduction*. Redwood City, CA, Addison-Wesley Publishing Co, 1991.

[72] M. Henon. Vlasov Equation. *Astron. Astrophys.*, 114:211, 1982.

[73] A. J. Brizard and A. A. Chan. Nonlinear Relativistic Gyrokinetic Vlasov-Maxwell Equations. *Physics of Plasmas*, 6(12):4548–4558, 1999.

[74] L. Rezzolla and O. Zanotti. *Relativistic Hydrodynamics*. Oxford University Press, Oxford, England, 2013.

[75] C. F. Gammie, J. C. McKinney, and G. Tóth. HARM: A Numerical Scheme for General Relativistic Magnetohydrodynamics. *Astrophys. J.*, 589(1):444, 2003.

[76] J. A. Font. Numerical Hydrodynamics and Magnetohydrodynamics in General Relativity. *Living Rev. Relativ.*, 11(1):7, 2008.

[77] A. M. Anile. *Relativistic Fluids and Magneto-fluids: With Applications in Astrophysics and Plasma Physics*. Cambridge University Press, Cambridge and New York, 1989.

[78] Y. Mino. Perturbative Approach to an Orbital Evolution around a Supermassive Black Hole. *Phys. Rev. D*, 67:084027, 2003.

[79] V. I. Arnol'd. *Mathematical Methods of Classical Mechanics*. Springer-Verlag New York, 2 edition, 1989.

[80] E. Hackmann and H. Xu. Charged Particle Motion in Kerr-Newmann Space-times. *Phys. Rev. D*, 87:124030, 2013.

[81] P. Byrd and M. Friedman. *Handbook of Elliptic Integrals for Engineers and Physicists*. Springer Verlag, Berlin, 1954.

[82] E. Tejeda, P. A. Taylor, and J. C. Miller. An Analytic Toy Model for Relativistic Accretion in Kerr Space-time. *Mon. Not. R. Astron. Soc.*, 429:925–938, 2013.

[83] R. Fujita and W. Hikida. Analytical Solutions of Bound Timelike Geodesic Orbits in Kerr Spacetime. *Class. Quantum Grav.*, 26(13):135002, 2009.

[84] M. Köcher and A. Krieg. *Elliptische Funktionen und Modulformen.* Springer-Verlag Berlin Heidelberg, 2 edition, 2007.

[85] L. M. Milne-Thomson. Jacobian Elliptic Functions and Theta Functions. In M. Abramowitz and I. A. Stegun, editors, *Handbook of Mathematical Functions With Formulas, Graphs, and Mathematical Tables*, chapter 16. National Bureau of Standards, 10 edition, 1972.

[86] K. Bobek. *Elliptische Funktionen und Modulformen.* B. G. Teubner Leipzig, 1884.

[87] J. M. Bardeen, W. H. Press, and S. A. Teukolsky. Rotating Black Holes: Locally Nonrotating Frames, Energy Extraction, and Scalar Synchrotron Radiation. *Astrophys. J.*, 178:347–369, 1972.

[88] J. Kovář, P. Slaný, Z. Stuchlík, V. Karas, C. Cremaschini, and J. C. Miller. Role of Electric Charge in Shaping Equilibrium Configurations of Fluid Tori Encircling Black Holes. *Phys. Rev. D*, 84:084002, 2011.

[89] M. A. Abramowicz and P. C. Fragile. Foundations of Black Hole Accretion Disk Theory. *Living Rev. Relat.*, 16:1, 2013.

[90] R. N. Henriksen and D. R. Rayburn. Hot Pulsar Magnetospheres. *Mon. Not. R. Astron. Soc.*, 166(2):409–424, 1974.

[91] H. Fischer and H. Kaul. *Mathematik für Physiker Band 1: Grundkurs.* Vieweg+Teubner Verlag Springer, Wiesbaden, Germany, 2011.

[92] M. A. Abramowicz. The Relativistic von Zeipel's Theorem. *Acta Astronomica*, 21: 81, 1971.

[93] S. Mendoza, E. Tejeda, and E. Nagel. Analytic Solutions to the Accretion of a Rotating Finite Cloud towards a Central Object – I. Newtonian Approach. *Mon. Not. R. Astron. Soc.*, 393(2):579–586, 2009.

[94] J. M. Bardeen and J. A. Petterson. The Lense-Thirring Effect and Accretion Disks around Kerr Black Holes. *Astrophys. J. Lett.*, 195:L65, 1975.

[95] S. Kumar and J. E. Pringle. Twisted Accretion Discs - The Bardeen-Petterson Effect. *Mon. Not. R. Astron. Soc.*, 213:435–442, 1985.

[96] Fragner, M. M. and Nelson, R. P. Evolution of Warped and Twisted Accretion Discs in Close Binary Systems. *Astron. Astrophys.*, 511:A77, 2010.

[97] A. M. Beloborodov and A. F. Illarionov. Small-scale Inviscid Accretion Discs around Black Holes. *Mon. Not. R. Astron. Soc.*, 323:167–176, 2001.

[98] I. Zalamea and A. M. Beloborodov. Mini-discs around Spinning Black Holes. *Mon. Not. R. Astron. Soc.*, 398:2005–2011, 2009.

[99] F. Daigne and J. A. Font. The Runaway Instability of Thick Discs around Black Holes – II. Non-constant Angular Momentum Discs. *Mon. Not. R. Astron. Soc.*, 349(3):841–868, 2004.

[100] F. J. Ernst. New Formulation of the Axially Symmetric Gravitational Field Problem. *Phys. Rev.*, 167:1175–1178, 1968.

[101] G. Pappas and T. A. Apostolatos. An All-purpose Metric for the Exterior of Any Kind of Rotating Neutron Star. *Mon. Not. R. Astron. Soc.*, 429(4):3007–3024, 2013.

[102] Z. Stuchlík and M. Kološ. Acceleration of the Charged Particles due to Chaotic Scattering in the Combined Black Hole Gravitational Field and Asymptotically Uniform Magnetic Field. *Eur. Phys. J. C*, 76(1):32, 2016.

[103] A. Trova, V. Karas, P. Slaný, and J. Kovář. Electrically Charged Matter in Permanent Rotation around Magnetized Black Holes: A Toy Model for Self-gravitating Fluid Tori. *Astrophys. J. Supple. Ser.*, 226(1):12, 2016.

[104] V. Karas, J.-M. Huré, and O. Semerák. Gravitating Discs Around Black Holes. *Class. Quantum Grav.*, 21(7):R1, 2004.

[105] P. J. Montero, J. A. Font, and M. Shibata. Influence of Self-Gravity on the Runaway Instability of Black-Hole–Torus Systems. *Phys. Rev. Lett.*, 104:191101, 2010.

Acronyms and Notations

Acronyms

ADAF advection dominated accretion flow

AGN active galactic nuclei

Cyg X-1 Cygnus X-1

GR general relativistic

ISCO innermost stable circular orbit

LNRF locally nonrotating reference frame

MHD magnetohydrodynamics

MRI magneto-rotational instability

quasar quasi stellar radio source

Sgr A* Sagittarius A*

ZAMO zero angular momentum observer

Symbols

A_α electromagnetic four-potential 12

$A_\alpha^{(dipole)}$ four-potential of a dipole magnetic test-field in Kerr spacetime 19

a parameter corresponding to the black hole spin 15